3802

UNIVERSITY OF HAWAI'I LIBRARY

METEOROLOGICAL ANALYSIS OF THE OCTOBER 29, 2000 HANA STORM

A THESIS SUBMITTED TO THE GRADUATE DIVISION OF THE UNIVERSITY OF HAWAI`I IN PARTIAL FULFILLMENT OF THE REQUIREMENTS FOR THE DEGREE OF

MASTER OF SCIENCE

IN

METEOROLOGY

AUGUST 2003

By

Ryan E. Lyman

Thesis Committee:

Thomas A. Schroeder, Chairperson
Gary M. Barnes
Yi Leng Chen

ACKNOWLEDGMENTS

I am grateful for the guidance received from the University of Hawai`i, Department of Meteorology, particularly those involved in my thesis research. I could not have completed the research without the careful scrutiny provided by Dr. Thomas Schroeder, the thought-provoking discussions with Dr. Gary Barnes, and review provided by Dr. Yi-Leng Dave Chen. In addition, I would like to thank Dr. Steven Businger for the continued guidance and opportunities provided.

A big mahalo to my fellow graduate students for the help received over the course of my student career. Specifically, I would like to thank Rebecca Schneider and Cynthia Palmer for their thorough examination of my papers. I also appreciate the time that Steve Caruso, Ian Morrison, Fred Yongxin Zhang, and Tiziana Cherubini took to help me produce GrADS figures. I would also like to thank Sean Daida and Arnold Hori for their help with various computer-related problems.

The National Weather Service has provided the data and support necessary to carry out this research and for this I am grateful. I would like to especially thank Kevin Kodama, Senior Service Hydrologist, for sparking my interest in flash floods and this event in particular.

I am extremely appreciative of my parents and parents-in-law for their continued strength and guidance during my undergraduate and graduate years. Most especially I am grateful for my father-in-law, Andrew Wilson, for the immediate revisions on my thesis so that it would not appear that English is my third language.

Lastly, I would like to thank my wife, Erin, and son, Kamaholu, for the love, support and encouragement that pushed me to finally finish this research. I could never have made it this far without the two of you. Mahalo nui loa kākou.

ABSTRACT

On the 29th of October, 2000, the Hana region on Maui received ~ 700 mm of rain in 7 hours. Radar analyses revealed that the storm responsible for the rain consisted of 7 cells that formed along the southeast slopes of Haleakala. The storm changed character from a series of ordinary cells that repeatedly moved over the Hana region to a quasi-steady cell that survived for nearly 4 hours. This cell accounted for ~ 80% of the rain recorded during the event and had a top that reached above the tropopause, a weak echo region, hail 25 mm in diameter, and maximum reflectivities above 60 dBZ. In contrast to the earlier ordinary cells, the quasi-steady cell moved to the right of the mean cloud-bearing winds.

An upper-level low with its center located 500 km north of Hawaii provided large scale lifting that eliminated the trade wind inversion, a persistent feature over the state. The interaction of the confluence line triggered by the island of Hawaii and the high terrain of Maui appeared to be responsible for the formation of the storm over the Hana region. The low-level upslope flow provided continued forcing for the series of cells, and the terrain may also be responsible for keeping any downdrafts and outflows from disturbing the continuing cell formation. The advection of colder air in the core of a passing short-wave trough enhanced the instability in the area which initiated the development of the intense quasi-steady cell. The author hypothesizes that the quasi-steady cell developed downdrafts with a flow that differed from the prior cells, resulting in an interaction with the low-level flow that maintained the cell for an extended period.

TABLE OF CONTENTS

Acknowledgements....iii

Abstract....iv

List of Tables....vii

List of Figures....viii

List of Abbreviations....x

Chapter 1 Introduction

Background....1

History....2

Goals....7

Chapter 2 Data and Methodology

Data....9

Radar....9

Rain Gages....11

Rawinsondes and Surface Observations....11

Satellite....12

NCEP Reanalysis....12

Methodology....12

Z-R Relationships....12

Cell Definition....14

Cell Tracking....15

Radar Issues....15

Velocity Azimuth Display....18

Chapter 3 Results

Storm Reflectivity Structure....19

Hana Reflectivity Summary....19

Hana Storm Evolution....20

Intensification Pulse....20

Mature Pulse....21

Dissipation Pulse....23

Cell Structure and Movement....24

Rainfall Assessment....25

Synoptic and Sub-Synoptic Analysis....28

PHMO Base Reflectivity....28

Satellite Imagery....30

NCEP Reanalysis....31

PHMO VAD....33

Hilo and Lihue Soundings....33

Steering Wind....36

Chapter 4 Conclusions

Summary....39

Discussion....40

Topics for Future Work....43

Tables....45

Figures....47

References....90

LIST OF TABLES

Tables Page

1. Cell characteristics.....45

2. Hourly percentage of volumetric rainout.....46

LIST OF FIGURES

Figures		Page
1.	Map of the Hawaiian Islands and significant locations	47
2.	Lowest elevation angle of PHKM and PHMO	48
3.	Three tropical-convective Z-R relationships	49
4.	Height of the radar beam center for PHKM and PHMO	50
5.	Scatter diagram of the maximum reflectivity returns for Hana Storm	51
6.	Reflectivity summary of the Hana Storm	52
7.	Volumetric rainout of the Hana Storm	53
8.	Reflectivity PPI for the developing stage (1309-1404 HST)	54
9.	Reflectivity RHI for the developing stage (1309-1404 HST)	56
10.	Reflectivity PPI for the mature stage (1508-1608 HST)	57
11.	Reflectivity RHI for the mature stage (1508-1608 HST)	59
12.	Reflectivity PPI for the dissipating stage (1643-1741 HST)	60
13.	Reflectivity RHI for the dissipating stage (1643-1741 HST)	62
14.	Tracks and origins of the seven cells embedded in the Hana Storm	63
15.	Vertical reflectivity profiles of the seven cells found in the Hana Storm	64
16.	PHKM and PHMO storm total precipitation	65
17.	The PHKM and PHMO best-fit bin vs. the Hana rain gage hourly rainfall	66
18.	Best-fit bin vs. the Hana rain gage: varying the reflectivity cap	67
19.	Best-fit bin vs. the Hana rain gage: varying the Z-R relationship	68
20.	Corrected Hana Storm total precipitation (mm) for 1200 HST to 1900 HST	69
21.	PHMO base reflectivity and wind observations	70
22.	GOES-10 1 km visible imagery for 1000-1600 HST	73

Figures Page

23. 250 hPa isoheights and wind analysis for 1400 HST.....75

24. 500 hPa isoheights and temperature analysis for 1400 HST.....76

25. Surface winds, pressure, and lifted index analysis for 1400 HST.....77

26. 250 hPa and 500 hPa winds with 300 hPa temperatures.....78

27. Sequence of PHMO VAD from 1306 to 1735 HST.....79

28. Hilo and Lihue sounding for 1400 HST 29, October 2000.....82

29. Hilo and Lihue hodograph for 1400 HST 29, October 2000.....83

30. Track description of C6.....84

31. NCEP reanalysis streamline mean tropospheric flow 85

32. NCEP reanalysis grid point mean tropospheric flow.....86

33. PHMO steering wind for 1334 to 1635 HST.....87

34. World record observed point rainfalls for various periods.....88

35. Mokulehua Bridge and "another rain gauge".....89

LIST OF ABBREVIATIONS

ASOS	Automated Surface Observing Systems
BWER	Bounded Weak Echo Region
CAPE	Convective Available Potential Energy
C_c	Mean Cell Motion
cm	Centimeter
C_s	Storm Motion
°C	Degree Celsius
dBZ	Decibels
ft	Feet
g	Grams
GARP	Global Atmospheric Research Program
GATE	GARP Atlantic Tropical Experiment
GOES-10	Geostationary Operational Environmental Satellites 10
HAP	Hana Airport
HaRP	Hawaiian Rainband Project
hPa	Hectopascals
HST	Hawaii Standard Time
HWFO	Honolulu Weather Forecast Office
IR	Infrared
ITO	Hilo Airport
J	Joules
Kg	Kilogram
KI	K-index
km	Kilometer

LAPS	Local Analysis and Predictions System
LCL	Lifted Condensation Level
LEC	Low Echo Centroid
LFC	Level of Free Convection
LI	Lifted Index
m	Meters
mb	Millibars
mm	Millimeters
MM5	Mesoscale Model Version 5
$m\ s^{-1}$	Meters per Second
MSL	Mean Sea Level
MSM	Mesoscale Spectral Model
NCEP	National Centers for Environmental Predictions
NHRE	National Hail Research Experiment
NWS	National Weather Service
PHKM	Kamuela Radar
PHMO	Moloka`i Radar
PPI	Plan Position Indicator
P_s	Propagation Effect
PW	Precipitable Water
QuikSCAT	Quick Scatterometer
R	Rainfall Rate
RAMS	Regional Atmospheric Modeling Systems
RDA	Radar Data Acquisition
R_i	Bulk Richardson Number

RHI	Range Height Indicator
TAMEX	Taiwan Area Mesoscale Experiment
TOGA-COARE	Tropical Ocean Global Atmosphere Couple Ocean-Atmosphere Experiment
s	Seconds
STP	Storm Total Precipitation
UTC	Universal Time Coordinated
US	United States
VAD	Velocity Azimuth Display
VCP	Volume Coverage Pattern
VCP 11	Precipitation VCP Mode
VCP 21	Severe Weather VCP Mode
VIS	Visible Imagery
VWS	Vertical Wind Shear of the Horizontal Wind
WATADS	WSR-88D Algorithm Testing and Display System
WER	Weak Echo Region
WSR-77	Weather Service Radar 1977
WSR-88D	Weather Service Radar 1988 Doppler
Z	Radar Reflectivity Factor

CHAPTER 1. INTRODUCTION

1.1 BACKGROUND

On the afternoon of October 29, 2000, a storm in the Hana area on the island of Maui produced more than 700 mm of rain in 7 hours. This amount exceeded the 100-year recurrence interval value for the Hana area (U.S. Department of Commerce 1962). The Hana area is located on the eastern slope of Haleakala (Fig. 1), the third largest mountain in the State of Hawai`i (3055 m elevation). The storm (hereafter referred to as the Hana Storm) left residents and tourists stranded when the only public road servicing the region was severed by the flash floods. It also produced hail 25 mm in diameter, was responsible for several home evacuations, required numerous rescues, and included one incident of a car being swept 30-40 meters downstream. Fortunately no lives were lost. If this storm had occurred over a populated, developed area, the loss of life and property damage could have been devastating.

The State of Hawai`i has always been vulnerable to heavy rain events. On average, six flash floods occur each year throughout the State (Kodama and Barnes 1997). Extreme rain rates, small watersheds with rapid response times, and a data sparse environment have made the forecasting of flash floods in Hawai`i a challenge. In reality, determining where and when flooding will occur, in addition to the duration and magnitude of the rain is generally left to nowcasting. The Hana flood was no different. However, a large amount of convective activity close to highly populated areas likely shifted the attention away from the isolated Hana Storm and thus, added to the challenge.

Prior to the installation of the WSR-88D's (Weather Surveillance Radar-1988 Doppler), forecasters relied on satellite imagery, rain gauges, rawinsondes, and cooperative and public observations to anticipate flash flood producing storms. While

Hawai`i boasts one of the densest rain gauge networks in the world (Giambelluca, 1986), the telemetered rain gauges (http://www.prh.noaa.gov/hnl/pages/hydrology.html) used for flood warnings are sparse. Even with the complete rain gauge network, the convective scales of flash flood producing storms still forces speculation as to how much rain actually fell (Schroeder, 1977). It was not until November 1993, when the first WSR-88D was commissioned in Hawai`i, that forecasters were able to use operational radar to provide nowcasts of flash flood producing storms, analyze storm/cell movement, and make informed decisions of the location of the heavy rains. Despite the addition of the WSR-88Ds, there is still little documentation concerning detailed reflectivity structure of flash flood producing storms in Hawai`i. Fortunately, studies have given forecasters the ability to determine environments favorable for heavy rain (Haraguchi 1977; Maddox et al. 1979; Chappel 1986).

1.2 HISTORY

1.2.1 Overview of ingredients of a flash flood producing storm.

Maddox et al. (1979) prepared one of the most comprehensive studies of heavy rain events that occurred over the continental U.S. They studied 151 events and found the following eight features common to these events:

1. Torrential rains were associated with convective storms.
2. Surface dew point temperatures were high.
3. High moisture content was found through a deep tropospheric layer.
4. Weak shear of the horizontal winds existed through the cloud-bearing layer.
5. Convective cells repeatedly form and move over the same area.
6. A weak 500-hPa trough helped to trigger and focus the storms.
7. Storm area was near the mid-tropospheric large-scale ridge position.

8. The storms generally occurred at night.

Six of the eight features are generally the result of the governing environment and can often be anticipated with the synoptic models that are readily available to forecasters, while the eighth feature can be easily timed. However, the fifth feature is often due to one or more mesoscale processes.

1.2.2 Prior studies that have described the formation and movement of storms over the same area.

Several studies that have addressed the concept of cells repeatedly forming and moving over the same area. The common conclusion is that quasi-stationary or slow-moving precipitation systems are frequently responsible for heavy rains and flash floods (Maddox et al. 1979; Chappell 1986; and Doswell et al. 1996). Chappel (1986) explained that storm motion, $\mathbf{C_s}$, is the sum of two vectors: 1) the mean cell motion, $\mathbf{C_c}$, and 2) the so-called propagation effect, $\mathbf{P_s}$. The mean cell vector is generally found to be near the mean wind vector of the cloud layer. The propagation vector is determined by the formation of new cells relative to the mature cells and may occur anywhere along the storm periphery. If the propagation vector is near equal but opposite to the cell motion, a storm will be virtually motionless.

Doswell et al. (1996) noted that anticipating cell movement is relatively simple; however forecasting the propagation effect is more difficult. The propagation effect is dependent on the development of new convective cells. It is the mesoscale and storm-scale processes that determine exactly where cells develop. Mesoscale features such as mesohighs, topography, and fronts normally provide the trigger that releases potential buoyancy. These boundaries are sometimes easy to recognize and nowcast for potential cell development. However, it is the storm-scale process such as outflow that contributes to how convection behaves, and can be the most difficult to forecast.

Tracking the formation of new cells relative to dissipating cells, and thus probably the outflow, can be best observed and assessed through radar.

1.2.3 Case studies that have addressed the formation and movement of storms over the same area.

One of the most referenced studies of a torrential rain event is the Big Thompson storm by Carena et al. (1978). They used a WSR-77 (Weather Service Radar-1977) and a National Hail Research Experiment (NHRE) radar, as well as the standard observations for their analysis, and found that strong, moist low-level inflow lifted by the Rocky Mountains combined with weak winds resulted in a quasi-stationary storm that dropped as much as 250 mm of rain in four hours. Their analysis also revealed that the relatively deep layer dominated by the collision/coalescence process produced a low echo centroid (LEC) radar structure that is generally more common in the tropics. They concluded that this warm cloud process, together with a moist mid-level environment, limited entrainment and evaporation and contributed to the high precipitation efficiency of the storm.

The Taiwan Area Mesoscale Experiment (TAMEX) was one of the first projects to focus on heavy rainfall and flash flooding over Taiwan. Akaeda et al. (1995) analyzed one flash flood producing storm during TAMEX using radar, mesonet, and model simulations. Through radar they found that although the storms' cells were of modest intensity, the cells continuously formed and tracked over the same area, thus spawning flash floods.

With the advent of the WSR-88D's nearly complete coverage of the United States, there have been increasing numbers of studies that have used radars for mesoscale analysis of flash flood producing storms (Bauer-Messmer et al. 1997; Baeck and Smith 1997; Petersen et al. 1999). Most of the studies conclude that flash flood

producing storms have radar structures similar to the Big Thompson storm. The storms are nearly stationary with cell regeneration on the rear flank of the storm relative to cell movement (Chappel 1986). Under this scenario, cells train over the same area until the moisture or bouyancy is exhausted, consistent with Akaeda's finding.

1.2.4 Flash flood storms in Hawai`i.

The analysis of 44 heavy rain events that occurred on the Southeast Flank of Mauna Loa on the Island of Hawai`i by Kodama and Barnes (1997) is one of the most comprehensive studies conducted. They reviewed Haraguchi's (1977) conclusion that the heavy rains generally occurred when Hawai`i was under one of four synoptic environments: tropical cyclone, sub-tropical low, cold front/shearline, or upper level trough/low. They found that all disturbances tend to erode or weaken the trade wind inversion, a persistent feature of the sub-tropical high. Their study revealed that there was a good correlation between the upslope flow component of the low-level winds and the rain. Kodama and Barnes also pointed to a common characteristic of the heavy rain events: a moist mid-level environment, which is very similar to the findings by Carcena et al (1978). They proposed two roles for the mid-level moisture: 1) to reduce the entrainment of dry air into the cloud and 2) suppress the formation of cold downdrafts. The reduction of the downdrafts limits density currents that might propagate the convection away from an area.

Carcena et al. (1979) used Schroeder's (1977) analysis of a devastating flash flood that occurred on Oahu, Hawai`i in April of 1974 to support their conclusions about the Big Thompson storm. Schroeder surmised that the Ko'olau mountain range played a crucial role in the persistence of the rains. He speculated that the range helped to anchor the storm by separating the inflow/updraft from the cooler outflow/downdrafts thereby preventing any propagation of the storm via density currents. However, without

radar data, Schroeder could only infer the mesoscale storm structure and movement through rain maps.

One of the concerns of heavy rain events in Hawai`i has been the lack of radar for both research and forecasting (Schroeder 1977, 1978). Although radars have been available for meteorological weather experiments such as the Project Warm Rain (Rodgers 1967) and the Hawaiian Rainband Project (HaRP) (Carbone et al. 1998), no heavy rain events occurred during the time of these investigations. There have been a few studies of Hawaiian flash flood events that have used radar for a mesoscale analysis. Dracup et al. (1991) used 3-cm wavelength radar to examine the New Year's 1987/1988 flash floods on the Island of Oahu. They were able to determine storm movement; however, the highly attenuated beam limited any mesoscale or convective scale analysis. They did hypothesize that the clouds that produced the heavy rain may have resulted from a mesoscale vortex south of Oahu that drifted northward.

Birchard (1999) was one of the first to use the WSR-88D archive data to study a sub-tropical low heavy rain event in Hawai`i. However, the objective of Birchard's research was to determine the Z-R equation best suited for estimating rainfall in Hawai`i, as the nation's default equation was consistently underestimating the rain. He concluded the tropical convective Z-R equation derived by Rosenfeld et al. (1993) produced the best radar rainfall estimates for this one event. Birchard did not analyze the convective scale movements and structure of the storm.

Studies of flash flood producing storms in Hawai`i could only infer the mesoscale storm structure and movement from rain gauges, satellite imagery, and rawinsondes because each of these instruments has limitations. Rain gauges are point-measuring devices. Unless the rainfall intensity is uniform, the convective scale analysis of a flash flood producing storm remains questionable. Although the visible satellite imagery is

available with a horizontal resolution of 1 km, which is adequate for detecting mesoscale disturbances, cirrus shields can hide the location of the heavy precipitating clouds. In addition, Haraguchi (1977) found that heavy rains in Hawai`i generally occur at night, in which case lower horizontal resolution infrared satellite imagery must be used. While infrared imagery may be useful to determining deep convective cold top clouds and thus potential areas for flash floods, Schroeder (1978), Cram and Tatum (1979), and Dracup et al. (1991) noted that torrential rains have fallen from warm clouds. Rawinsondes are launched twice a day (0000 UTC and 1200 UTC) at two locations, Hilo and Lihue. This limits the analysis of a storm's mesoscale dynamic and thermodynamic wind structure outside of these two rawinsonde locations and launch times. Outside of mesoscale experiments, a thorough tropospheric data set for Hawai`i will rarely be available.

Prior to the installation of the WSR-88Ds, lack of radar coverage in Hawai`i made it a challenge to produce accurate and timely flash flood warnings. Products from the WSR-88Ds have been available for nearly a decade, while radar data have been archived for over five years. However, there is still little documented evidence of storm cell structure, movement, or intensity over Hawai`i. Radar data are now available for analysis and the intent of this study is to thoroughly use it to document the reflectivity structure of a flash flood producing storm. In doing so, it may improve the ability to monitor and detect flash flood conditions in Hawai'i.

1.3 GOALS

The fundamental goal of this study is to determine the evolution and morphology of the Hana Storm. To achieve this goal several issues will be addressed:

1. Documentation of the reflectivity structure;
2. Estimation of the rainfall using radar;
3. Identification of the synoptic environment to infer the storm's characteristics.

Documentation of the reflectivity field allows the convective structure, intensity, movement, and duration of the Hana Storm to be established. This can then be used to identify the characteristics of the cell(s) embedded in the storm. Were they similar to the cells that produced the April 1974 Oahu flood which were anchored to the terrain? Were the storm's cells continuously forming upstream in the rear flank and advancing over the Hana area similar to the quasi-stationary storm envisioned by Chappel (1986)? Investigation of the cells will allow the storm organization (ordinary cell or supercell) and vertical structure to be assessed. Does the Hana storm have a LEC structure similar to the Big Thompson storm or are the highest reflectivities found above the freezing level like the Great Plains hailstorms?

The rainfall pattern and amount are difficult to establish using the limited official State or National Weather Service (NWS) rain gauges along the eastern slopes of Haleakala. The conversion of reflectivity to rain rate integrated in time and space can be used to determine the rainfall amount. Although there are issues concerning radar rainfall estimations, a quantitative examination can be done to determine any bias for the radar. With this an adjusted precipitation field can be constructed.

The reflectivity structure can be placed in the context of the synoptic environment to infer the intensity and movement of the Hana storm. What provided the instability for the convective clouds? What is the magnitude of the convective instability? Did it change over time? Were there other storms in the area? If so, are there any correlations between the other convective activity and the Hana Storm?

CHAPTER 2. DATA AND METHODOLOGY

2.1 DATA

2.1.1 Radar

The primary data source used in this study was Hawai`i's 10-cm wavelength WSR-88D array. There are currently four WSR-88Ds placed throughout the State of Hawai`i that relay data to the National Weather Service (NWS) for operational use and record information for archiving at the National Climatic Data Center (Fig. 1). The recorded or archived data, often referred to as level II data, are comprised of high-resolution base data (reflectivity, radial velocity, and spectrum width). The spectrum width, which primarily measures the turbulence in the atmosphere, was not used for this research. The base velocity was used solely to produce vertical wind profiles. The Hana area radial wind velocities were not produced consistently due to range folding, and thus were not included in this study. The base reflectivity was the principal data source for this analysis. It has a spatial resolution of 1° by 1 km (hereafter referred to as bins), a reflectivity resolution of 0.5 dBZ, and a maximum range of 460 km. Ground clutter is removed from the reflectivity at the radar data acquisition (RDA) component of the WSR-88D. The volume resolution of the base data changes according to the volume coverage pattern (VCP), which is determined by the operational needs of the NWS.

Each VCP is set to continuously scan the atmosphere at preprogrammed 360° azimuthal sweeps at various elevation angles. Presently there are four VCP's that are available for the WSR-88Ds: clear air (short pulse), clear air (long pulse), precipitation, and severe weather (Crum et al. 1993). For the first half of the Hana Storm, the VCP was set to precipitation mode (VCP 21). Over the course of the storm the NWS changed the VCP to its severe weather pattern (VCP 11). VCP 21 consists of nine 360° azimuthal sweep angles that range from 0.5° to 19.5°. This mode takes approximately

six minutes to complete one volume scan. VCP 11 takes five minutes to complete a volume scan, while making fourteen 360° azimuthal sweep angles with the same range as VCP 21.

Of the four WSR-88Ds positioned throughout Hawai`i, the Kamuela (PHKM) and Moloka`i (PHMO) radars were best situated to observe the evolution of the Hana Storm. The PHKM radar is positioned at approximately 1162 meters above sea level with Hana located approximately 75 km north-northwest of the radar. The overall range of the eastern tip of Haleakala is 60-100 km away from PHKM. At its lowest elevation angle (0.5°) the radar beam is at least two km above sea level and it is partially obstructed by Haleakala (Fig. 2a). The mountain does not block the radar beam at subsequently higher elevation angles (greater than 0.5°). However, at the azimuths of 321-324° of the three lowest elevation angles, the NWS employs spot blanking due to the potential for frequency interference with the astronomical observatories on the summit of Haleakala.

The Kamuela radar did not record the entire duration of the Hana Storm. It stopped scanning at approximately 1718 HST on October 29, 2000 for unknown reason(s). However, the rains did not cease until after 2000 HST. Therefore, for the first half of the storm, the Kamuela radar will be the primary radar source. For the second half of the storm, the PHMO radar will be the only radar source.

The PHMO radar is located 100-150 km from the Hana area with Hana being about 130 km south-southeast of the radar. The advantage of this radar is it rests at 415 m above sea level and thus, at the lowest elevation angle, the beam above the Hana region is still 2-2.5 km above sea level. PHMO was also able to view the evolution of the mesoscale storms/cells that led to the Hana Storm, and it recorded throughout the duration of the event. The Molokai radar, like the Kamuela radar, is partially blocked by

Haleakala at the lowest elevation angle (Fig. 2b). Spot blanking is also engaged at the azimuths of 115-118° of the three lowest elevations.

2.1.2 Rain Gauges

There are a few rain gauges located throughout the Hana area; however, three of the rain gauges are located at the Hana Airport (HAP) and are within 10 meters of each other. One of these rain gauges is the NWS 15 minute telemetered unofficial rain gauge that has a resolution of 0.254 mm. Another is part of the National Climatic Data Center (NCDC) hourly precipitation data network. It records to the nearest 2.54 mm. The last is a part of the state's climatic rain gauge network. This rain gauge is recorded daily at 0800 HST and has a resolution of 0.254 mm. All three recorded the same amount of rain for this event, thus these rain gauges were referred to as the HAP rain gauge. A former NWS employee, John Vares, read the final rain gauge used in this study. He used a 254-mm unofficial rain gauge, which he checked irregularly throughout the day. Unfortunately the location of the rain gauge is accurate to within 1 km.

2.1.3 Rawinsondes and Surface Observations

In Hawai`i, rawinsondes are launched regularly at 0200 and 1400 HST at Hilo and Lihue. The data from both stations (temperature, pressure, relative humidity, and wind speed/direction) were available and used. Both of these locations as well as six other sites throughout the state are equipped with Automated Surface Observing Systems (ASOS), a system that remotely records basic weather elements usually at the end of the hour. In addition to the ASOS, there are several locations throughout the State that report wind direction/speed and maximum/minimum temperatures to the NWS. One of these sites is located at the HAP. All radar, rawinsonde, surface observations, and relevant rain gauge locations can be seen in Fig. 1.

2.1.4 Satellite

Satellite imagery from GOES-10 (Geostationary Operational Environmental Satellites 10) was also used to supplement radar observations as well as evaluate the synoptic and mesoscale conditions. The three basic channels, Infrared (IR), visible (VIS), and water vapor (WV), were available. The 4-km resolution IR channel recorded every half hour, while the 1-km resolution VIS imagery recorded every 15 minutes. Unfortunately, the 8-km resolution WV images were only available at random times and thus were not used for this analysis. Cloud drift winds were also determined using both the IR and VIS imagery. These winds were used to asses the low-level winds near the Hana area.

2.1.5 NCEP Reanalysis

A complete mesoscale analysis, and thus explanation, of the Hana Storm is difficult, if not impossible, using just radars and the limited surface and upper air observations. Consequently, the National Centers for Environmental Predictions (NCEP) reanalysis was used to assess the synoptic environment. The NCEP reanalysis is available four times a day (0000, 0600, 1200, 1800 UTC) with grid points every 2.5°. It was used to address the synoptic environment at various levels as well as the synoptic steering wind over the course of the Hana Storm.

2.2 METHODOLOGY

2.2.1 Z-R Relationships

There have been numerous Z-R relationships that have been uncovered since the advent of the meteorological radar, each applicable for a specific environment, cloud phase, or drop size distribution (Battan 1973). This study will not include a comprehensive selection of a Z-R relationship most appropriate for this storm in both

time and space. However, it is imperative to select a Z-R relationship that was used for regimes similar to the Hana Storm to accurately estimate rainfall. Several Z-R relationships are useful when compared to the limited rain gauge data. Therefore, three proven Z-Rs based on studies of tropical convective rainfall were chosen (Fig. 3) to assess the rainfall.

One Z-R used in this study was $Z = 250\ R^{1.2}$. Rosenfeld et al. (1993) developed this Z-R based on a study of maritime tropical rainfall regime of Darwin, Australia. This Z-R is in operational use at the Honolulu weather forecast office (HWFO), and was found by Birchard (1999) to outperform other Z-R relationships for a heavy rain event in Hawai`i. Another Z-R ($Z = 139\ R^{1.43}$) employed was based on research from Tokay and Short (1996). Their results were established on high-resolution disdrometer and radar data from the Tropical Ocean Global Atmosphere Couple Ocean-Atmosphere Experiment (TOGA-COARE) in the western equatorial Pacific Ocean. The last relationship used was $Z = 230\ R^{1.25}$. Hudlow and Patterson (1979) formulated this Z-R from radar data taken during the Global Atmospheric Research Program (GARP) Atlantic Tropical Experiment (GATE).

All Z-Rs will be used to determine storm total precipitation (STP) at the lowest elevation angle for both radars. STP is the integration of the radar-derived rain rate in both space and time from 1200 HST to 2157 HST for PHMO and from 1200 to 1719 HST for PHKM. It was assumed that the reflectivity was steady state between volume scans. The estimated rainfall from bins surrounding Hana's telemetered rain gauge will then be compared to the rain gauge. Contrasting the rain gauge to the radar estimates should be taken cautiously as they are two different types of measuring devices, both with their own sources of error. Regardless, the rain gauge will be taken

as ground truth. From this comparison one Z-R will be selected to illustrate the STP for the Hana Storm.

2.2.2 Cell Definition

In order to assess the convective structure of the Hana Storm, convective cells were identified, tracked, and analyzed using radar. Four arbitrary thresholds of a convective cell for radar analysis have been adopted as follows:

1. A local maximum of reflectivity ≥ 45 dBZ;
2. 45 dBZ area ≥ 5 km^2;
3. Both of the above evident in at least the two lowest elevation scan angles, and;
4. The above three thresholds must be sustained for at least 15 min.

These thresholds are set in order to track and examine the more significant and organized echoes during their most active lifetime. The first criterion is set so that 1) bright bands were not mistaken as cells, and 2) to evaluate the intense rain shafts. The 45 dBZ area of 5 km^2 was chosen so that very small short lived features were ignored. The third threshold was selected for several reasons. The lowest angle was used to ensure that the bright band would not be mistaken for a cell. The second elevation angle was selected because over the Hana area on this day the radar beam height was at approximately the level of a weak 1 °C inversion (2 km). Thus, if the radar was able to view echoes at this height, the cloud would be able to draw on the atmosphere's potential buoyancy. The fourth requirement was chosen so that short-lived anomalies would not be tracked and analyzed.

Another reason for the selection of these thresholds is my belief that echoes that meet these criteria contribute the most to the total precipitation and thus flash flooding.

Davis's (2001) overview of flash flood forecasting stated "...flash floods tend to evolve on the same time and spatial scales as the intense precipitation...." While the dependence of the flash flooding is essentially unique for each location and time, the cell criteria broadly address Davis's concept. The 45 dBZ threshold is equivalent to 50 mm h^{-1}. According to Davis and Doswell et al. (1996) this rain rate is more than heavy enough to produce flash flooding. The 15-minute threshold is an adequate time scale for flash flooding to occur at or above the 45 dBZ thresholds. The 5 km^2 criterion is small enough to evaluate the spatial scale of the precipitation (although it may not resolve rain shaft cores which may be on the orders of hundreds of meters), but still large enough so that disorganized or anomalous echoes are not assessed.

2.2.3 Cell Tracking

Cells were tracked using the following approach. The location, maximum reflectivity, and the area of 45, 50**, 55**, and 60** dBZ contours of echoes that meet the criteria threshold in the first elevation angle were logged. Subsequently higher elevation angles were then analyzed in the same manner allowing for tilting of cell location in the vertical. Above the second elevation angle maximum reflectivities in the area of lower elevation angles' cell locations were noted regardless if the 45 dBZ threshold was exceeded. This was done until echo values were less than 10 dBZ which was later defined to be the threshold for echo top. This threshold is similar to that used in the NHRE (Foote and Wade 1982).

2.2.4 Radar Issues

There are several significant limitations inherent to the use of radar when tracking cells/echoes or estimating rainfall. The first is the height of the radar beam. The height of the beam is a function of many variables including the elevation and

** *When these contours are applicable*

latitude of the radar station, the elevation angle in use, the range of the bin, and the curvature of the earth (Reinhart 1991). Ideally, for accurate rainfall estimates and assessment of the storm structure, the radar should sample the sub-cloud layer. However, some radar do not sample the sub-cloud layer because of range or beam blockage (which forces the use of higher elevation angles). This issue can be magnified when clouds show signs of a LEC structure (Carcena et al. 1979). LEC clouds generally display tight vertical reflectivity gradients with the greatest reflectivity values in the sub-cloud layer. Thus, under circumstances that force the use of higher elevation angles while sampling LEC-type clouds, it would be quite easy to overshoot the largest reflectivities thereby seriously misjudging the structure and/or rainfall of the storm.

PHKM and PHMO both suffered from inadequate sampling of the sub-cloud layer during the Hana Storm. Range is the key concern for the Molokai radar, and the Kamuela radar is at too high an elevation. At the lowest elevation angle both radars sample the Hana Storm at nearly the same height. However, at higher elevation angles the PHMO beam is higher than PHKM as the height of the radar beam is not a linear function. Figure 4 illustrates the height of the beam center as a function of range for the lowest seven elevation angles for both radars.

Another issue concerning radar, particularly with PHMO radar, is inhomogeneous beam filling due to beam spreading. Rosenfeld et al. (1992) demonstrated that the problem is more prominent when the radar is viewing intense convective cells with large reflectivity gradients. During these atmospheric conditions partial beam filling often leads to lower reflectivity values within a bin due to signal averaging. However, the areal extent of the reflectivity increases as the beam spreads. A scatter diagram of the PHKM and PHMO maximum reflectivity returns is illustrated in Figure 5. It shows that the PHKM to PHMO reflectivity ratio is about 1.1. As a result, PHMO maximum

reflectivity is as much as 4 dBZ less than the PHKM maximum reflectivity. This can be a major concern for both rainfall estimates and cell tracking. While this bias will not be applied to the observed reflectivity, it will be used to adjust for the STP.

The presence of hail in a radar scan is another severe problem as it can lead to gross overestimations in rain (Austin 1987; Baeck and Smith 1997). To minimize this issue a reflectivity cap is frequently used. Nationally the WSR-88Ds' reflectivity cap is set between 51 dBZ (dry areas) and 55 dBZ (tropical areas). Examination of central high plains hailstorms during the NHRE by Knight et al. (1979) supports this range. Only 2 of 19 (11%) storms that had reflectivity maxima less than 55 dBZ deposited hail, none with reflectivity maxima below 50 dBZ. Conversely, 28 of 32 (88%) storms above the 55 dBZ threshold produced hail.

Operationally the HWFO uses a reflectivity cap of 51 dBZ (rain rates ~ 177.4 mm h^{-1}) for its radar derived rainfall estimates. This is well below the recommended reflectivity cap value for a tropical regime. Moreover, a cloud physics study conducted on the Island of Hawai`i during the 1970's (Fullerton and Wilson, 1975) found numerous incidents of instantaneous rain rates greater than 250 mm h^{-1} (~ 55 dBZ) from both cold and warm clouds. Conversely, Birchard's (1999) study of one Hawaiian flash flood producing storm showed little difference in total rainfall when varying the reflectivity cap from 50 to as high as 62 dBZ. To test Birchard's conclusion and the WSR-88D range, reflectivity caps of 51, 53, and 55 dBZ were employed.

The bright band can be an obstacle when estimating rainfall by radar. Furthermore, it can sometimes be mistaken for a cell. The bright band becomes a concern when the radar is sampling near or below the freezing level. It can often increase the reflectivity by as much as 7 dBZ in that area (Reinhart 1991). To alleviate this problem for rainfall estimates the lowest elevation angle was used. This would place

the radar beam about 1.5 km below the freezing level. During cell tracking, the cells must be apparent in two or more elevation angles within the same area.

Anomalous propagation is another limiting factor which occurs when large vertical gradients of temperature and/or water vapor in the atmosphere bend the beam up or down. This can cause interception of the beam by the ground (Hunter 1996). Fortunately WSR-88D uses an algorithm filter to help eliminate this issue.

2.2.5 Velocity Azimuth Display

The Velocity Azimuth Display (VAD) from both the Molokai and Kamuela radars were used to evaluate the temporal change in the horizontal winds in the vertical. VADs were produced for both radars at each volume scan using the WSR-88D Algorithm Testing and Display System (WATADS 2000). There are many assumptions and sources of errors associated with the VADs (Browning and Wexler 1968). One is the time variation of the wind field during the period of an azimuth rotation. Steady state is implied. This is valid given the time scale of a volume scan (~ 5-6 min). More serious sources of errors involve the inhomogeneities in the horizontal distribution of precipitation, and the presence of strong vertical shear. Both of these limitations involve the proper acquisition of the data by the RDA, and cannot be corrected or even identified. Nevertheless, the VADs were used primarily as another source of winds. Unfortunately a complete vertical profile from the height of the radar to the tropopause was not produced for any PHKM volume scans due to the lack of echoes within 50 km of the radar. PHMO did have complete profiles from 1324 to 1635 HST.

CHAPTER 3: RESULTS

3.1 STORM REFLECTIVITY STRUCTURE

3.1.1 Hana Reflectivity Summary

A comprehensive summary of the radar reflectivity time series for the Hana Storm is detailed in Figure 6. It demonstrates that the storm steadily intensified between 1200 and 1500 HST when the 45 dBZ area increased ~ 30 km^2 h^{-1} and maximum reflectivities increased from 45 dBZ to 55 dBZ. It then reached a quasi-steady state between 1500 to 1730 HST with maximum reflectivity near 60 dBZ and a 45 dBZ area of ~ 150 km^2. At the height of the Hana Storm (between 1545 to 1615 HST), tops reached 16 km above sea level, maximum reflectivity was 66 dBZ, and 45 dBZ area was ~ 175 km^2. After 1730 HST, maximum reflectivity and storm area appeared to gradually decrease until 1800 HST when there was a rapid decline. Maximum reflectivities > 45 dBZ were recorded for the duration of the storm.

The effects of beam spreading can be seen in the time series of maximum reflectivities (bottom panel, Fig. 6). PHKM reflectivity was approximately 3-4 dBZ greater than PHMO, especially during the quasi-steady state period of the storm. The effects of beam spreading can also be seen in Figure 10 at the transition (1719 HST) from PHKM to PHMO. The reflectivity becomes smoother and the 60 dBZ contour area suspiciously decreases.

Volumetric rainouts for both radars were calculated by integrating the conversion of reflectivity to rainfall (using Rosenfeld's Z-R relationship) in space. This was done to display a time-series of the volumetric rainout (Fig. 7), which illustrates the rainfall intensity over the Hana Storm. Also shown on this figure are the lifetimes of the various cells comprising the event (this issue will be addressed later). Although the magnitude of the volumetric rainout is a function of the Z-R and reflectivity cap used, pulses in the

rainfall intensity can be recognized. For this study a pulse is arbitrarily defined as an increase in volumetric rainout of ~ $1.5 \cdot 10^7$ m^3 s^{-1} in 15 min. Three pulses can be identified and require further discussion. The first, termed the intensification pulse, happened from 1309 HST to 1404 HST. The second was referred to as the mature pulse and occurred between 1508 to 1608 HST. The last pulse, labeled the dissipation pulse transpired between 1643 to 1741 HST.

3.1.2 Hana Storm Evolution

A sequence of PPIs in Figure 8, 10, and 12 illustrates the evolution of the Hana Storm's precipitation structure for the intensification, mature, and dissipation pulses, respectively. The PPIs were composed from the Kamuela radar for times prior to 1719 HST October 29, 2000 and the Molokai radar for times that follow 1719 HST. Superimposed on several time frames is the HAP wind vector recorded at the corresponding time.

Three approximate levels, 2.5, 4.5, and 10 km above sea level, were chosen to illustrate the sequence of PPIs. The lowest level, 2.5 km, was selected because it was the closest that either radar sampled to the surface of the earth. The 4.5 km level was selected because it was the closest that both radars sampled at approximately the same horizontal section of the freezing level (even though the freezing level is closer to 4 km above MSL). The final height was used to analyze the vertical extent of the reflectivity near the tropopause. Each of the three levels is the approximate height of the radar beam over Hana.

3.1.2a Intensification Pulse

During the first half of this period (Fig. 8) the reflectivity was oriented south to north. Individual echoes with moderate intensity (~ 45 dBZ) can be distinguished as they

develop on the south-southeast flank of Haleakala and move toward the north. Smaller, less intense (15-25 dBZ) echoes can be seen heading toward the Hana region from the east-southeast, presumably with the low-level wind. Some moderate returns can be identified above the freezing level making individual cells easier to recognize. However, few or no organized echoes can be seen near the tropopause. A range height indicator (RHI) of a cell along the assumed inflow direction at 1321 HST is illustrated in Figure 9a. It shows that 45 dBZ barely extends to 4 km, while only weak returns are apparent above 5 km. Overall, stationary convection was not observed during the first half of this pulse. Rather, there was a training of moderately intense cells over the Hana area. This pattern was also evident when the echoes first appeared over the Hana area just after 1200 HST (not shown).

Between 1340 and 1345 HST the reflectivity began to turn clockwise to a south-southwest/north-northeast orientation in the lower two elevation scans. Furthermore, the storm's reflectivity and area increased. At the two lowest levels two cells can be distinguished, one of which extends near the tropopause. Figure 9b shows a RHI along the presumed inflow of the Hana Storm at 1345 HST. This indicates that 50 dBZ was well above the freezing level, while tight reflectivity gradients (~ 20 dBZ km^{-1}) existed above 7 km. At 1400 HST, both cells collapsed as strong 55 dBZ returns were found in the lowest level. Individual cells become difficult to distinguish as the 45 dBZ contour expands and becomes steady state. For the next hour, the Hana Storm contained convective cells similar to ones just described.

3.1.2b Mature Pulse

At 1507 HST the HAP reported east-southeast (120°) winds at 4 m s^{-1} (Fig. 10). The reflectivity at the start of this pulse resembles that of the previous pulse with two cells present, but with a slight increase in the strength of the returns. However, by the

next volume scan (1513 HST) only one cell was evident, and it was strengthening rather than dissipating. At 1518 HST, 60 dBZ can be regularly found above the freezing level, and 15 minutes later a weak hook echo becomes apparent along the inflow side. This reflectivity feature endured for about 30 minutes. Tight reflectivity gradients can also be seen on the inflow side of the Hana Storm. At 1540 HST, 45 dBZ was apparent near the tropopause, while a new cell begins to develop on the southwest flank of the storm. The strong returns (> 60 dBZ) above the freezing level do not diminish until after 1600 HST. Meanwhile, the orientation of the echoes in the lower two elevation scans continue to turn clockwise until it is tilted from southwest to northeast. In the upper level scan, the orientation is more west to east.

Figure 11 shows a sequence of RHIs across the hook echo, and reveals a vertical reflectivity structure not commonly found in the tropics. The first frame is similar to the vertical structure of the cells found during the intensification pulse; however, by the next time a weak echo region (WER) becomes apparent. During the most intense period of the storm (1537 HST) radar reflectivity returns exceeding 60 dBZ were visible near 7.5 km with 15 dBZ recorded above 13 km. Vertical reflectivity gradients decreased to nearly 4 dBZ km^{-1}, while areal extent of the storm increased to nearly 200 km^2. Moreover, throughout most of this pulse the strongest reflectivity returns were found above the freezing level. These reflectivity features are more commonly observed in supercells (Chisholm and Renick, 1972). However, over the next 20 minutes, the strong returns and the WER begin to descend, as the tight reflectivity gradients return (~ 10-15 dBZ km^{-1}). At 1602 HST the WER and the hook echo features disappeared, the 55 dBZ horizontal area decreased, and the vertical extent of 55 dBZ contour only reached to 3-4 km. The HAP winds also switched to 6 m s^{-1} from the north-northwest (340°).

The cell that first appeared at the beginning of this pulse was still visible and roughly in the same location. The cell that appeared around 1530 HST had moved towards the north staying west of the original cell and not fading until 1640 HST. Sometime between the mature pulse and the dissipation pulse the hook echo region (not shown) regenerated. However both features did not attain the same magnitude as an hour before.

3.1.2c Dissipation Pulse

At 1643 HST the persistent notch in the reflectivity along the inflow region was still apparent (Fig. 12). Also present was the quasi-steady cell from the mature pulse. The WER was still observable (not shown) with tight vertical reflectivity gradients above the freezing level. Most of the strongest echoes were found at lower heights with some weak returns (25-35 dBZ) near the tropopause. Nonetheless, the echoes were on a slight strengthening trend.

Over the next 10 minutes the horizontal reflectivity takes on a curious horseshoe structure at the middle and lower levels. A RHI taken across the inflow region at 1658 HST shows a bounded weak echo region (BWER) in response to this feature (Fig. 13a) as the strongest reflectivities were observed above the freezing level. At 1709 HST the weak hook echo becomes more distinguishable at the lower level. However, at 1719 HST PHKM radar stopped recording and thus PHMO was used to analyze the storm. This reduced the horizontal reflectivity resolution and the hook echo feature disappeared. The winds recorded at HAP during this transition switched back to the southeast (140°) at 7 m s^{-1}, but the intense echoes were two km to the southeast. Returns exceeding 60 dBZ were observed above the freezing level for another 10 min, and tight reflectivity gradients were apparent on the southeast side of the storm. A RHI taken at 1730 HST (Fig. 13b) shows that the WER was still present and the

15 dBZ echoes were observed at nearly 10 km in height. Nevertheless, the reflectivity strength and area were dissipating, and most of the convection moved offshore. 50 dBZ returns were still recorded at 1821 HST while the echoes remained fairly organized 5-10 km offshore almost an hour later (not shown). During this pulse, the orientation of the echoes continued to turn clockwise. By 1900 HST, it is tilted in a more west to east manner, especially in the upper two elevation scans.

3.1.3 Cell Structure and Movement

Seven cells have been identified and analyzed throughout the duration of the Hana Storm using the criteria outlined in the Methodology section. Table 2 summarizes major characteristics of each cell, while Figure 7 shows the times of the cells existence relative to the intensity of the storm. One cell, labeled C6, clearly lasts longer than the remaining 6 cells. It also persisted throughout the mature and dissipating pulses of the storm by lasting ~ 4 hours. C6's mean maximum reflectivity height was found at ~ 4 km, and the maximum reflectivity recorded was 66 dBZ. The remaining 6 cells lasted for an average of 60 minutes, and only one of these cells occurred during part of the mature pulse. The first five cells occurred before or during the intensification pulse. The mean maximum reflectivity of these cells was ≤ 60 dBZ and found in the lowest elevation angle.

Figure 14 shows the tracks of each cell from their origin, to cell status, to collapse. C4, C5, and C6 cannot be tracked before reaching cell status. Nevertheless, most of the organized echoes reached cell status near the same location, approximately 1200 m above sea level along the east Haleakala ridge just southwest of Hana. C4 and C6, which were the two longest lasting cells, reached cell status on the northward side of the east Haleakala ridge. The remaining five reached cell status on the southern side.

With the exception of two cells, most of the cells moved toward the north-northeast at 2 - 3 m s^{-1}. One of the exceptions, C5, was a short-lived cell that moved toward the northwest at 0.5 m s^{-1}. The other, C6, moved in a different manner compared to the other cells (first toward the northeast before turning to the southeast) and was very slow-moving (0.5 m s^{-1}).

The mean vertical reflectivity profile of each of the cells is presented in Figure 15. All cells, save C6, have a mean profile similar to LEC structure found in tropical squall lines (Houze, 1977) and other mesoscale systems studied during GATE (Szoke and Zipser 1985), with greatest reflectivity found in the lowest 2 km. Below 5 km, C6 is roughly 10 dBZ greater than any other cell. Furthermore, between 6 and 7 km above sea level, C6 is nearly 25 dBZ greater than any other cells. In fact, the C6 profile resembles the Alberta hailstorms analyzed by Chisholm and Renick (1972) with maximum reflectivity near the freezing level.

3.2 RAINFALL ASSESSMENT

The STP's derived from Rosenfeld's Z-R with a reflectivity cap of 51 dBZ (HWFO default cap) for the two radars with the topography of east Haleakala are presented in Figure 16. The STP period for the PHKM radar is 1200-1719 HST, while the PHMO radar is for 1200-2157 HST. Two rain gauge sites (HAP and the approximate location of John Vares' home) are also plotted on the STP figures as points of reference and verification. The Hana rain gauge recorded 249 mm of rain between 1200 and 2200 HST, while John Vares recorded approximately 686 mm at his rain gauge between 0800 HST on October 29th and 0800 HST on the 30th.

The radar derived horizontal rainfall distribution is similar in shape for both radars, as both radars show rainfall maxima on the northern side of the east Haleakala

ridge. However, the magnitude of the PHMO rainfall is slightly less than the PHKM rainfall, which is likely the result of beam spreading. The rainfall distribution for the PHMO radar is slightly skewed to the east relative to the PHKM radar. This can be attributed to PHMO operating throughout the duration of the Hana Storm, and was thereby able to record C6 as it moved toward the southeast.

A comparison between the radar derived rainfall and the rain gauge of John Vares can be made, assuming that most of the rainfall in the rain gauge fell during the period when the radars were recording. Estimating from the rainfall contours, the PHMO rainfall was approximately 425 mm or about 60% of the recorded rainfall. The estimate from the rainfall contours of the PHKM is similar to the observation at about 620 mm, which is within 10% of John Vares' rainfall value.

A similar comparison of the radar-derived rainfall can also be done with the HAP rain gauge. This comparison is ideal as the location of the rain gauge is accurately known, and, more importantly, there is less assumption about timing since the rain gauge was read hourly. Based on the rainfall contours, both the PHMO and PHKM rainfall were roughly 500 mm, twice the rain gauge observation. Because the radar estimations were so different from the rain gauge, a best-fit bin was found to assess the rainfall temporally. This was accomplished by mapping out the bins within roughly 5 km of the HAP and stratifying them into four quadrants. The rainfall at each bin was estimated hourly using the HWFO default Z-R relationship and hail cap. A statistical analysis to select the best bin was not attempted because of the limited amounts of hourly data points (5 for PHKM and 9 for PHMO). Rather, bins that did not match the shape of the curve (but not necessarily the magnitude) of the Hana rain gauge hourly rainfall were omitted. A best-fit bin for was then selected subjectively within the remaining lot.

The best-fit bins for both radars were found in the southeast quadrant 3-5 km away from the HAP. There were 7 bins from PHKM and 6 from PHMO that matched the curve of the Hana rain gauge hourly rainfall. The best-fit bin from each of these batches for PHKM and PHMO radars are shown in Figure 17. These two points were not co-located but are still within 2 km of each other. Although both bins generally overestimated the rainfall at each hour, the Molokai radar best-fit bin estimated rainfall exceeded the PHKM estimation. This may seem rather odd considering that the reflectivity recorded by PHMO was more prone to beam spreading effects. However, as noted earlier, PHMO did record throughout the duration of the Hana Storm, and was thereby able to record C6 as it moved toward the southeast.

Figure 18 illustrates the effects of varying the hail cap (keeping the Z-R relationship fixed) on the radars best-bin rainfall estimations. Contrary to Birchards' (1999) findings, significant changes resulted particularly at the times when most of the rain fell. This is to be expected as varying the cap from 51 to 53 dBZ can result in 146% change in the rainfall rate for Rosenfeld's Z-R; whereas a 51 to 55 dBZ adjustment increases the rainfall rate 215%. Regardless, the best-fit bin rain trend was closest to the rain gauge trend when a 51 dBZ reflectivity cap was used.

Altering the Z-R but keeping the reflectivity cap constant also resulted in considerable differences as shown in Figure 19. Overall, Rosenfeld's and the GATE Z-R relationship grossly overestimated the rainfall, especially during the heaviest rainfall hours. Tokay and Short's Z-R was the closest to the recorded rainfall, with PHKM estimations being very accurate at most hours. PHMO overestimated the rainfall regardless of the Z-R used.

Due to these findings, the STP for the PHMO radar (since it recorded throughout the duration of the storm) was recalculated and shown in Figure 20. It was derived using

Tokay and Short's Z-R relationship and a reflectivity cap of 51 dBZ. To compensate the effects of beam spreading for PHMO, 3.5 dBZ were added to each bin before computing the rainfall. It illustrates the same overall rainfall distribution of the STP in Fig. 27, but with a maximum rainfall exceeding 700 mm. What makes this value more striking is that between 70 to 80% of this rain primarily fell during 1500 to 1830 HST (Table 2), which was likely the result of C6. Nevertheless, the location of the PHMO rainfall maximum is about 2.5 km southeast of the approximate location of John Vares' rain gauge; the estimates are within 5% of each other.

3.3 SYNOPTIC AND SUB-SYNOPTIC ANALYSIS

3.3.1 PHMO Base Reflectivity

To have a clearer understanding of the behavior of the echoes found in the Hana Storm, it is useful to observe the storm from a larger scale. Therefore examination of the PHMO reflectivity from 0830 to 1830 HST 29 October 2000 will be done to observe the evolution of the echoes within a 230 km radius of the Molokai radar. A sequence of the PHMO radar reflectivity plan position indicators (PPI) using the lowest elevation angle (0.5°) at 60-minute intervals is given in Figure 21. Superimposed on several times are the HAP, various ASOS stations, PHMO and PHKM 900-hPa height velocity azimuth display (VAD), and satellite derived wind vectors recorded at the corresponding time.

At 0830 HST most of the Islands were echo free, with returns ≥ 45 dBZ were present 100 km to northeast of Molokai. Over the next hour, two sets of echoes, organized somewhat linearly with a north-northwest to south-southeast alignment, were located northeast of Oahu and northeast of Molokai. Between 0930 and 1130 HST these linear echo patterns moved toward the southwest and intensified. Just after 1200 HST the orientation of the linear shaped feature northeast of Oahu shifted counter-

clockwise perpendicular to the Ko'olau Mountains (not shown), and moved toward the southeast. The linear feature north of Molokai, on the other hand, became quasi-stationary. At 1230 HST, there is a hint that convection is beginning to occur over Hana, as isolated moderate (< 45 dBZ) convection existed. Low-level winds near the Alenuihaha channel (Fig. 1) throughout this time were from the east-southeast at ~ 5 m s^{-1}, while near land and the convection winds were from the northeast to northwest.

Between 1230 and 1400 HST, the echoes near Oahu continued to advance toward the southeast with maximum reflectivity values exceeding 55 dBZ. When the initial convection cleared Oahu at 1430 HST, the linear echo pattern continued to swing counter-clockwise to a north-south orientation in Kaiwi channel (Fig. 1), while more convection moved over east Oahu. The convection north of Molokai become more clustered in shape, but maintained its position. The Hana Storm appeared to be slowly intensifying as reflectivity near 55 dBZ were recorded and the area of the echoes has increased over this time.

Just after 1430 to around 1530 HST, the echoes north of Moloka`i intensified and started to move slowly toward the southeast. While mostly residual stratiform echoes remained near east of Oahu, convection was occurring over and to the west of Lanai and isolated short-lived thunderstorms were appearing over east Molokai. Meanwhile, the intensity of the echoes over Hana remained steady and stationary.

Between 1530 and 1630 HST, the convection to the northeast near Molokai continued to slowly move toward the southeast but was not intensifying. The echoes west of Lanai initially shifted to the west before lining up with the convection in the Kaiwi channel and progressed toward to the southwest. The thunderstorms over Lanai moved southwest before changing direction to the southeast and dissipating. In the meantime,

the Hana Storm appeared to reach its maximum intensity and started to move slowly to the southeast. By 1730 HST the convection north of Moloka`i had all but dissipated, while the Hana Storm was still going strong as echoes ≥ 55 dBZ persisted. It continued to move slowly southeastward and did not dissipate until after 1830 HST.

3.3.2 Satellite Imagery

Geostationary Operational Environmental Satellite 10 (GOES-10) 1 km visible imagery for four times (1000, 1200, 1400, and 1600 HST) is presented in Figure 22. At 1000 HST (Fig. 22a) there are two major features worth distinguishing. One is the organized convective activity 50 km north of Molokai and Oahu. Using the 4-km resolution IR satellite imagery, the highest cloud top was near – 50 °C. Based on the Hilo sounding, these cloud tops extended to ~ 11 km above sea level. Associated with the convection are the two distinct linear cloud features that were observed in the PHMO base reflectivity: 1) 20 km north of Molokai and 2) 10 km north of Oahu. Relatively cloud-free areas to the southwest of these features can also be seen.

The second major feature is the bow cloud associated with the convergence of easterly trade winds and the westerly katabatic/land-breeze flow from the island of Hawaii (Chen and Nash 1994). Although 1000 HST was a little late for land-breeze flow, observations from the Hilo International Airport (ITO) reveal that the winds did not turn to onshore flow until after 1100 HST (not shown). Thus the bow cloud would still be present from the convergence of the two opposing flows, and this feature flowed directly toward the Hana area. Despite the convergence associated with the bow cloud, there were no clouds with tops above the freezing level in the Hana region before 1200 HST.

The visible imagery at 1200 HST shows the thunderstorms north of the central islands (Oahu, Maui, Molokai, and Lanai) have intensified and moved closer to the

islands. Minimum cloud top temperatures were now near – 60 °C or 13 km above sea level. While most of the islands remained thunderstorm free, clouds have begun to develop over Molokai and Oahu. The Hana region still remained partially influenced by bow cloud from the island of Hawaii.

At 1400 HST, the convection that was north of the central islands had moved toward the southeast, and brushed by the Ko`olau Mountains on the island of Oahu. Minimum cloud top temperatures remained near – 50 to – 60 °C as most of the intense thunderstorms remain north of the islands. The Hana area now shows some signs of convection with cloud top temperatures around – 30 °C or about 10 km. However, it should be noted that the clouds/convection over the Hana region were not a part of the initial convection that was north of the central islands. This was evident by the southwest-northeast boundary of thunderstorm activity off the northeast tip of Molokai.

The visible imagery at 1600 HST reveals that the thunderstorms on the east side of Oahu continued to move toward the southeast. Some convection remained five km to the northeast and west of Molokai. Over the Hana area deep convection had developed as cloud top temperatures reached as low as – 55 °C. The effect of the bow cloud is now difficult to ascertain as low-level clouds had developed in the region northeast of Upolu point (northern tip of the Big Island).

3.3.3 NCEP Reanalysis

Examination of the 250-hPa heights and winds (Fig. 23a) reveals an upper-level trough over the Hawaiian Islands with an area of weak upper-level divergence just east of Oahu. With the exception of the divergence over and to the south of the Big Island, this area coincides with the convection observed in the satellite imagery and the PHMO large-scale reflectivity analysis. Although it is not apparent in this analysis, a cyclonic

circulation that cut off from the westerlies was embedded within the trough. The 500-hPa (Fig. 24) and surface analyses (Fig. 25) illustrates that the cyclonic circulation was apparent only in the upper-levels of the atmosphere. Although it is not shown in any of the figures, the extent of the circulation reached down to 700-850 hPa. The 500-hPa heights and temperature fields establish that this was a cold-core low.

The surface synoptic analysis reveals the upper-level low's influence on the surface wind field. An inverted trough axis was centered near Oahu, with weak (5 m s^{-1}) east-southeasterly flow just east of Hawaii, turning to northeasterlies near Kauai. The lifted index (LI) (Galway 1956), a commonly used measurement of thunderstorm potential, was also calculated from the NCEP reanalysis and employed in the surface analysis to assess the stability of the atmosphere. Values less than zero generally correspond to favorable thunderstorm development. The LI field shows a minimum of - 4 to - 6 °C just north of the islands, which coincides with the location of the upper-level low. The State of Hawai`i was situated in an area where the LI was between - 2 to - 4 °C.

The 500-hPa and 250-hPa winds with 300-hPa level temperatures are illustrated in Figure 26. It confirms the - 39 to - 40 °C cold air anomaly associated with the upper-level low just north of the State during the time of the Hana Storm. Inspection of the isotherms reveals that the 300-hPa air over the Hana region cools by ~ 1.5 °C between 0800 to 2000 HST. This is in response to the advection on the western side of the trough. This advection correlates with the intensification of the convective activity near Oahu, Moloka`i, and Hana.

3.3.4 PHMO VAD

A time series of the PHMO VAD from 1207 to 1735 HST (Fig. 27), is used to demonstrate the movement of the upper-level trough. The numerous missing points prior to 1400 HST and after 1630 HST can be attributed to lack of detectable echoes near the radar. This figure shows that before 1500 HST southwesterlies ≥ 10 m s^{-1} persisted above 8 km. This flow then gradually veered to westerlies for the next hour, before becoming northwesterlies after 1600 HST. Cold air advection can also be seen after 1630 HST, which supports the NCEP reanalysis. The mid-level winds appear to remain from the south throughout the period of this figure, while low-level winds are steadily veering from northerlies to northeasterlies and eventually easterlies. At the time of upper-level westerlies, there is a clear increase in the low-level winds. Just after 1700 HST, there are signs of northwesterlies at around 2 km above sea level.

3.3.5 The Hilo and Lihue Soundings

The 1400 HST Hilo sounding (Fig. 28) indicates three distinct moist layers. The first layer, located between a weak (1.5 °C) inversion (between 800 and 765-hPa) and the lifted condensation level (LCL) at 935-hPa, was nearly saturated (average mixing ratio of 15 g kg^{-1}). The second layer was above the inversion near 625-hPa. The last relatively moist layer was situated between 300-hPa and the tropopause (100-hPa). The Lihue sounding (Fig. 19a) reveals a fairly moist low-level air mass (average mixing ratio of 14 g kg^{-1}), which helps to produce a relatively low LCL (930-hPa). However, above 750-hPa the air is quite dry.

Precipitable water (PW), defined as the total atmospheric water vapor contained in a vertical column of unit cross-sectional area extending between the surface and 200-hPa, was 4.3 cm for Hilo and 3.6 cm for Lihue. Kodama and Barnes (1997) found

that precipitable water in the 750-450 hPa exceeded 1.0 cm for all days with rainfall ≥ 100 mm day^{-1}. In this case, the precipitable water for Hilo and Lihue in the 750 to 450 hPa level was 1.1 cm and 0.8 cm, respectively.

The Hilo sounding was thought to be better representative of the low-level air mass as it was positioned upstream of Hana, and thus was used as the primary parcel analysis. A mixed parcel from the lowest 500 meters would have reached a level of free convection (LFC) at 640-hPa and remain positively buoyant to 225-hPa. Based on this sounding, several stability indices were calculated to assess the stability of the atmosphere. The lifted index (LI) was - 2.6 °C, which is favorable for thunderstorm development and consistent with the NCEP surface analysis. The K-index (KI) (George, 1960), which considers the overall static stability of the 850-500 hPa layer, was 33 °C. Kodama and Barnes (1997) found a strong correlation between KI and rainfall for the southeast flank of Mauna Loa; a KI greater than or equal to 30 °C was a good indication of rainfall exceeding 100 mm in 24 hours. The convective available potential energy (CAPE), a measure of the latent instability in the atmosphere, was 950 J kg^{-1}. CAPE values for this sounding were modest relative to tornadic thunderstorms in the Great Plains, which can have CAPE values on the order of 2000 to 3000 J kg^{-1} (Fankhauser and Mohr, 1977). Compared to values from tropical experiments such as GATE (1000 to 1500 J kg^{-1}) and TAMEX (1200 J kg^{-1}), as well as estimates of 800 to 1200 J kg^{-1} in hurricanes (Jorgensen et al. 1985) the CAPE value from this sounding was high for the Hawaiian region. However, because the thermal wind demonstrated that the upper-level cold air advection likely occurred near the time of this sounding, CAPE was also calculated using a combination of the Hilo and Lihue soundings to evaluate a possible change in the latent instability. Using the Hilo parcel path and temperature profile below

500-hPa, as well as the temperature profile above 500-hPa from the Lihue sounding, the modified CAPE was found to be 1150 J kg^{-1}.

Hodographs of the lowest 10 km, derived from the Hilo and Lihue soundings, are presented in Figure 29. The Hilo sounding depicts weak surface flow (5.5 m s^{-1}) from the east-southeast (120°) that starts to veer with height over the lowest 1.5 km. It then slightly backs for the next 1 km before veering again up to 10 kilometers. The Lihue hodograph points to a layer of northeasterlies from the surface up to 2.5 km. Above this height, the winds back to northerlies and eventually become northwesterlies from 6 km to 10 km. Cold air advection is also evident in the 400 to 250 hPa layer, which supports the VAD and the NCEP reanalysis. The vertical shear of the horizontal winds (VWS) in the lowest 3 km (0.5 to 3.5 km above sea level) was calculated from these soundings. While the VWS for the Lihue sounding was close to zero, it was around 2.3×10^{-3} s^{-1} for the Hilo sounding. This is about one order of magnitude less than what is found in mid-latitude supercells (Weisman and Klemp 1986). The straight-line shape of the Hilo hodograph is similar to typical wind hodographs from supercell storms and mulitcells observed during the Alberta Hail Studies (Chisholm and Renick, 1972), and simulated by Weisman (1986).

An indicator of the type of convection (ordinary or supercell) that may occur is the Bulk Richardson number (R_i). R_i is proportional to the ratio of **CAPE** and a measure of the vertical wind shears, **VWS**, or:

$$R_i = \frac{CAPE}{1/2 VWS^2}$$

VWS was calculated by taking the difference between the density weighted mean wind in the lowest six km and a typical low-level wind (~ 950-hPa). Numerical simulations of thunderstorms by Weisman and Klemp (1982) have shown that $10 < R_i < 50$ are

indicative of supercells, while with R_i > 35 conditions are better suited for ordinary convection. It should be noted that the R_i is a ratio and thus relatively low **CAPE** and **VWS** values could account for supercell-like values. Weisman and Klemp (1986) state that the R_i works best with CAPE values from 1500 to 3500 J kg^{-1}. Nonetheless, the Bulk Richardson number for the Hilo sounding was 35, while the modified sounding was 38. These values suggest that either supercell or multicell type convection could have occurred under this environment.

3.3.5 Steering Wind

The mean motion of each cell and the potential cell motion vector are also illustrated in Figure 29. Potential cell motion was calculated based on the winds from the Hilo and Lihue soundings. Cells embedded in a storm often move in the mean wind direction of the cloud-bearing layer (Fankhauser 1964; Chappell 1986; Doswell et al. 1996). This concept was used to calculate the steering wind of the Hana Storm by density weighting the wind at 50-hPa intervals between 950 to 250 hPa and again from 950 to 500 hPa. This was done for two layers because C6 generally existed in the former layer, while the other six cells primarily were found in the shallower layer. The magnitude and direction of the steering wind for both layers and soundings are displayed in the inset table on Figure 29. The mean cell motion of each cell except C6 was generally to the left of the shallow layer steering wind. C6 appeared to move in the direction of the deep mean layer wind found in the Kauai Sounding. However, based on Figure 14 it is apparent that the movement of C6 is not well described by a single vector. Thus, its movement is separated into two segments: 1) between 1450 to 1542 HST (before the turn), and 2) 1542 to 1835 HST (after the turn). The movement and information regarding this is displayed in Figure 30. This shows that before the turn, C6

moved toward the northeast at 4 m s^{-1}, or just left of the mean deep tropospheric wind reported in the Hilo sounding. After the turn C6 nearly matched the mean tropospheric wind recorded at Lihue of south-southeasterlies at 3.5 m s^{-1}. The NCEP reanalysis was then used to verify a change in the 10 km steering wind over time and space.

The NCEP reanalysis steering wind was calculated for all the grid points within the domain of 135°-180° W and 10°-40° N in a similar manner to that of the Hilo sounding. The only difference in the calculation was the number of levels used. Because the NCEP reanalysis has 17 pressure levels, several key levels (925, 850, 700, 600, 500, 400, 300, and 250 hPa) were selected to estimate the mean tropospheric steering wind. The advantage to using the reanalysis to calculate the steering wind is that wind fields are determined every 6 hours rather than every 12 hours for the rawinsondes. This allowed the examination of the change in the steering wind over time. Therefore, the steering wind was also computed for 0800, 1400, and 2000 HST for each grid point and is illustrated in Figure 31. The upper-level low clearly displays its influence on the steering wind, as it appears that the cyclonic circulation propagates southward in time. Within the center of the low, movement of clouds or thunderstorm cells would be very limited and erratic. The steering wind near Hana in all periods appears to be toward the east-northeast. However, as the low propagates toward the south, the Hana area was within the weak mean flow.

Figure 32 shows the steering level at the four nearest grid points to the Hana area. It shows that the steering wind at the grid point nearest to Hilo and Lihue (site of the rawinsonde launch) are consistent with the soundings. The steering wind at all four grid points changes very little in time. However, the grid point to the northwest of Hana and near the center of the low is of interest. At the time of the Hana Storm the direction and speed of the steering wind at this grid point were very similar to the mean motion of

C6. Whether this movement inferred from the NCEP reanalysis reached the Hana region is difficult to evaluate due to the coarse temporal and spatial resolution. Regardless, the mean flow at any of the surrounding grid points during the time of the Hana Storm is no more the 6 m s^{-1}.

To further investigate the change in the steering wind over time, the mean horizontal wind was derived from the PHMO VAD and displayed in Figure 33. However, because a vertical profile of density is not available at this location, an extrapolation of density was done using the Hilo and Lihue soundings. With this, the steering wind was calculated in the same manner as the NCEP reanalysis and soundings. It is evident that the mean flow remains predominately from the west-southwest at the PHMO site. However, the mean wind speed decreases from 3.5 m s^{-1} to 2 m s^{-1}.

CHAPTER 4: CONCLUSIONS

4.1 SUMMARY

Two 10-cm radars, the NCEP reanalysis, and other conventional meteorological data were used to describe the evolution and morphology of the October 29, 2000 Hana Storm. The conversion of reflectivity to rain rate integrated in time and space demonstrated that the Hana area received ~ 700 mm of rain over 7 hours. This value was based on Tokay and Short's Z-R relationship with a conservative reflectivity hail cap of 51 dBZ, while adding 3.5 dBZ to the reflectivity values at each the Molokai radar bins to correct for inhomogeneous beam filling.

Radar analysis revealed that the Hana Storm consisted of 7 cells that formed at ~ 1200 m above sea level along the southeast slopes of Haleakala. The storm appeared to change character from a series of ordinary cells that trained over the Hana region to a quasi-steady cell that survived for nearly 4 hours. This cell (also known as C6) accounted for roughly 80% of the estimated rain and had supercell-like features such as a hook echo, maximum reflectivities of 60 dBZ recorded near the freezing level, tops that extended above the tropopause, a weak echo region, and hail 25 mm in diameter. In contrast to the ordinary cells that moved with the mean wind in the cloud-bearing layer, C6 moved to the right of the mean wind.

An upper-level low with its center situated 500 km north of Hawai`i provided large-scale lifting which eliminated the tradewind inversion, a persistent feature over the state. It also changed the low-level winds to light east-southeasterlies by forming an inverted trough over the State. These winds aligned the bow cloud, generated by the convergence between the synoptic low-level flow and the offshore flow from the Big Island, so it flowed directly toward Hana. The interaction between the convergence

associated with the bow cloud and the high terrain of Haleakala appears to be the triggering mechanism for the storm.

Inspection of the synoptic analyses shows the upper-level trough moving past the Molokai radar (likely from northwest to southeast) between 1600 and 1630 HST. The advection of upper-level cold air toward the southeast is also apparent before and during the trough's passage. The upper troposphere over the Islands cooled by ~ 1 to 2 °C, which increased CAPE from 950 to 1150 J kg^{-1}. This 20% increase in CAPE and passage of the trough coincides with the order of echo intensification over the Central Hawaiian Islands. First the echoes near Oahu intensified, followed by the echoes north of Moloka'i, and finally the Hana Storm. All of these storms dissipated in the same progression as they intensified. This demonstrates that the large-scale subsidence on the west-side of the trough was responsible for the decay of the convective activity.

4.2 DISCUSSION

While this study gives a detailed analysis of the Hana Storm, I feel there are three issues that require further clarification.

1. Is the 700 mm rainfall estimate reasonable?
2. Was C6 a supercell?
3. What accounted for the change in movement and character of C6?

Based on Figure. 34 taken from Ramage (1995), 700 mm of rain in 7 hours is ~ 25% less than the projected world record rainfall for that duration. The only official rain gauge in the Hana region during the time of this storm recorded ~ 250 mm. However, I believe that the maximum rainfall core was at least 700 mm. This is supported by the adjusted maximum STP from PHMO and John Vares' rain gauge, which are within 5% of

each other. The PHMO rainfall core is 2.5 km upstream of John Vares' rain gauge. This is a reasonable location considering that the radar estimates were derived from the lowest elevation angle which is ~ 2.5 km above sea level. Based on a raindrop fall velocity of 7 m s^{-1} and low-level winds from the southeast at 6 m s^{-1}, the maximum rainfall core would be advected ~ 2 km downstream and within 0.5 km of John Vares' rain gauge. Both rainfall estimates are debatable, but damage and stream height observations confirm this magnitude. For instance, the Mokulehua Bridge, which is adjacent to John Vares' rain gauge, is approximately 30 m wide and 6 m high (personal communication with Kevin Kodama Senior Service Hydrologist for the Honolulu National Weather Service). The Mokulehua River overflowed its banks by nearly 2 m (Fig. 37a). There is also evidence from "another rain gauge," whose location is unknown, that suggests 550 mm fell (Fig. 37b and 37c). While the water in this "rain gauge" was an accumulation of rain from the 28th and 29th of October, I speculate that most of the rain was from the Hana Storm. What makes the 700 mm storm total amount more impressive is that ~ 80% or 560 mm of rain fell over the course of ~ 4 hours and was the product of one cell, C6.

What type of cell was C6, supercell or ordinary? I believe that C6 was supercell, and I will restate the supporting observations:

- The cell persisted for nearly 4 hours;
- It had a weak echo region with a forward reflectivity overhang;
- A hook echo was apparent;
- Hail ≥ 25 mm in diameter fell;
- Reflectivity tops (defined as 10 dBZ) above the tropopause were recorded;
- The Bulk Richardson number was 35 (indicative of supercells)

Do these observations meet the definition of a supercell? Although there are many definitions of a supercell (Doswell 2002), most come to a similar conclusion as Doswell (1986): "...(a supercell) is a convective storm that possesses a deep, persistent mesocyclone." The only suggestion of a mesocyclone in C6 is a questionable hook echo. Unfortunately, the Doppler winds were not available to verify a mesoscale circulation in the Hana Storm. Furthermore, no meso-warnings were recorded by the radar algorithms.

What accounted for the change in character and movement of C6? Unlike the ordinary cells which had a mean height of ~ 6 km, C6 had a mean height of ~ 10 km. The development of C6 coincides with the advection of cold air in the core of the trough. Based on the Hilo sounding, the mean movement of a cell that extended to 10 km would be toward the northeast at 5.7 m s^{-1}. For the first 50 min, C6 did move to the northeast at 4 m s^{-1} (Fig. 14). Later it moved toward the south-southeast at 3.5 m s^{-1}. Based on the mean cloud-bearing flow estimated from the Lihue sounding, this movement is justifiable; but I believe this mean flow was not valid for the Hana region and was coincidental. This was evident in the NCEP reanalysis and the PHMO VAD which demonstrated little change in the northeastward mean steering wind. The PHMO VAD does not show northerly winds at any level until 1630 HST. C6 started moving toward the southeast at 1550 HST. I infer that the interaction between the storm's mesoscale outflow boundaries and the moist low-level inflow air was responsible for the change in motion.

During the first three hours of the storm, cells formed along the east Haleakala ridge and tracked north. Any outflow from these cells would have a northward component as the mountain would block it from going south. This would limit the interaction between the outflow and the southeasterly low-level inflow air. When C6

moved northeast of Haleakala at 1545 HST, the cell's outflow could spread southeastward. This was observed at the HAP at 1608 HST with 6 m s^{-1} north-northwesterly winds. This outflow boundary would oppose the synoptic flow giving the storm its own lifting mechanism. Now the duration of C6 would be dictated by the available moisture and potential buoyancy. This type of storm movement toward the moisture source and to the right of the mean wind has been documented by Browning (1964) and Marwitz (1972) and simulated by Weisman and Klemp (1982). Why didn't C7, which originated 40 min after C6, have a vertical extent comparable to C6 and move toward the northeast as well?

C7 had a mean top of ~ 6 km because C6 likely cut off its moisture source once it moved south-southeastward and in front of the mountain. Without low-level moisture, this cell could not last long or extend very high, despite the available buoyancy aloft. This is also the reason why no cells developed after C7. The movement of C7 would then be to the north as determined by its cloud-bearing depth.

4.3 TOPICS FOR FUTURE WORK

Due to the lack of wind observations, this analysis of the Hana Storm, like previous studies of Hawaiian flash floods, was only able to hypothesize the anchoring mechanism. An alternative analysis was attempted through a simulation of the Hana Storm using the Mesoscale Spectral Model (MSM) (Juang, 2000) with the NCEP reanalysis as initial conditions. This was unsuccessful, as the rainfall pattern was poorly replicated. In the future, a precise simulation of the Hana Storm will be required to further study the effects of the topography, mesoscale outflow boundaries, and any confluence lines triggered by the surrounding Islands on the initiation of flash flood producing storms in Hawai`i. The model would likely need to be initialized close to the

onset of the storm, with high resolution wind observations, and/or using the reflectivity structure from this analysis.

Finally a complete radar analysis of the other cells and storms surrounding the PHMO radar would also be useful. This could be compared to my analysis, which would help to verify my hypothesis that the movement of C6 was governed by the interaction between the storm's mesoscale outflow boundaries with the moist low-level inflow air. The PHMO base velocity could be used on the storms near Moloka`i, which appear to have similar characteristics to the Hana Storm. This will help determine the existence and magnitude of the outflows, and reveal if any mesocyclones were present in these storms. This study would bring closure to the movement and structure of cells within the Hana Storm.

Cell Number	Mean Speed ($m\ s^{-1}$)	Mean Direction (°)	Start Time (HST)	End Time (HST)	Duration (min)	Max Z (dBZ)	Mean Height of Max Z (km)	Mean Height (km)
C1	2.6	175	1210	1320	71	52.5	2.2	6.5
C2	3.0	193	1303	1338	35	54.0	2.2	5.8
C3	2.7	196	1338	1427	48	56.5	2.3	5.9
C4	0.6	194	1321	1512	111	60.0	2.5	7.4
C5	0.6	123	1403	1438	35	54.5	2.5	6.5
C6	0.7	309	1450	1836	225	66.0	4.0	10.0
C7	1.9	199	1532	1643	71	59.0	2.7	6.2

Table 1. Cell characteristics.

HOUR	13	14	15	16	17	18	19
PHMO	1	6	8	28	22	25	11
PHKM	2	10	19	37	32	N/A	N/A

Table 2. Hourly percentage of volumetric rainout. Derived from the PHMO and PHKM radars using Tokay and Short's (1996) tropical convective Z-R ($Z = 139\ R^{1.43}$) relationship with a reflectivity cap of 51 dBZ.

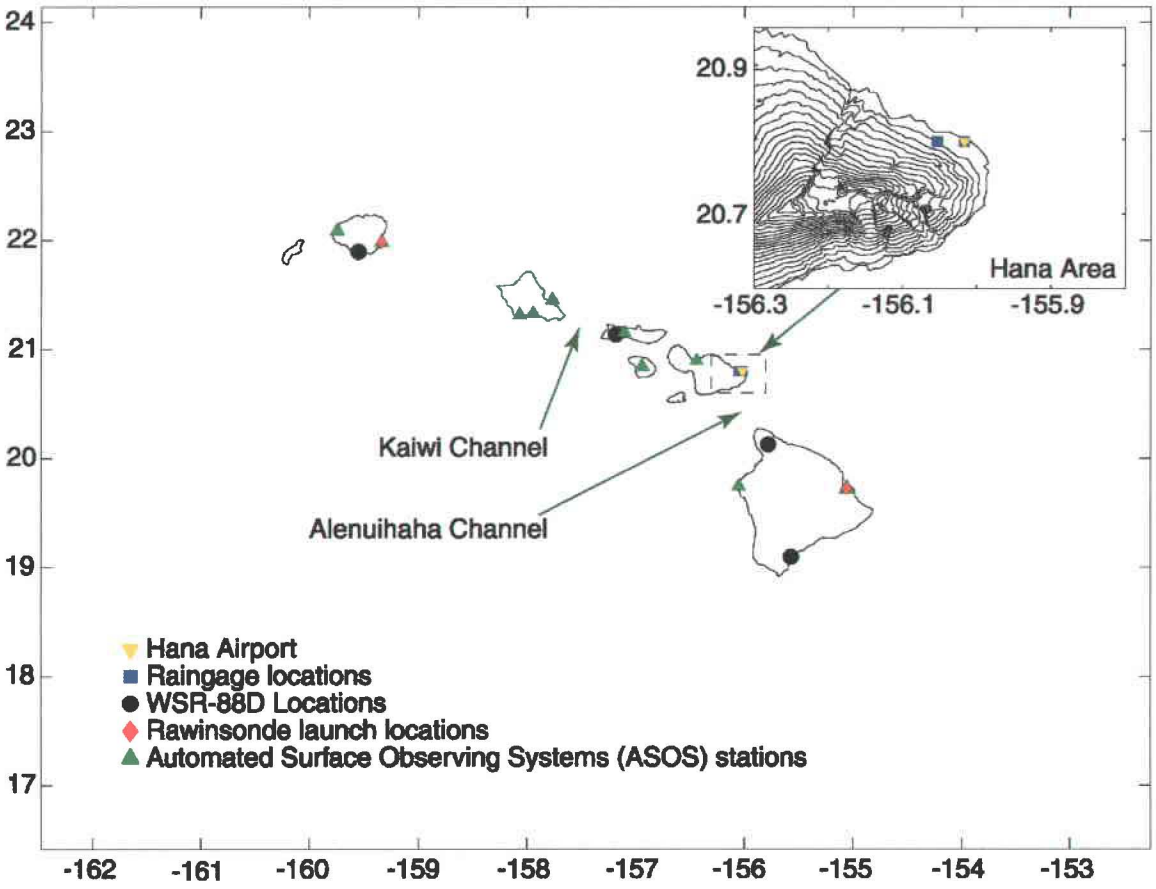

Figure 1. Map of the Hawaiian Islands and significant locations. The blue box denotes the RSM domain, while the yellow box is the area of the MSM domain. The inset in the upper right hand corner shows the Hana area, complete with elevations every 500 ft.

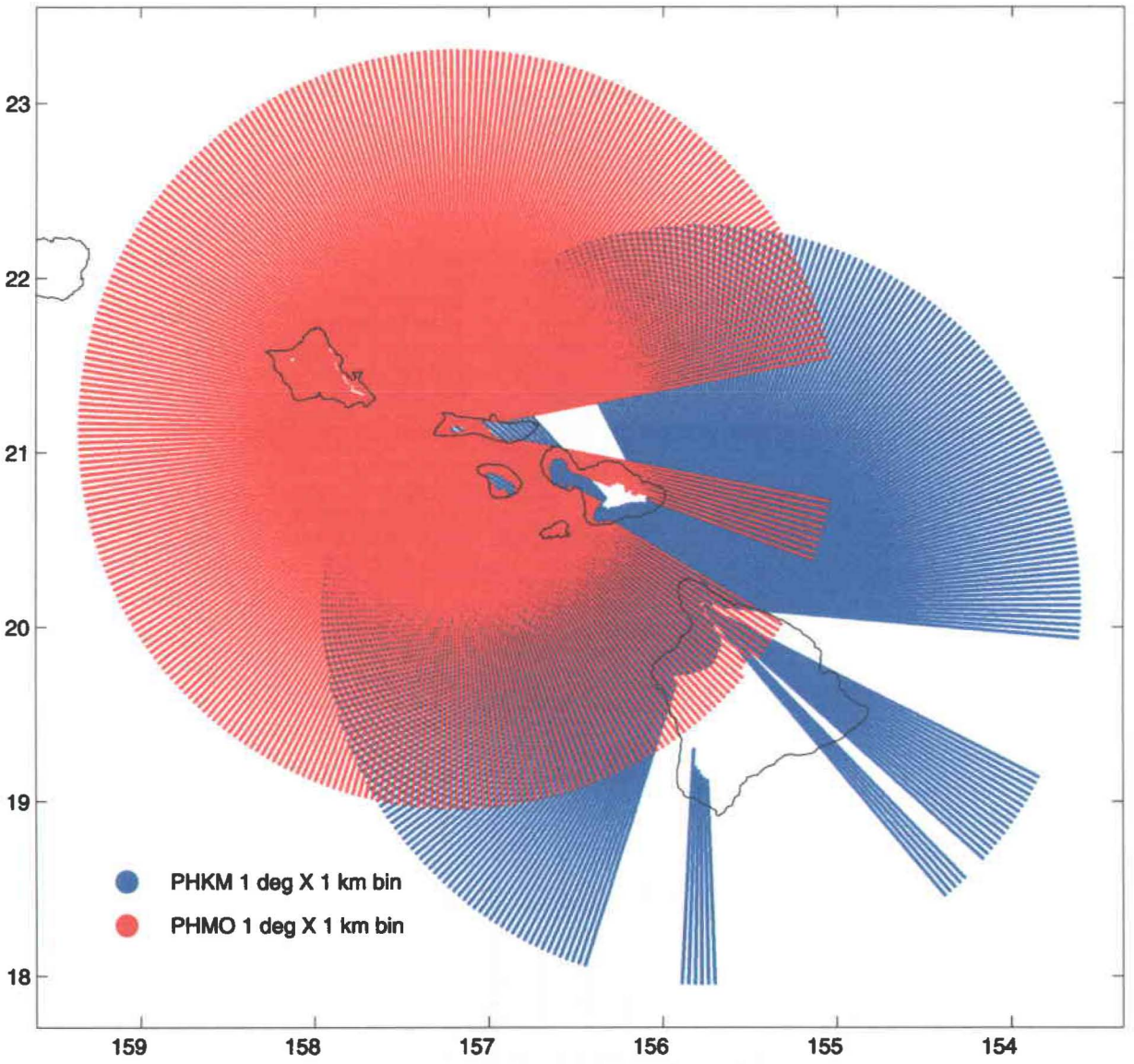

Figure 2. PHKM and PHMO first elevation angle (0.5 °) reflectivity bin location.

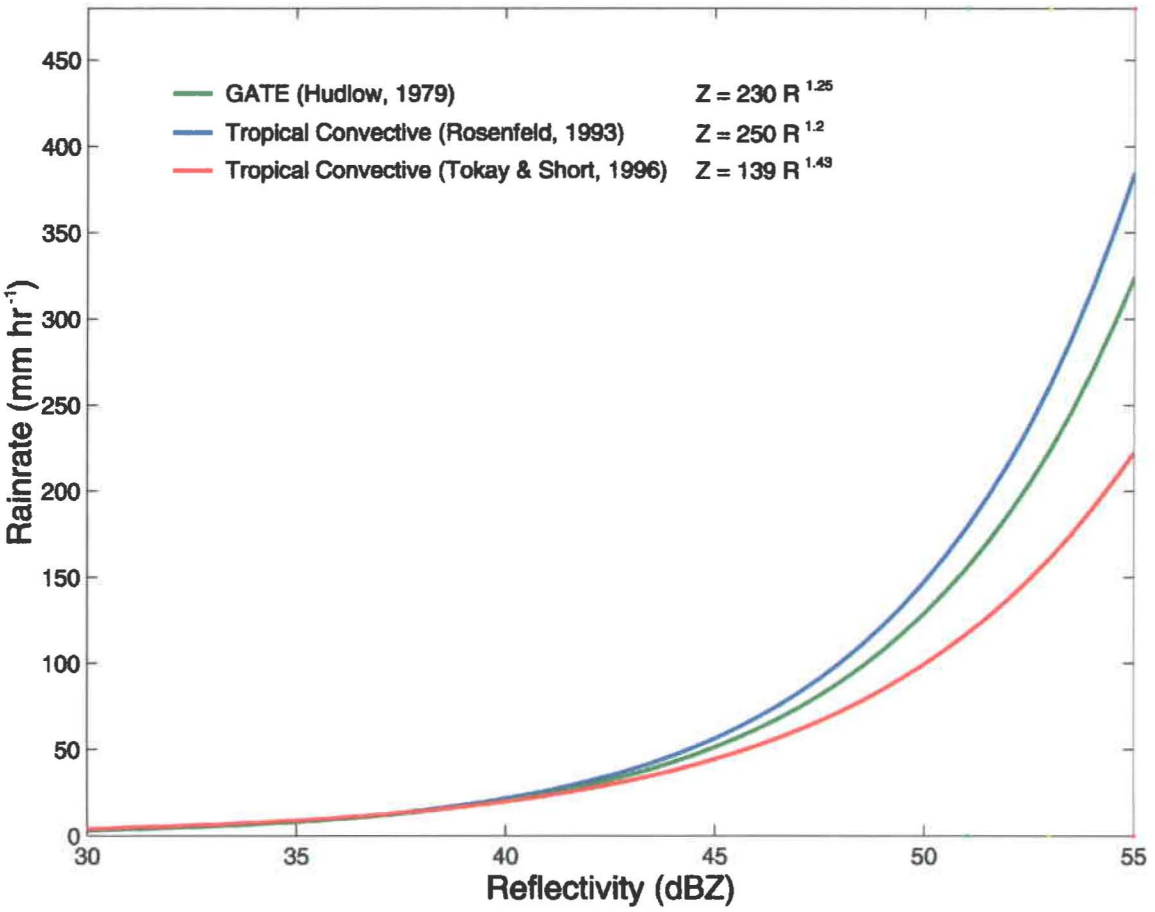

Figure 3. Three tropical convective Z-R relationships used.

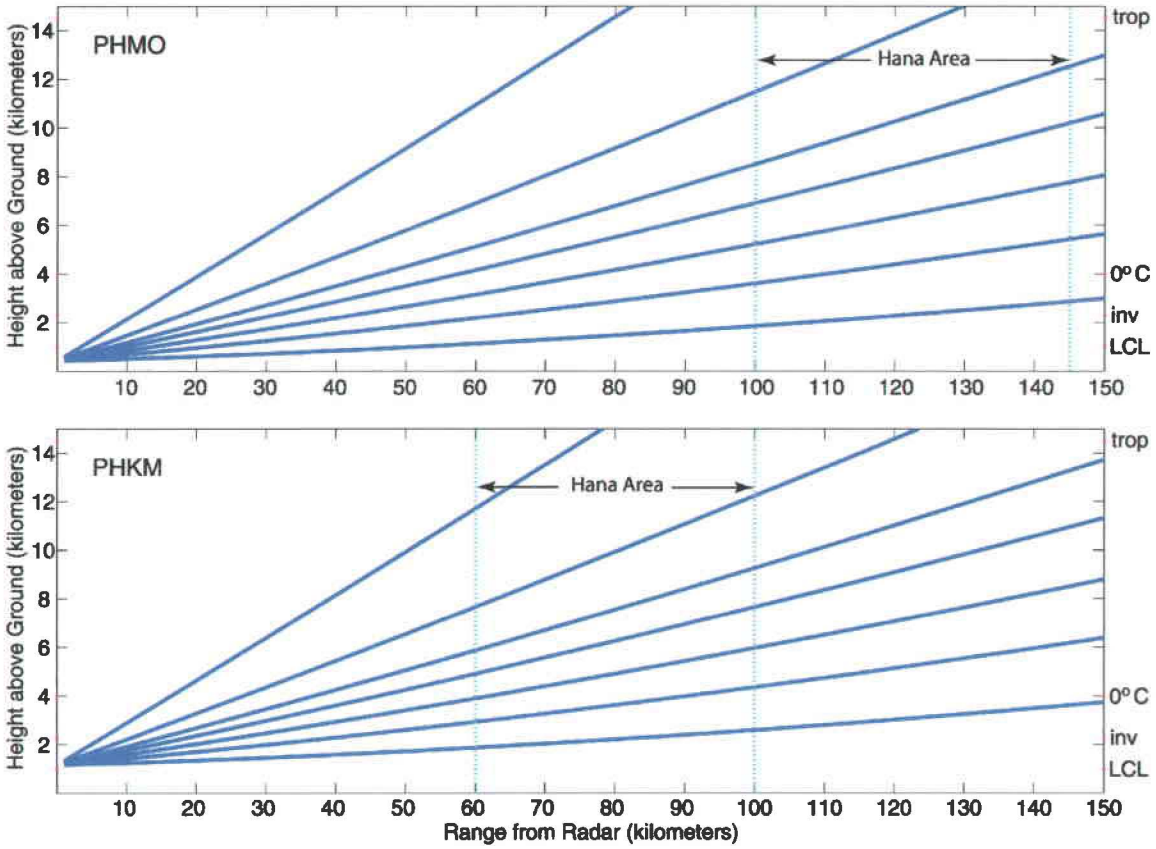

Figure 4. Center of the lowest seven elevation angles for the PHMO and PHKM radars. The range of the Hana area with respect to each radar is denoted within the blue dotted lines. Additionally, four significant heights are labeled on the right axis, lifted condensation level (LCL), inversion (inv), freezing level (0 °C), and tropopause (trop).

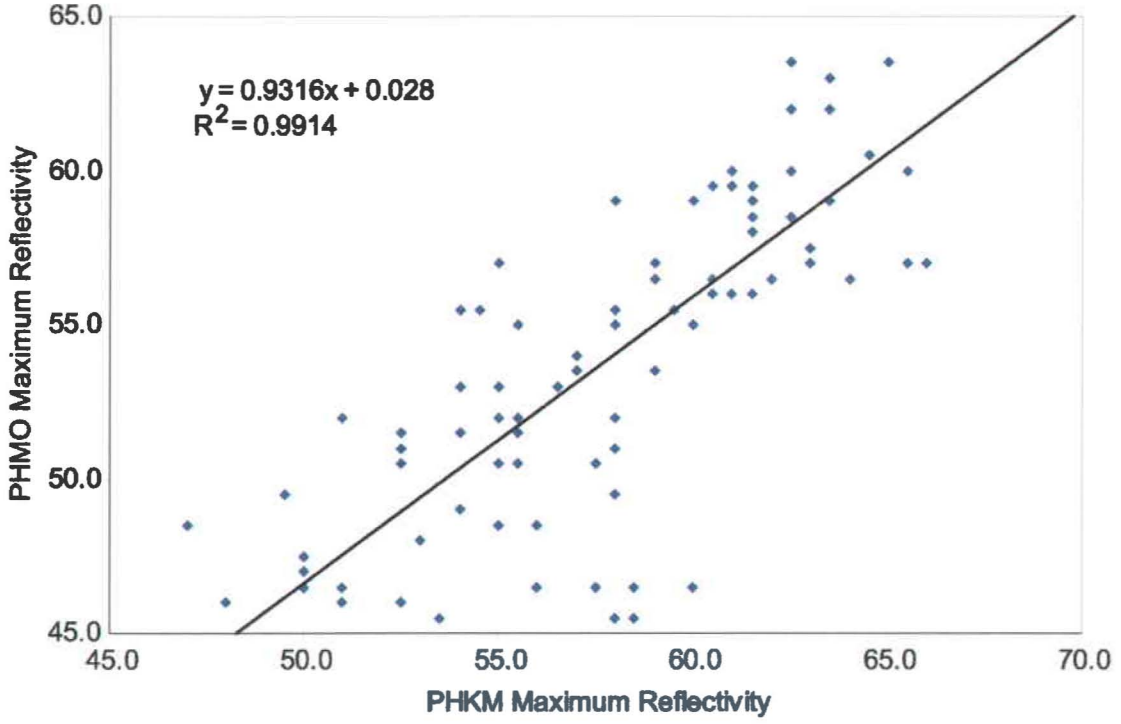

Figure 5. Scatter diagram of the maximum reflectivity returns for the Hana Storm.

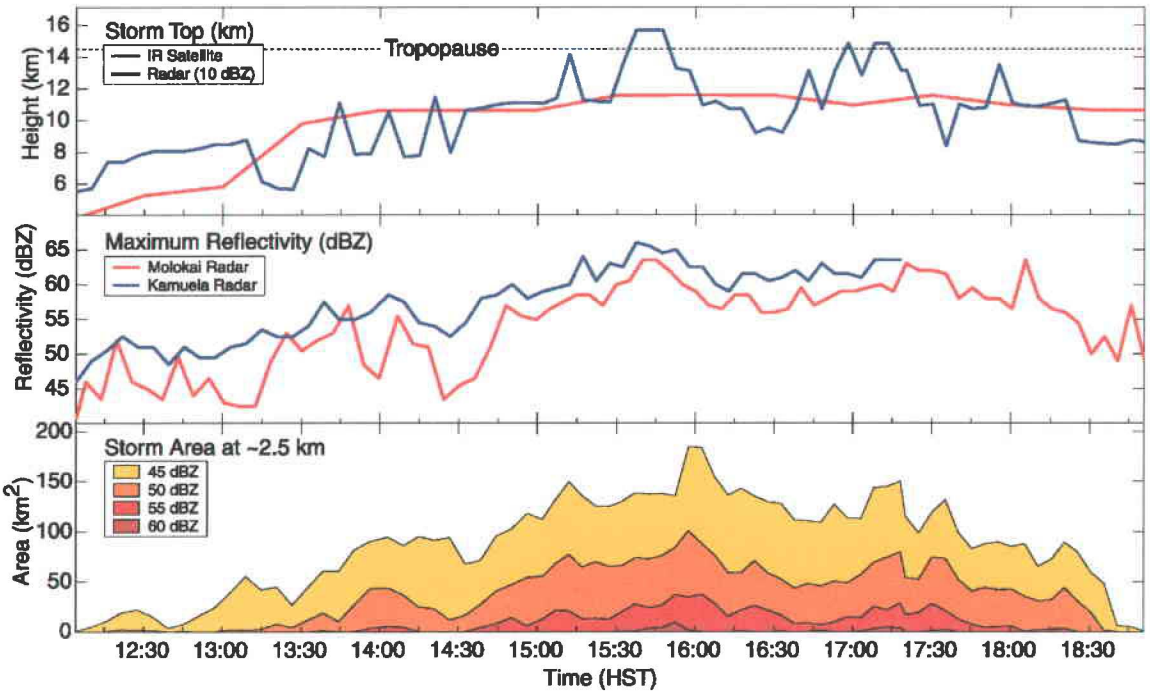

Figure 6. Reflectivity Summary of the Hana Storm. The top panel shows the approximate height of the storm top from the radar (defined as 10 dBZ) and infrared satellite imagery. The middle panel illustrates the maximum reflectivity for both radars, while the bottom panel displays the area enclosed by various reflectivity contours 2.5 km above sea level.

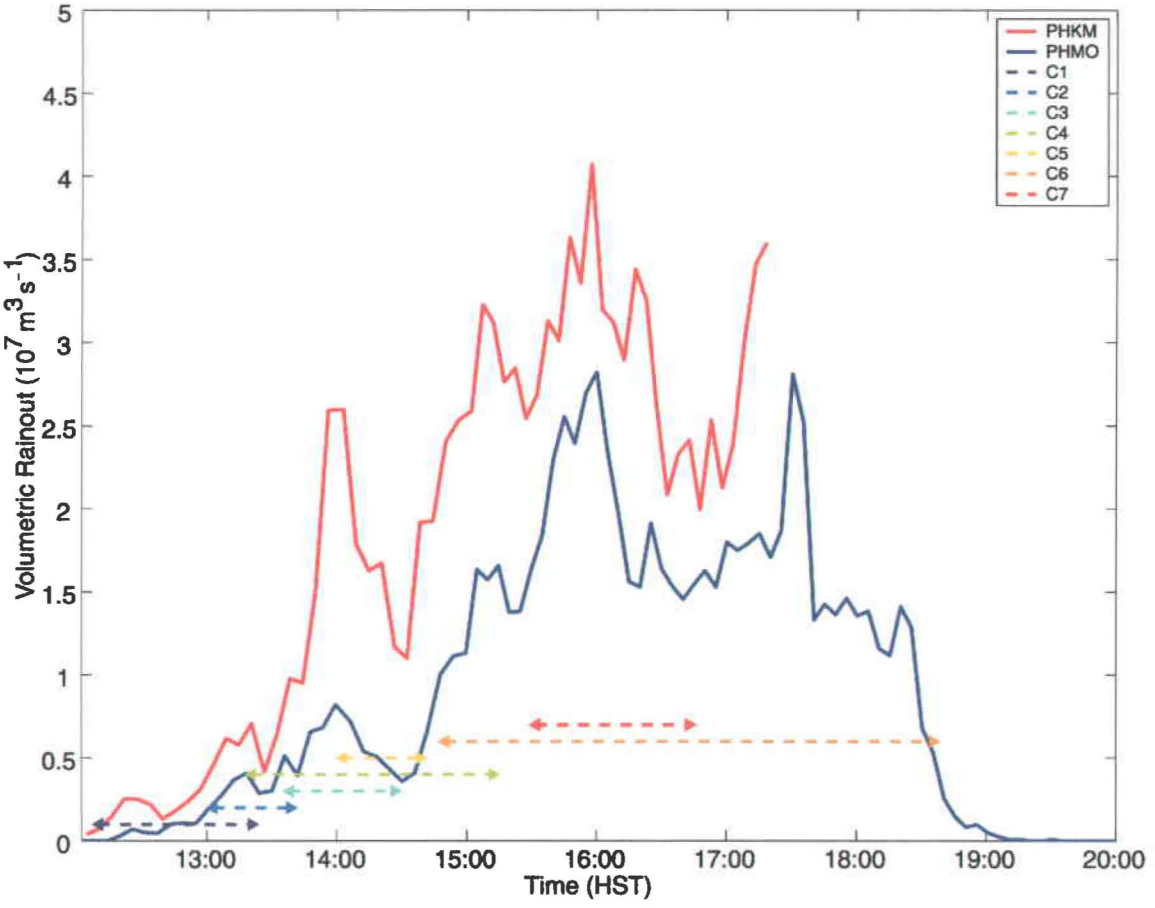

Figure 7. Volumetric Rainout of the Hana Storm. Derived from the PHMO and PHKM radars using Rosenfeld et al. (1993) tropical convective Z-R ($Z = 250\ R^{1.2}$) relationship with a reflectivity cap of 51 dBZ. Arrow lines denotes the period of a cell's existence.

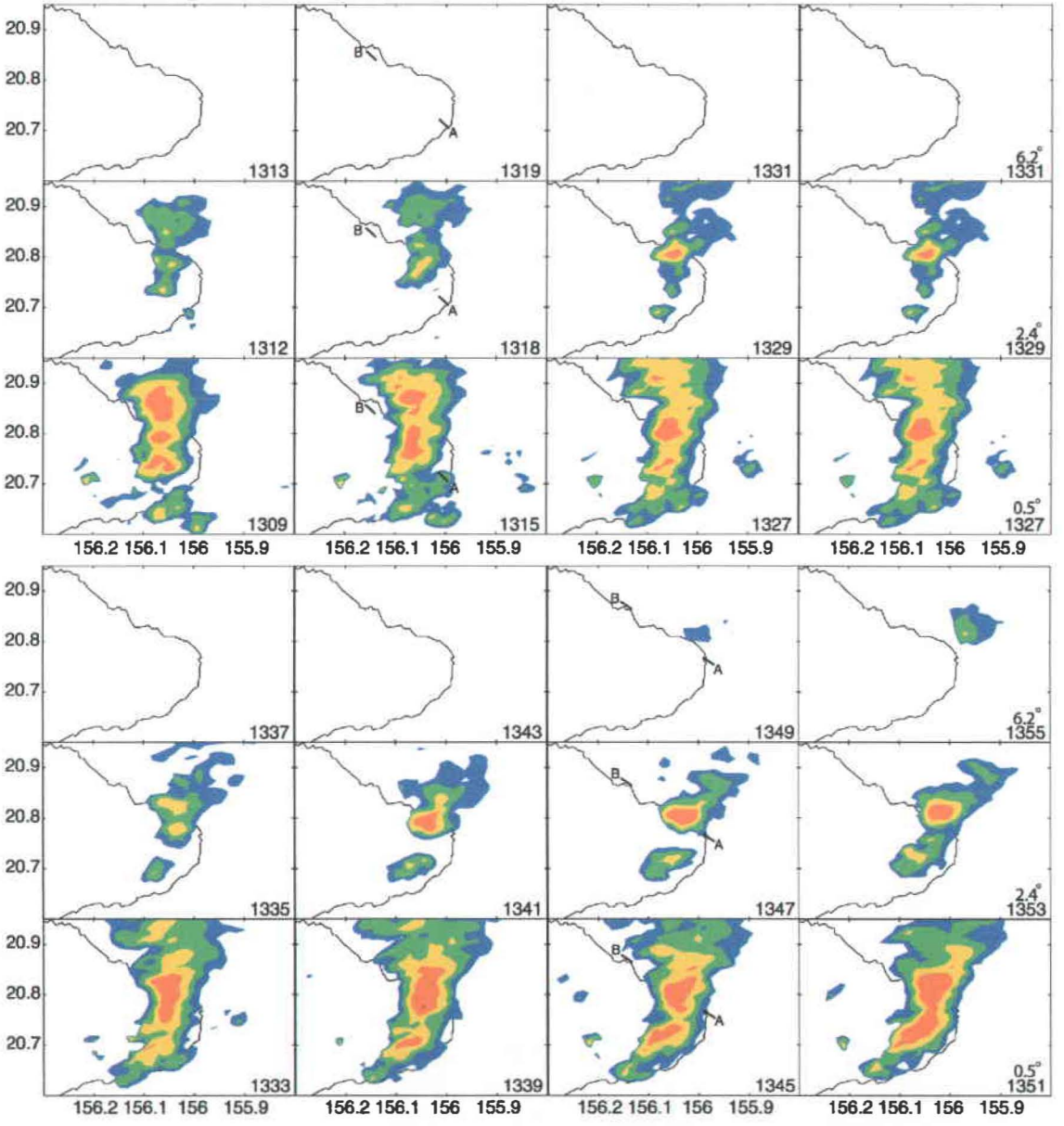

Figure 8. Reflectivity PPI for the developing stage (1309-1409 HST) of the Hana Storm. Sequence of PPIs at 0.5°, 2.4°, and 6.4° elevation angles for PHKM, roughly correspond to 2.5, 4.5 and 10 km above MSL respectively. Color shading represents 10 dBZ intervals in reflectivity starting with 15 dBZ Dashed lines represent 5 dBZ intervals for 50 and 60 dBZ. **A** and **B** denote the location of the vertical cross section (RHI) taken.

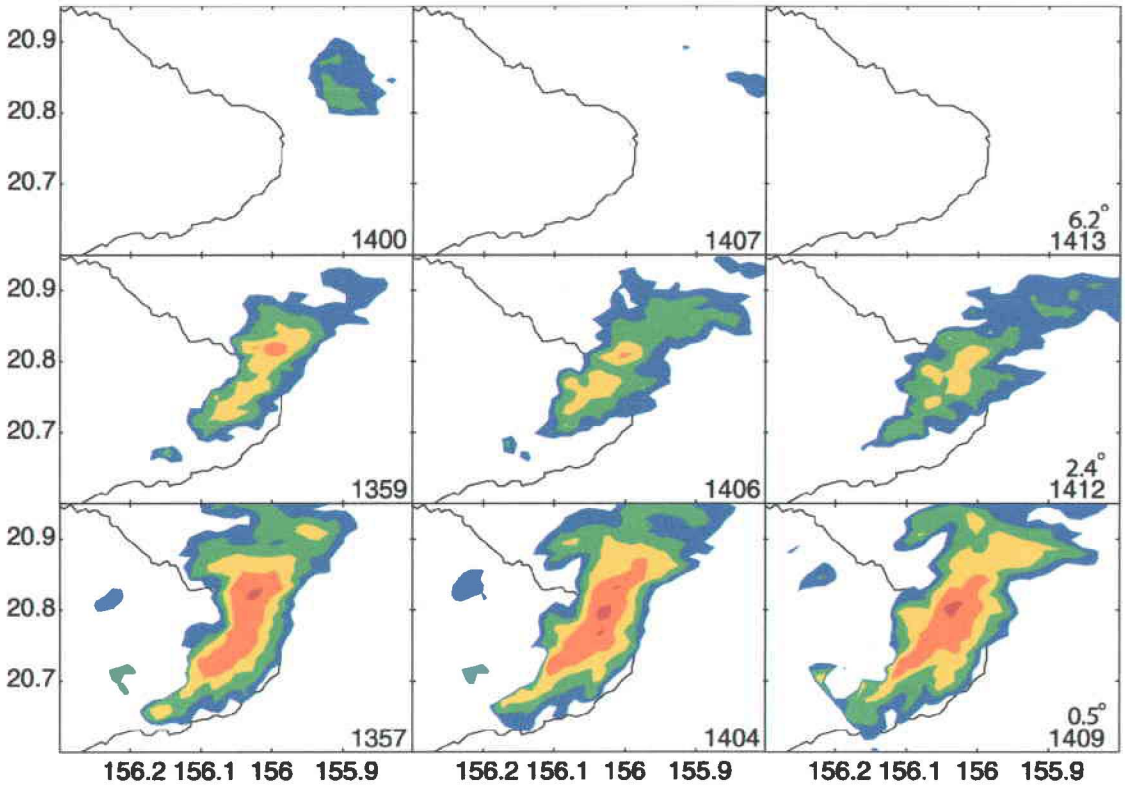

Figure 8 continued. Reflectivity PPI for the developing stage (1309-1409 HST) of the Hana Storm.

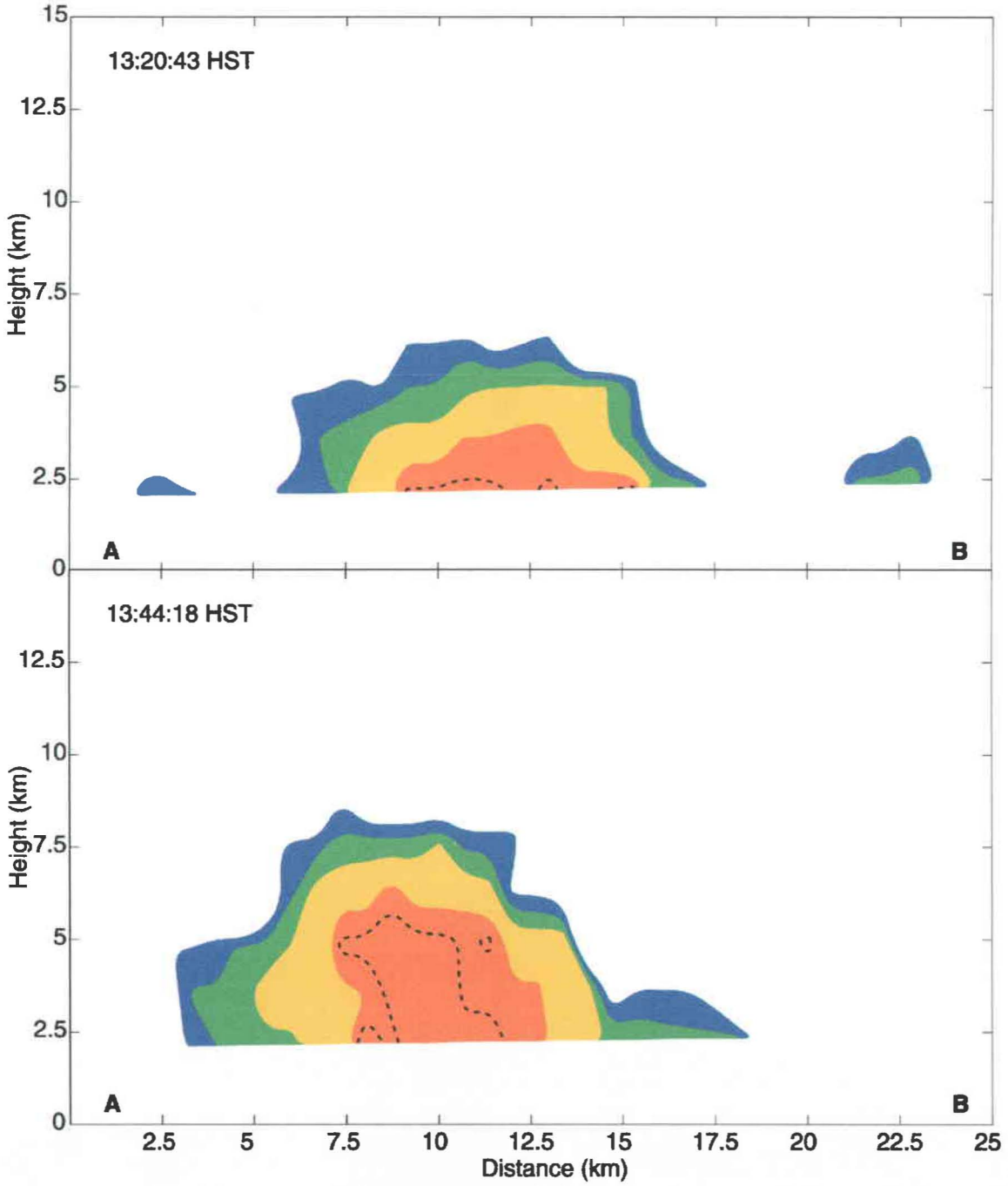

Figure 9. Vertical cross section taken during the developing stage. **A** denotes the southeast flank of the storm and **B** is the northwest flank (see Figure 8 for azimuth slice). Color shading represents 10 dBZ intervals in reflectivity starting with 15 dBZ. Dashed lines represents 50 dBZ contours.

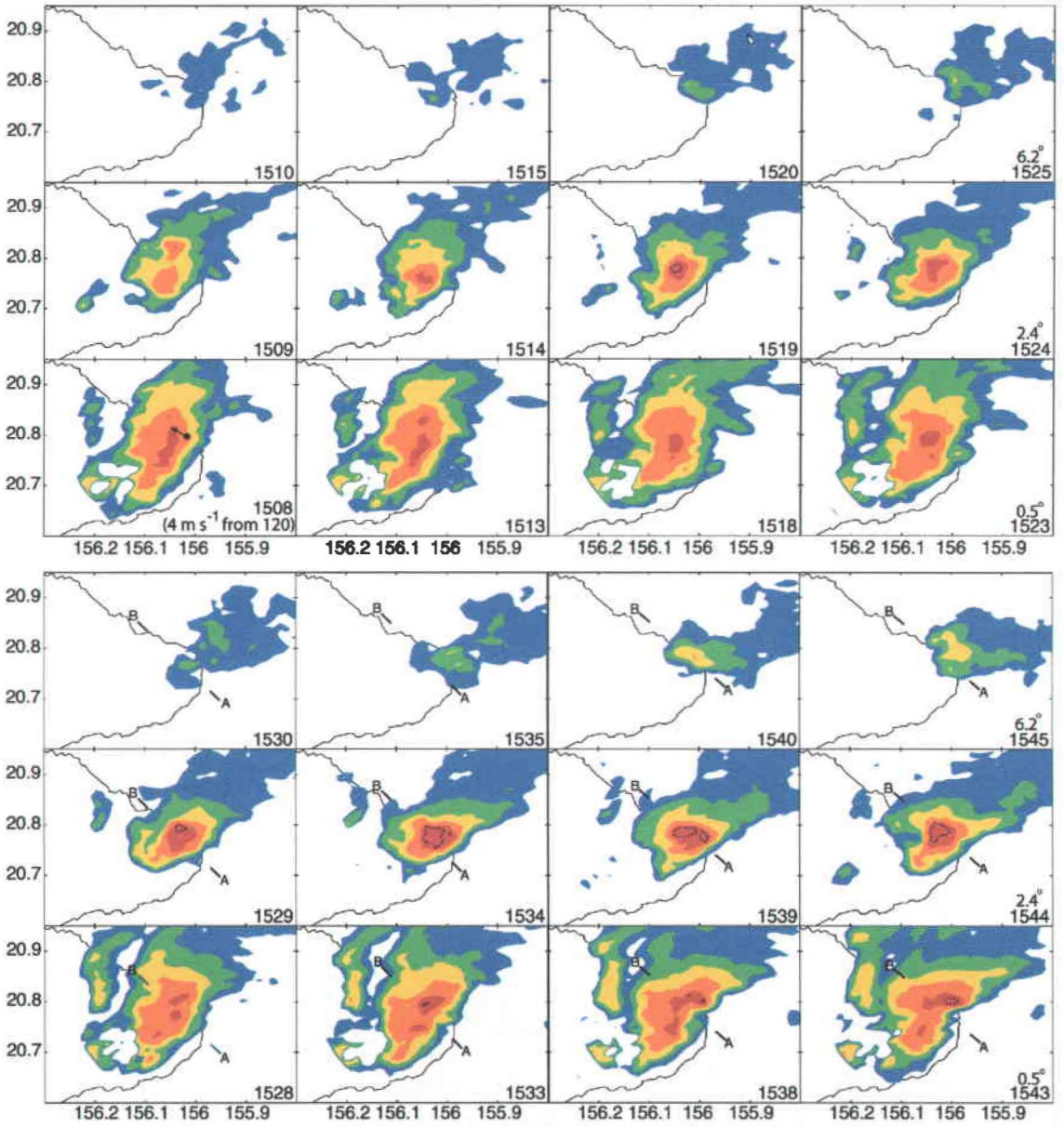

Figure 10. Reflectivity PPI for the mature stage (1508-1608 HST) of the Hana Storm. Sequence of PPI's at 0.5°, 2.4° and 6.4° elevation roughly correspond to 2.5, 4.5, and 10 km above MSL respectively. Color shading represents 10 dBZ intervals in reflectivity starting with 15 dBZ. Dashed lines represent 50 and 60 dBZ contours. A and B denote the location of the vertical cross section (RHI) azimuth taken (when applicable). Winds at Hana airport given at 1508 and 1608 HST.

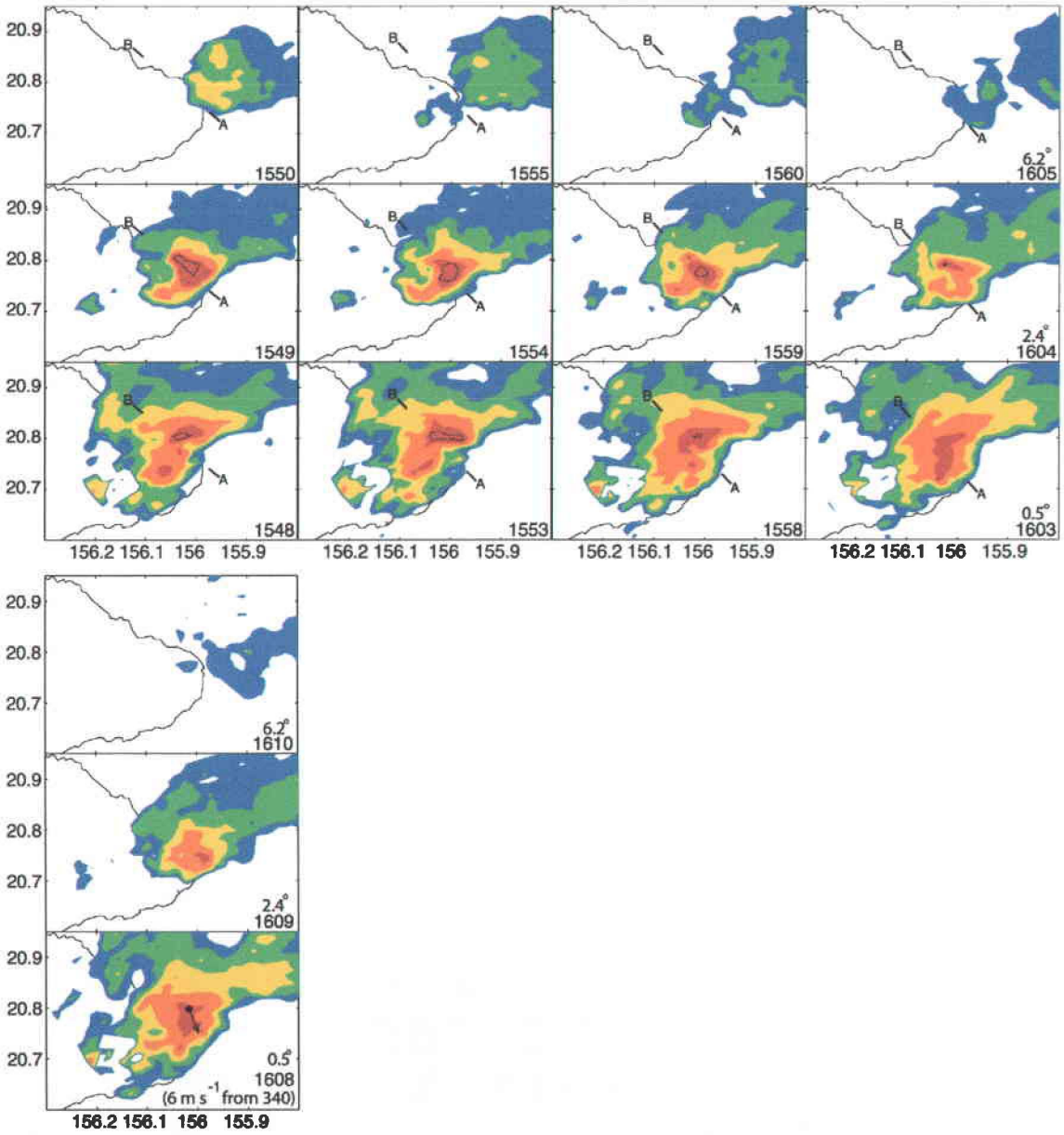

Figure 10 continued. Reflectivity PPI for the mature stage (1508-1608 HST) of the Hana Storm.

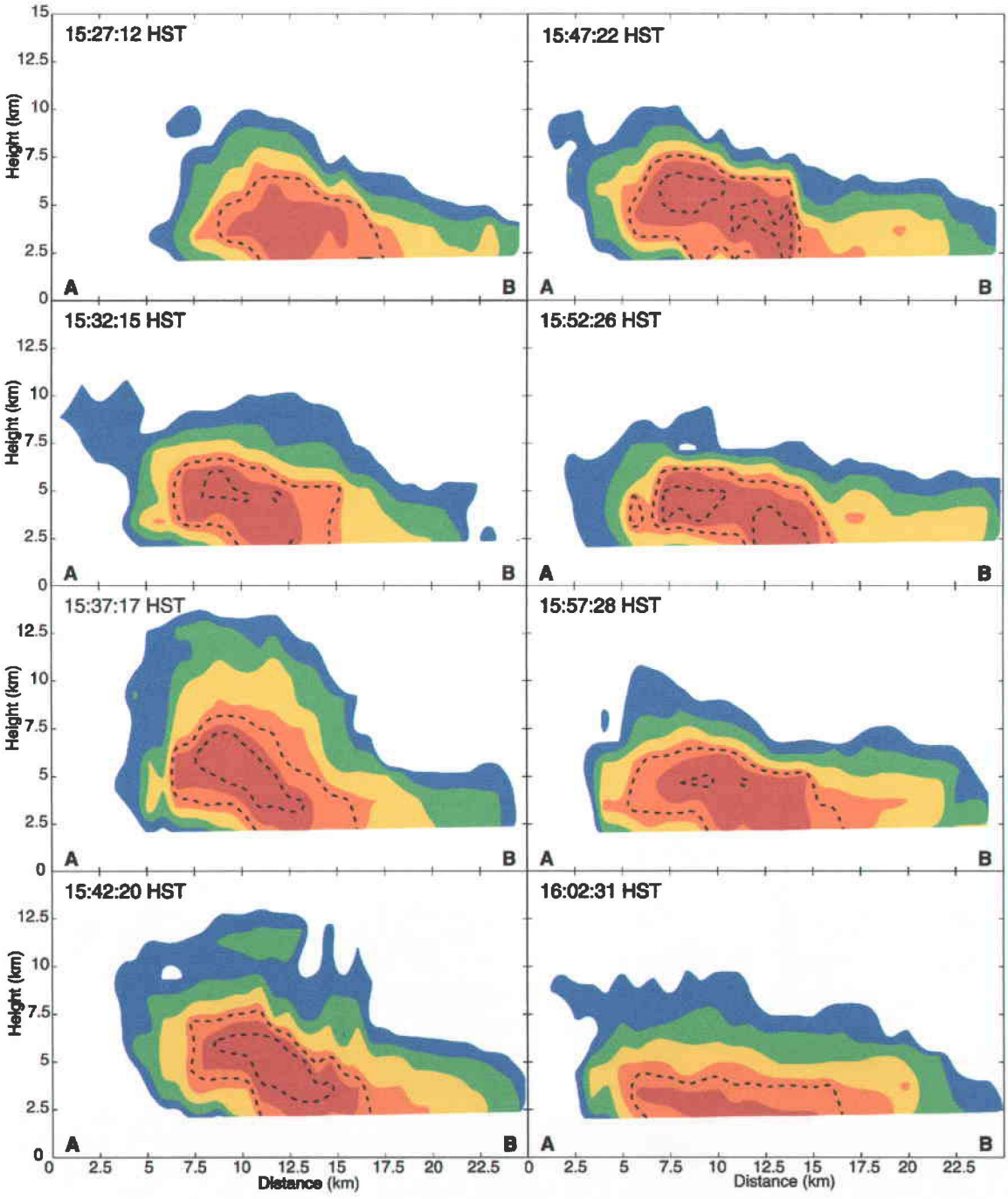

Figure 11. Sequence of RHI's for the mature stage. A denotes the southeast flank of the Hana Storm, whereas B is the northwest flank (see Figure 10 for azimuth slice). Color Shading represents 10 dBZ intervals in reflectivity starting with 15 dBZ. Dashed lines represents 50 and 60 dBZ contours.

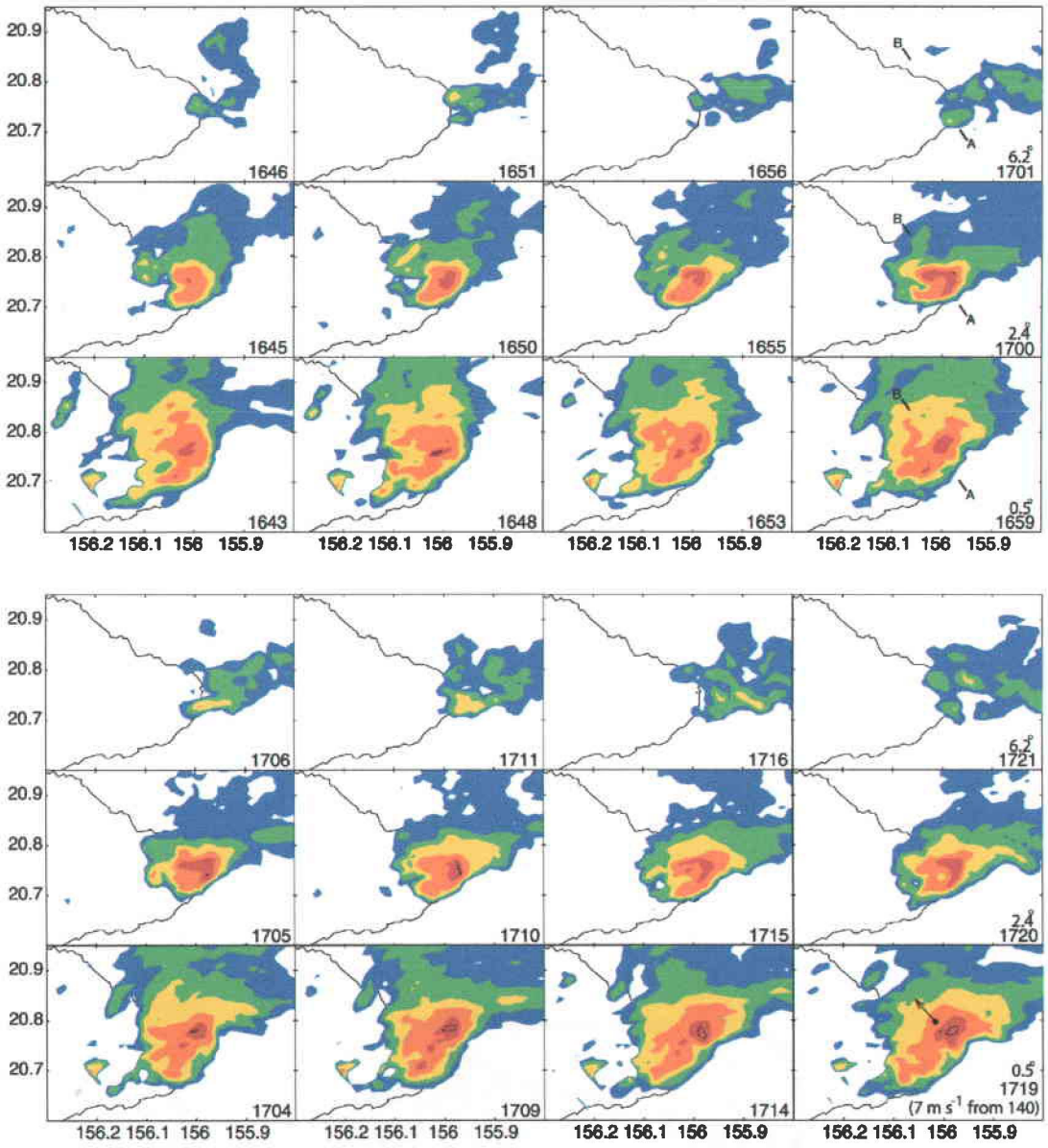

Figure 12. Reflectivity PPI for the dissipating stage (1643-1741 HST) of the Hana Storm. Sequence of PPI's at 0.5°, 2.4°, and 6.2° elevation angles by the PHKM radar and 0.5°, 1.5°, and 4.3° elevation angles by the PHMO radar roughly correspond to 2.5, 4.5, and 10 km above MSL. Color shading represents 10 dBZ intervals in reflectivity starting with 15 dBZ. Dashed lines represent 50 and 60 dBZ contours. A and B denote the location of the vertical cross section (RHI) azimuth taken (when applicable). Hana winds given at 1719 HST.

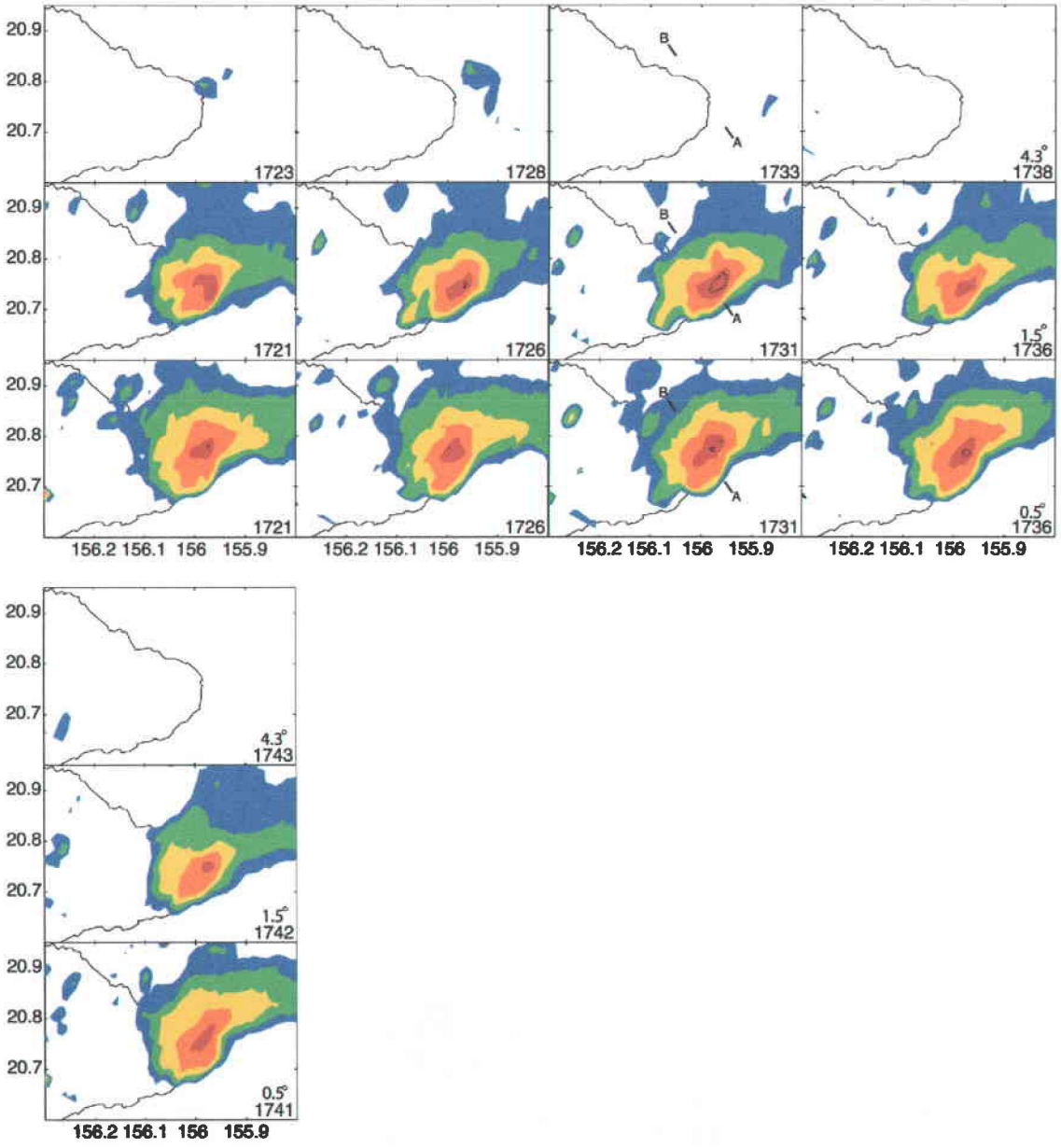

Figure 12 continued. Reflectivity PPI for the dissipating stage (1643-1741 HST) of the Hana Storm

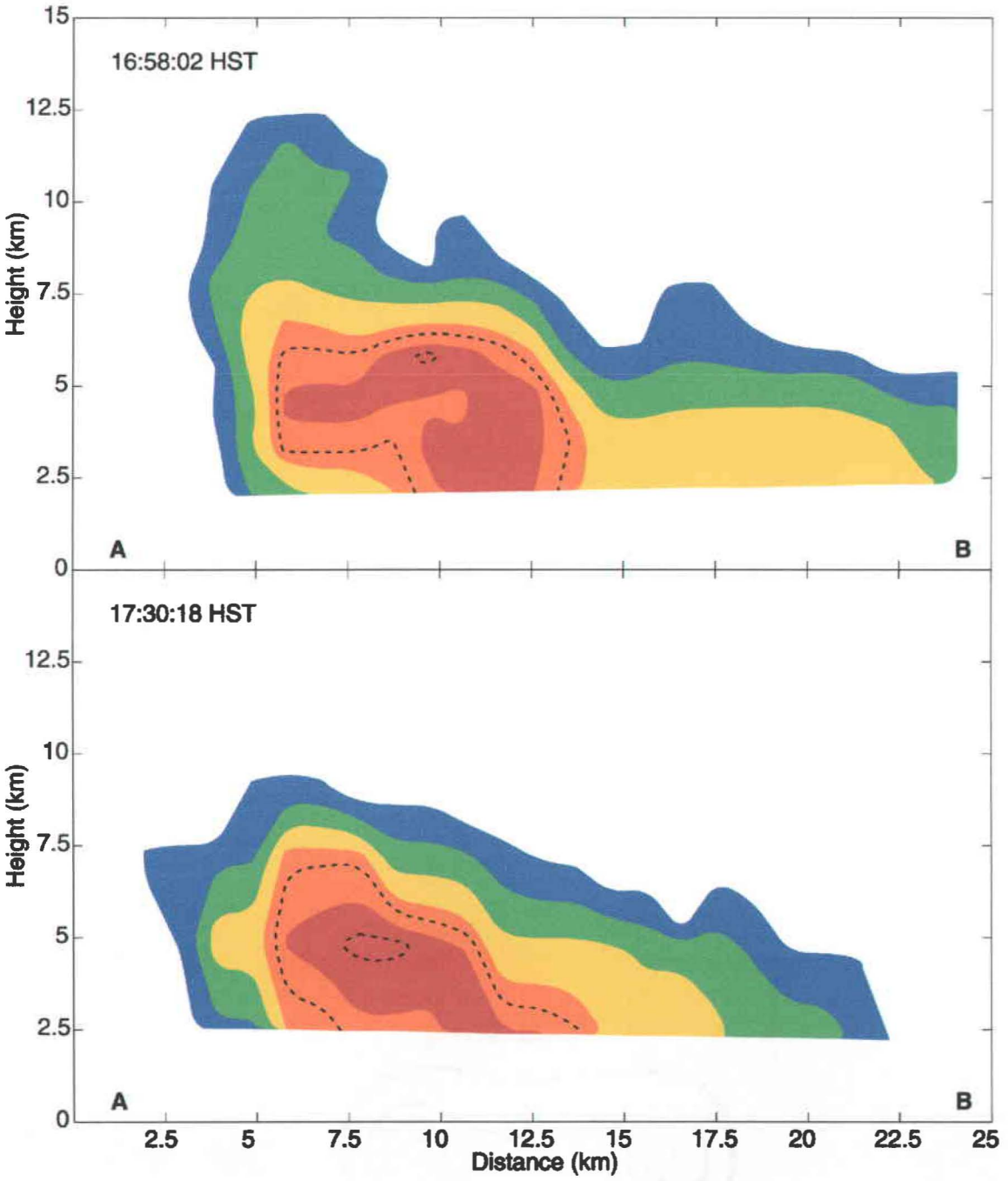

Figure 13. RHI's for the dissipating stage. A denotes the southeast flank of the Hana Storm, whereas B is the northwest flank (see Figure 12 for actual azimuth slice). Color shading represents 10 dBZ intervals in reflectivity starting with 15 dBZ. Dashed lines represents 50 and 60 dBZ contours.

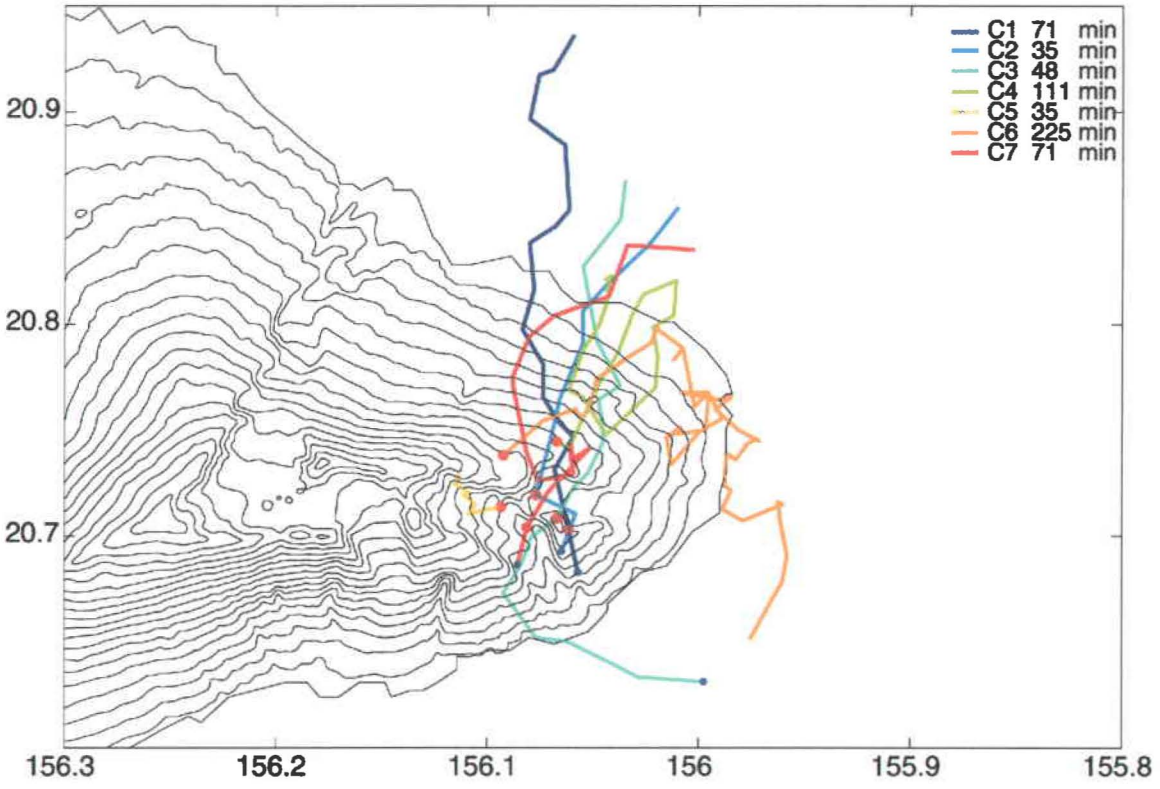

Figure 14. Tracks and origins of the seven cells embedded in the Hana Storm. Red dot denotes when echo reached cell status. Blue dot represents when echo was first tracked. Each line segment is approximately five to six minutes apart. Topography in 500 ft intervals.

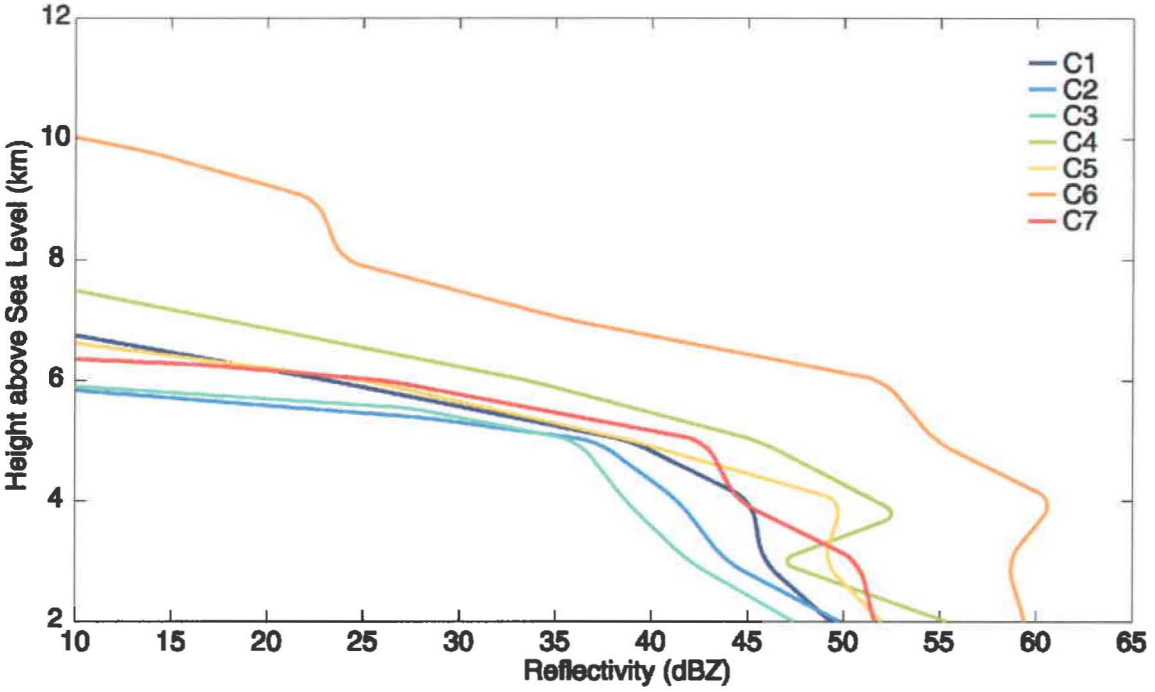

Figure 15. Vertical reflectivity profiles of the seven cells embedded in the Hana Storm.

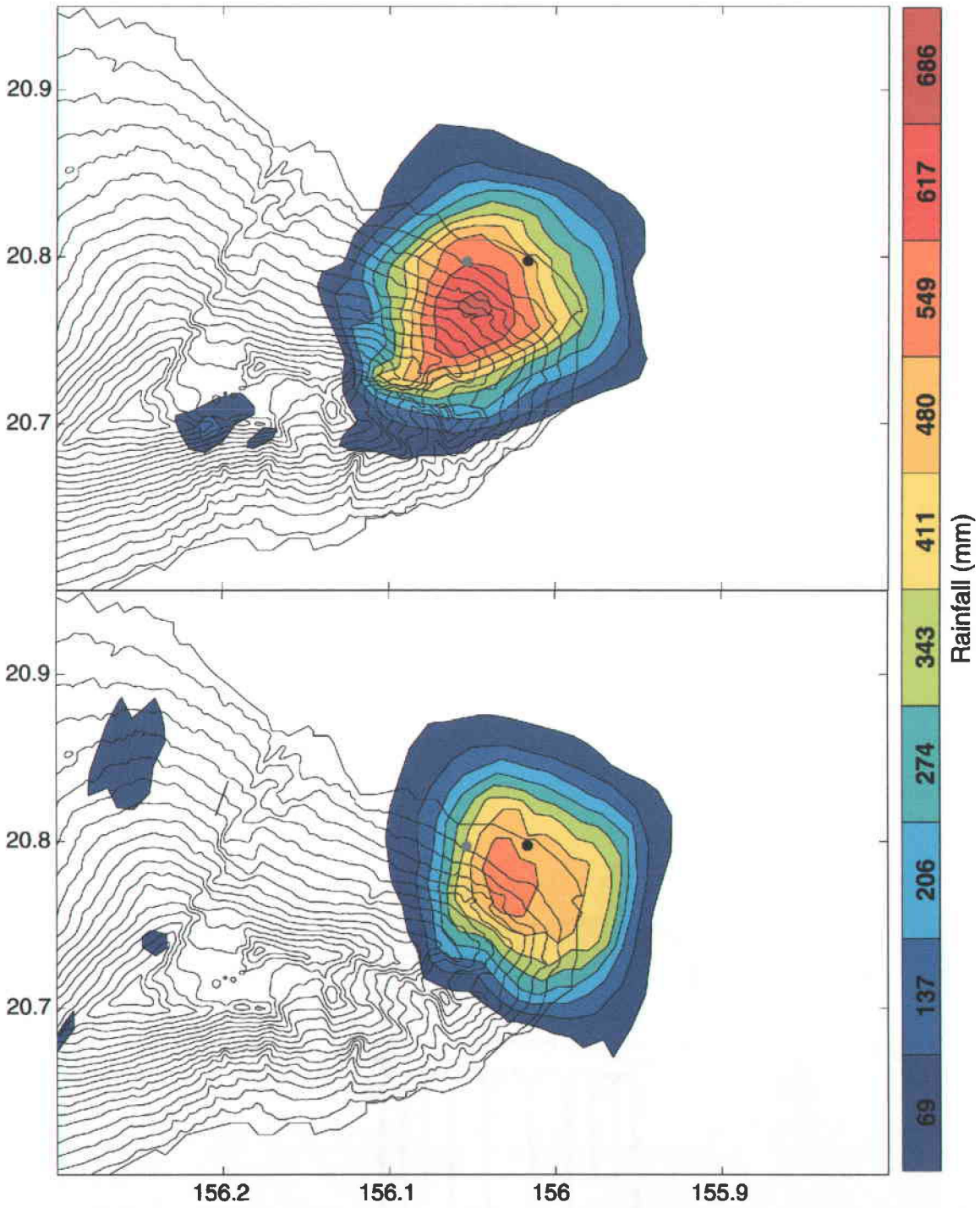

Figure 16. Hana Storm total precipitation (mm). The top panel is the PHKM STP for 1200 HST to 1719 HST, while the bottom panel is the PHMO STP for 1200 HST to 1900 HST. Derived using Rosenfeld et al. (1993) tropical convective Z-R ($Z = 250\ R^{1.2}$) relationship with a reflectivity cap of 51 dBZ. Black dot represents the Hana rain gage, while the gray dot depicts the approximate location of John Vares' rain gage. Topography intervals are 500 ft.

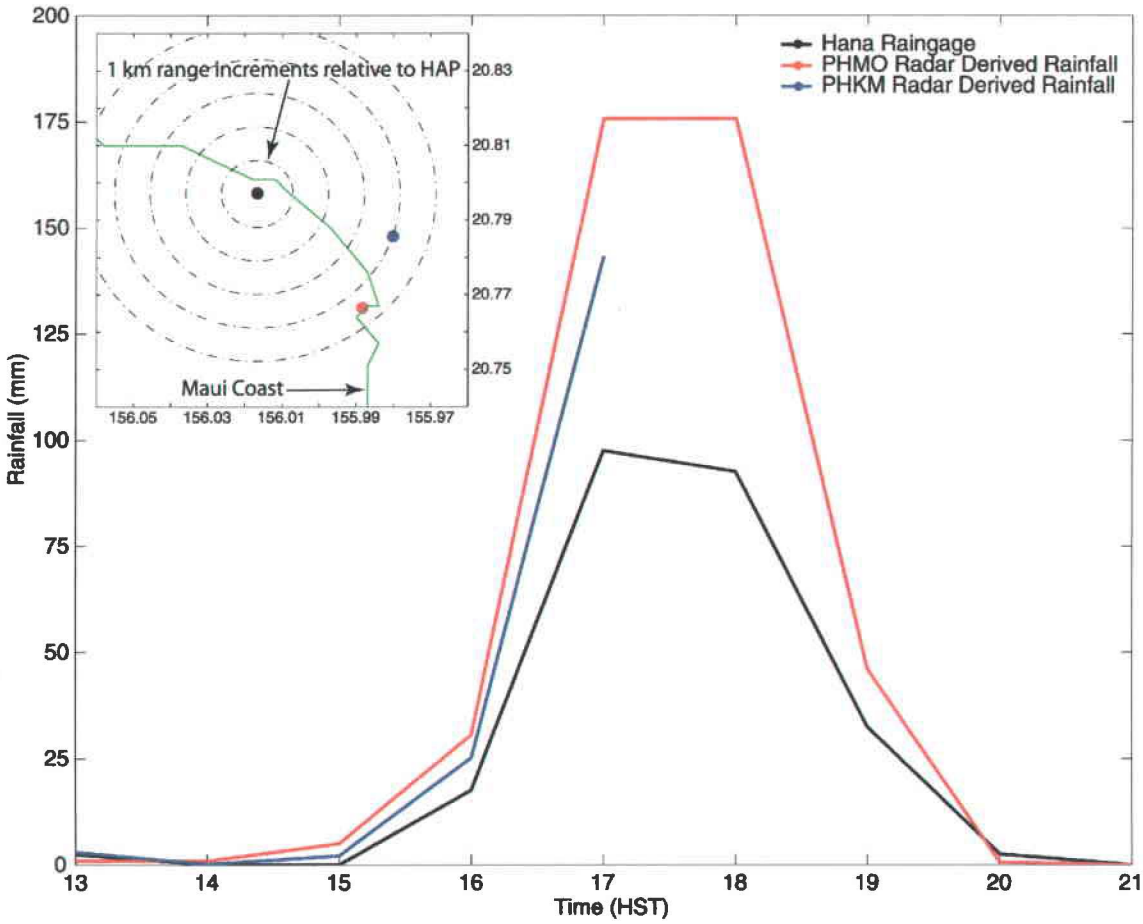

Figure 17. The PHKM and PHMO best-fit bin and the Hana rain gage hourly rainfall. The inset in the upper left corners shows the location of the Hana rain gage and the PHMO and PHKM best-fit bins. Derived using Rosenfeld et al. (1993) tropical convective Z-R ($Z = 250\ R^{1.2}$) relationship with a reflectivity cap of 51 dBZ.

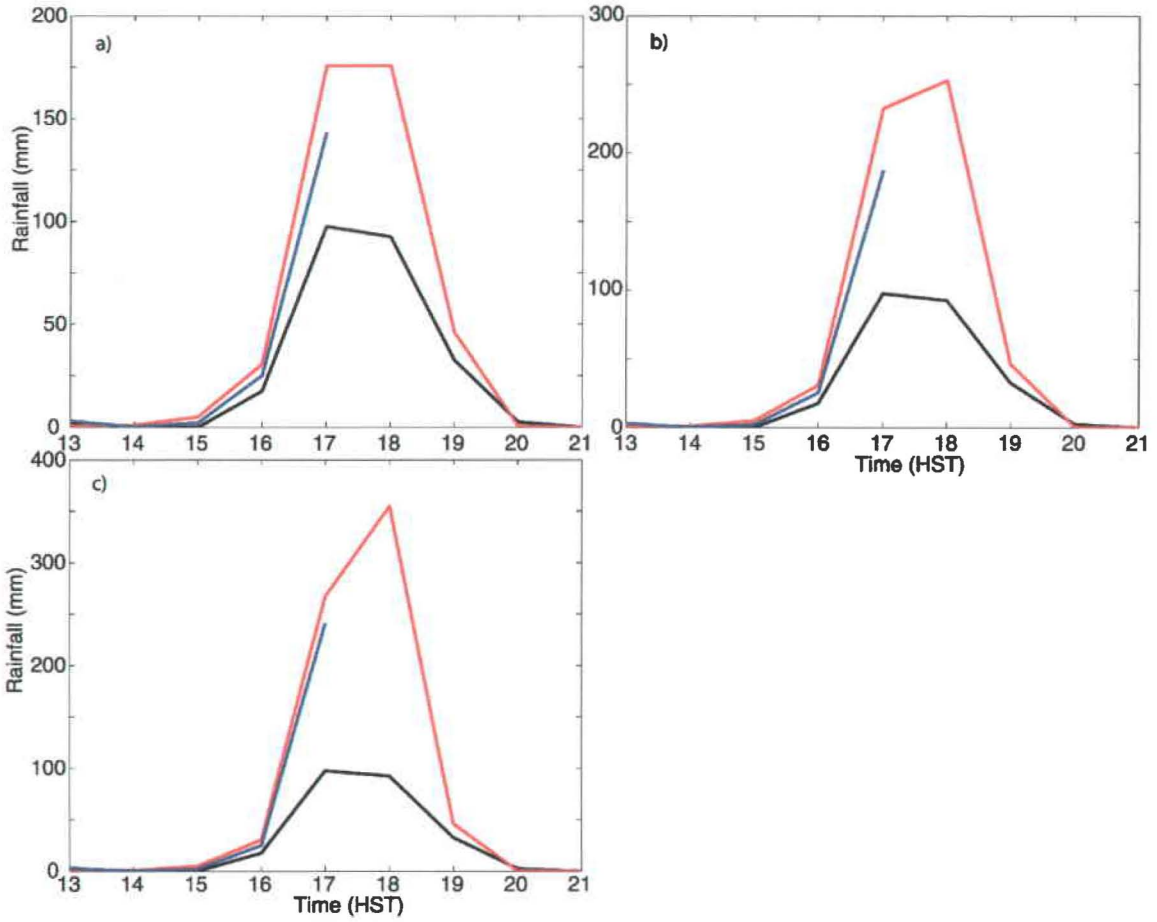

Figure 18. Best-fit bin versus the Hana rain gage using a constant Z-R relationship, but varying the reflectivity cap. Derived using Rosenfeld et al. (1993) tropical convective Z-R ($Z = 250\ R^{1.2}$) relationship. a) 51 dBZ; b) 53 dBZ; c) 55 dBZ.

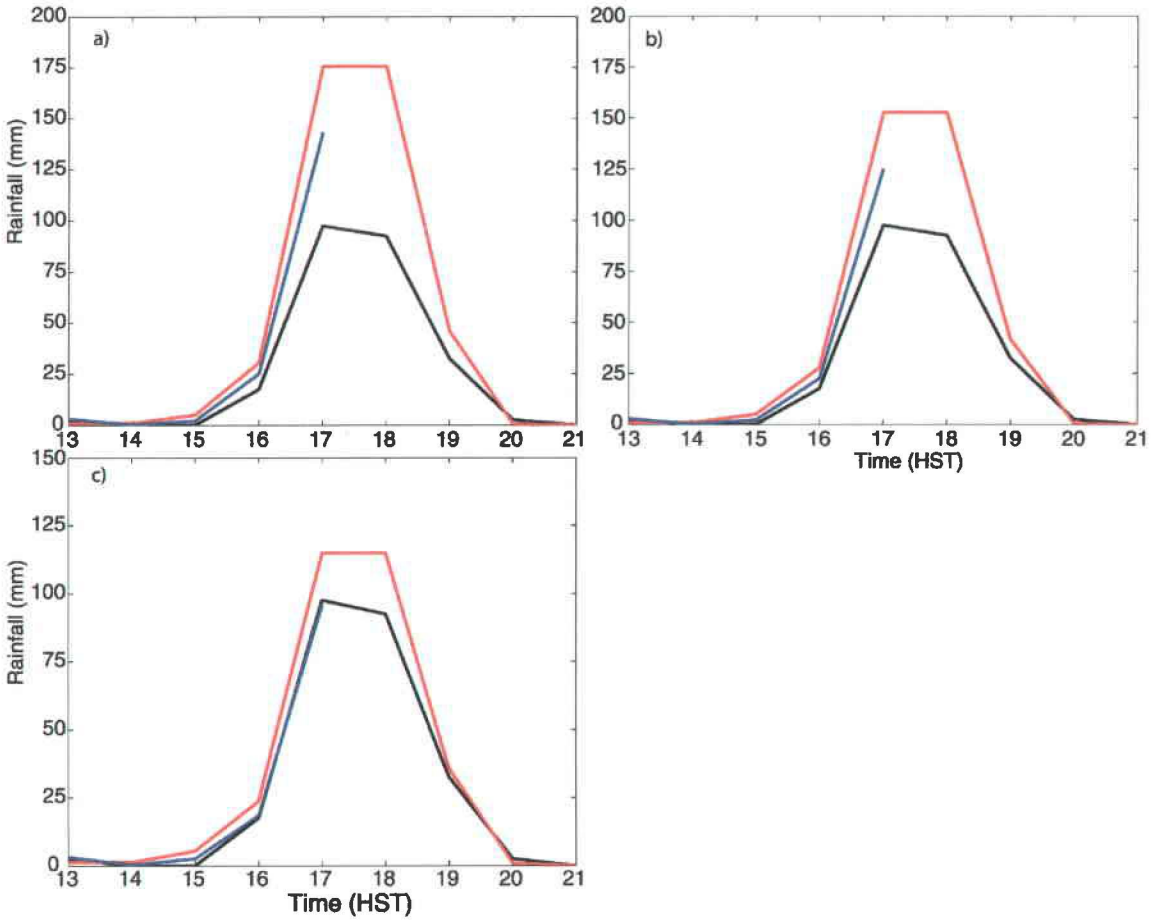

Figure 19. Best-fit bin versus the Hana rain gage using a constant reflectivity cap (51 dBZ) but varying the Z-R relationship. a) Tokay and Short (1996) ($Z = 139\ R^{1.43}$); b) Hudlow (1979) ($Z = 230\ R^{1.25}$); c) Rosenfeld et al. (1993) ($Z = 250\ R^{1.25}$).

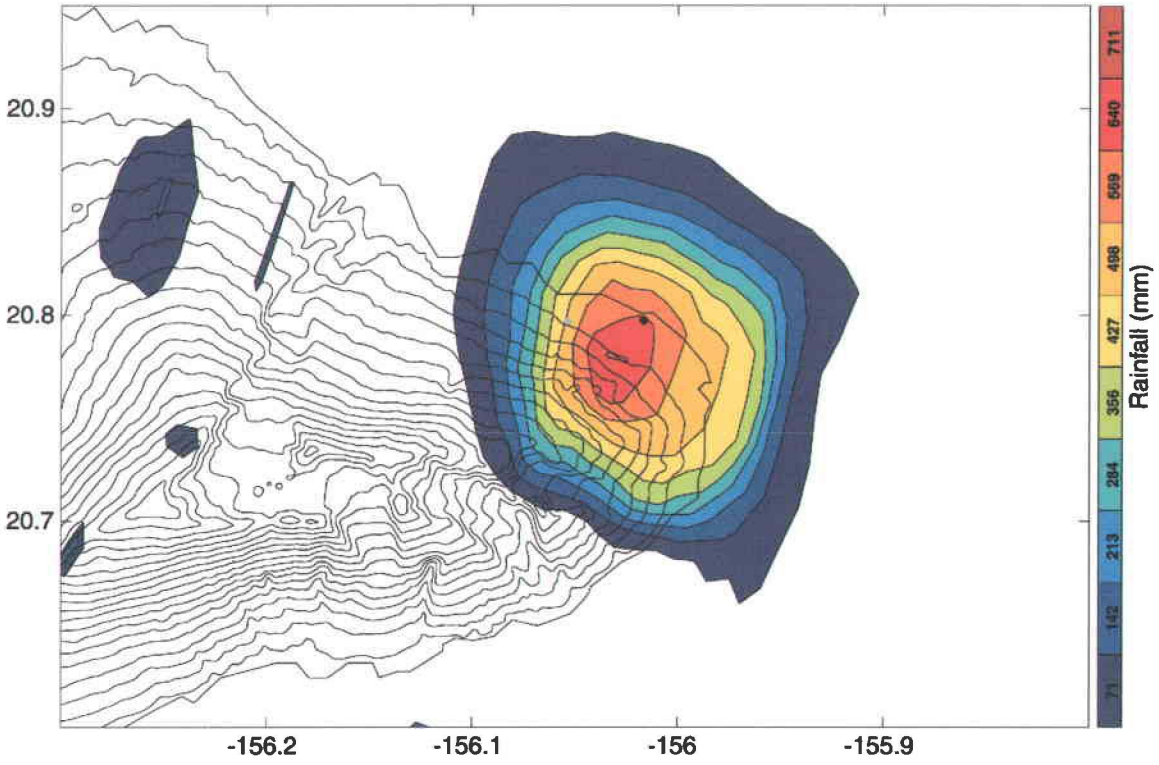

Figure 20. Corrected Hana Storm total precipitation (mm) for 1200 HST to 1900 HST. Derived from the PHMO radar using Tokay and Short's (1993) tropical convective Z-R ($Z = 139\ R^{1.43}$) relationship, with a reflectivity cap of 51 dBZ, and a 3.5 dBZ increase in reflectivity to compensate for inhomogeneous beam filling. Black dot represents the Hana rain gage, while the gray dot depicts the approximate location of John Vares' rain gage. Topography intervals are 500 ft.

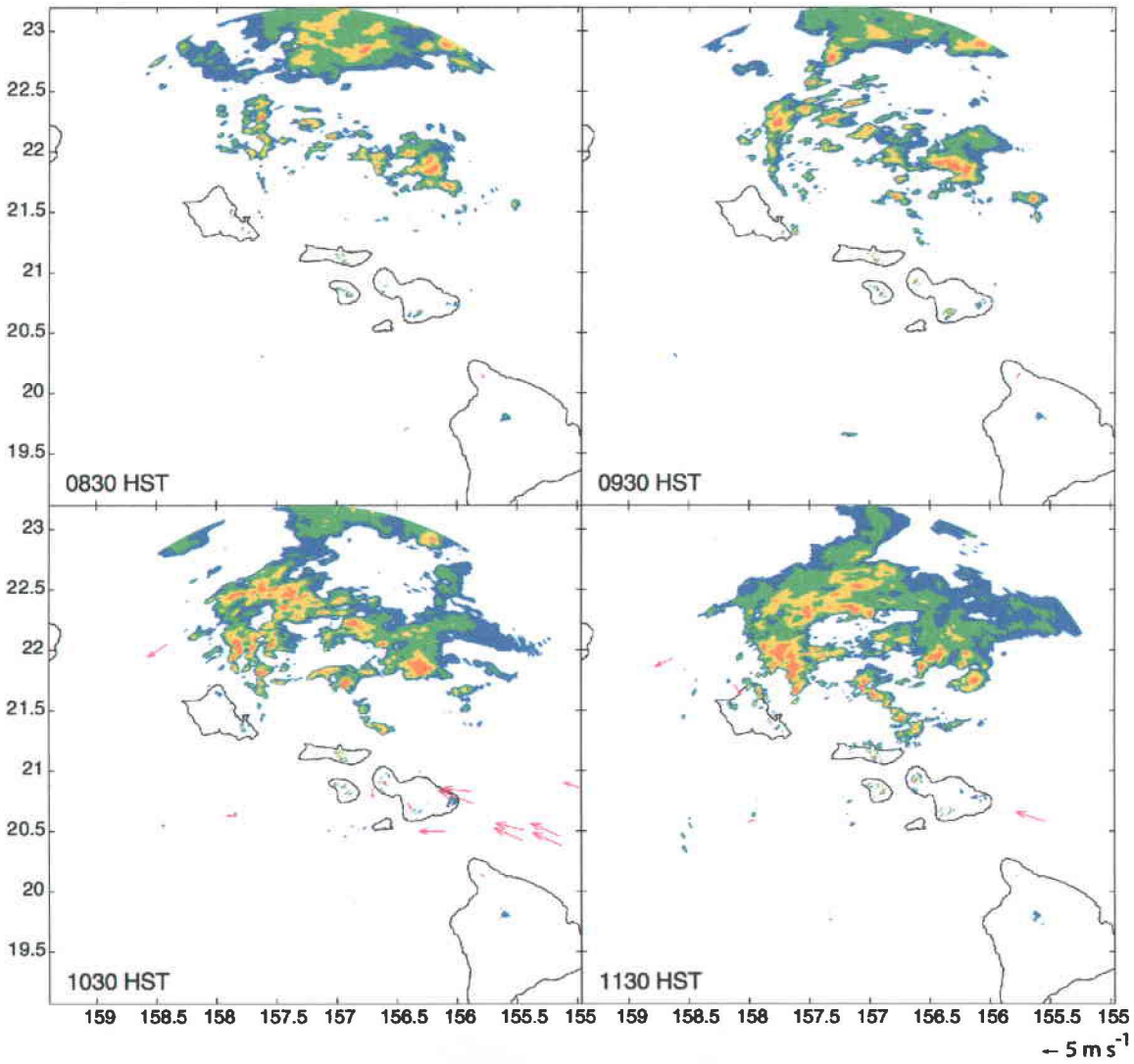

Figure 21. PHMO Base Reflectivity (0.5 deg elevation angle) and wind observations for 0830 HST 29 October 2000 through 1830 HST 29 October 2000. Time interval is approximately 30 minutes. Color shading represents 10 dBZ reflectivity intervals starting with 15 dBZ. Dashed lines represent 5 dBZ intervals for 50 and 60 dBZ. The purple arrows represent the cloud-drift low-level winds; red arrows are derived from the Velocity Azimuth Display; and the black arrows are the winds observed at the Automated

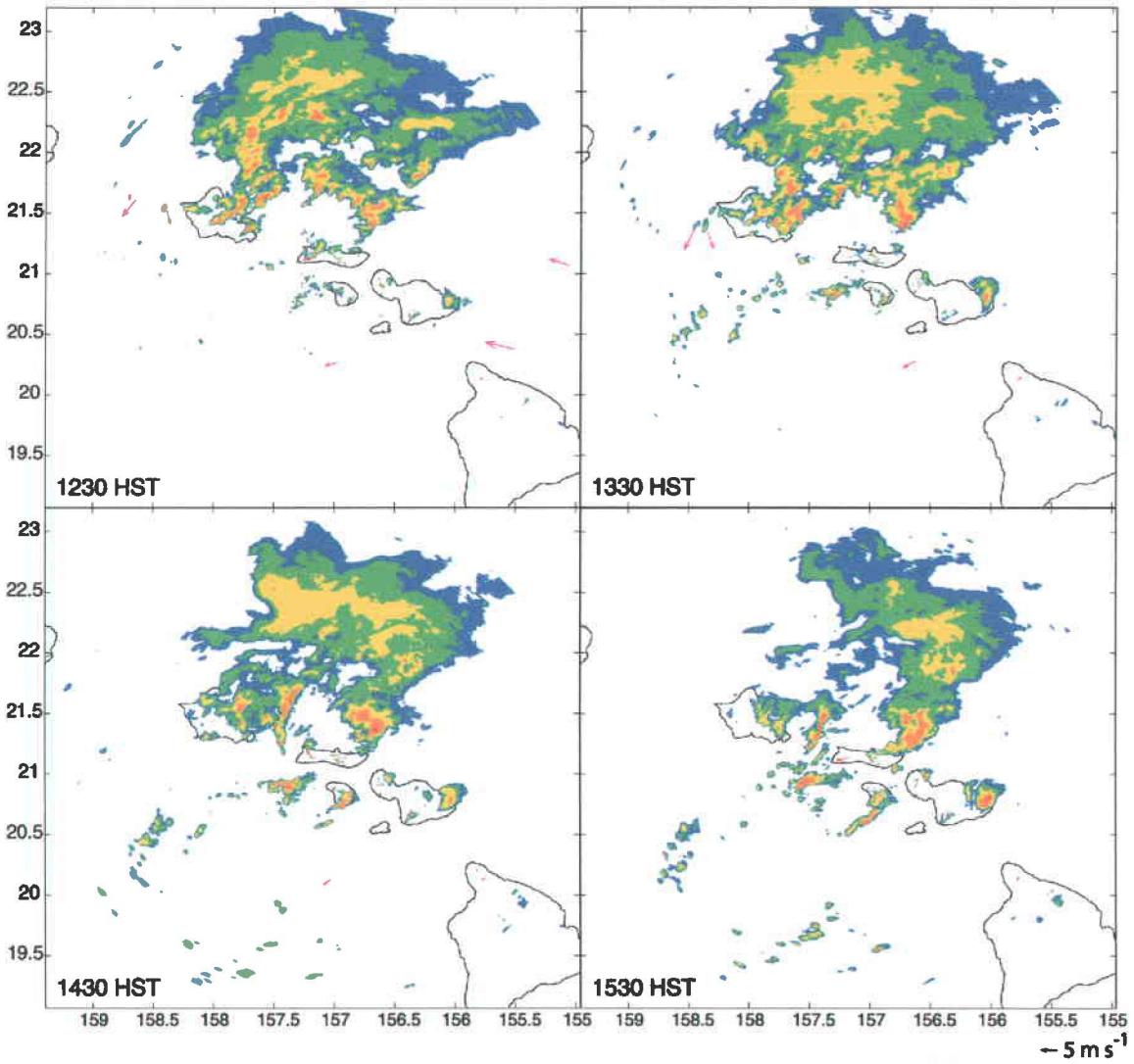

Figure 21 continued. PHMO base reflectivity and wind observation for 29 October 2000.

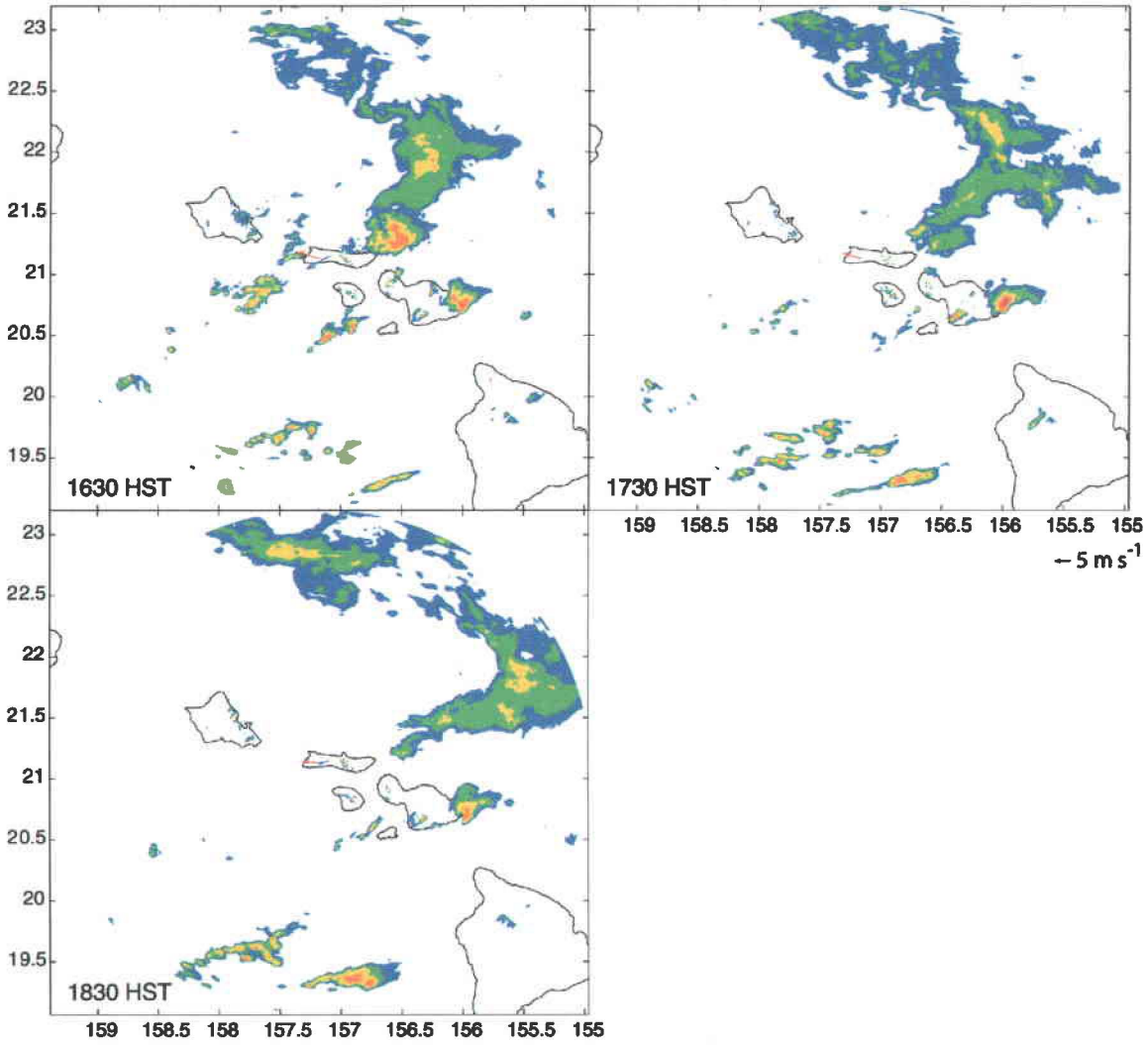

Figure 21 continued. PHMO base reflectivity and wind observation for 29 October 2000.

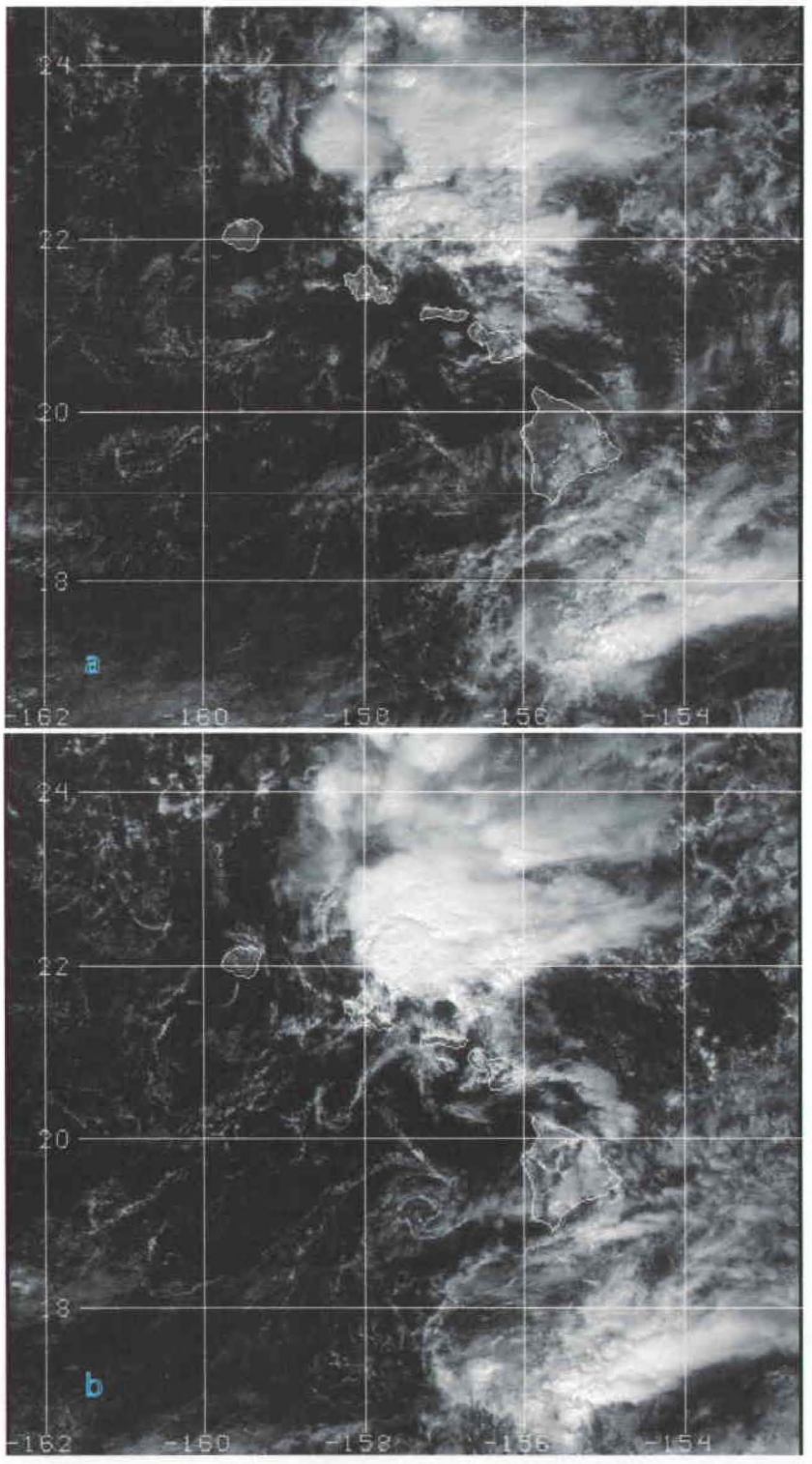

Figure 22. GOES-10 1 km visible imagery for 1000-1600 HST 29, October 2000. a) 1000 HST; b) 1200 HST; c) 1400 HST; d) 1600 HST.

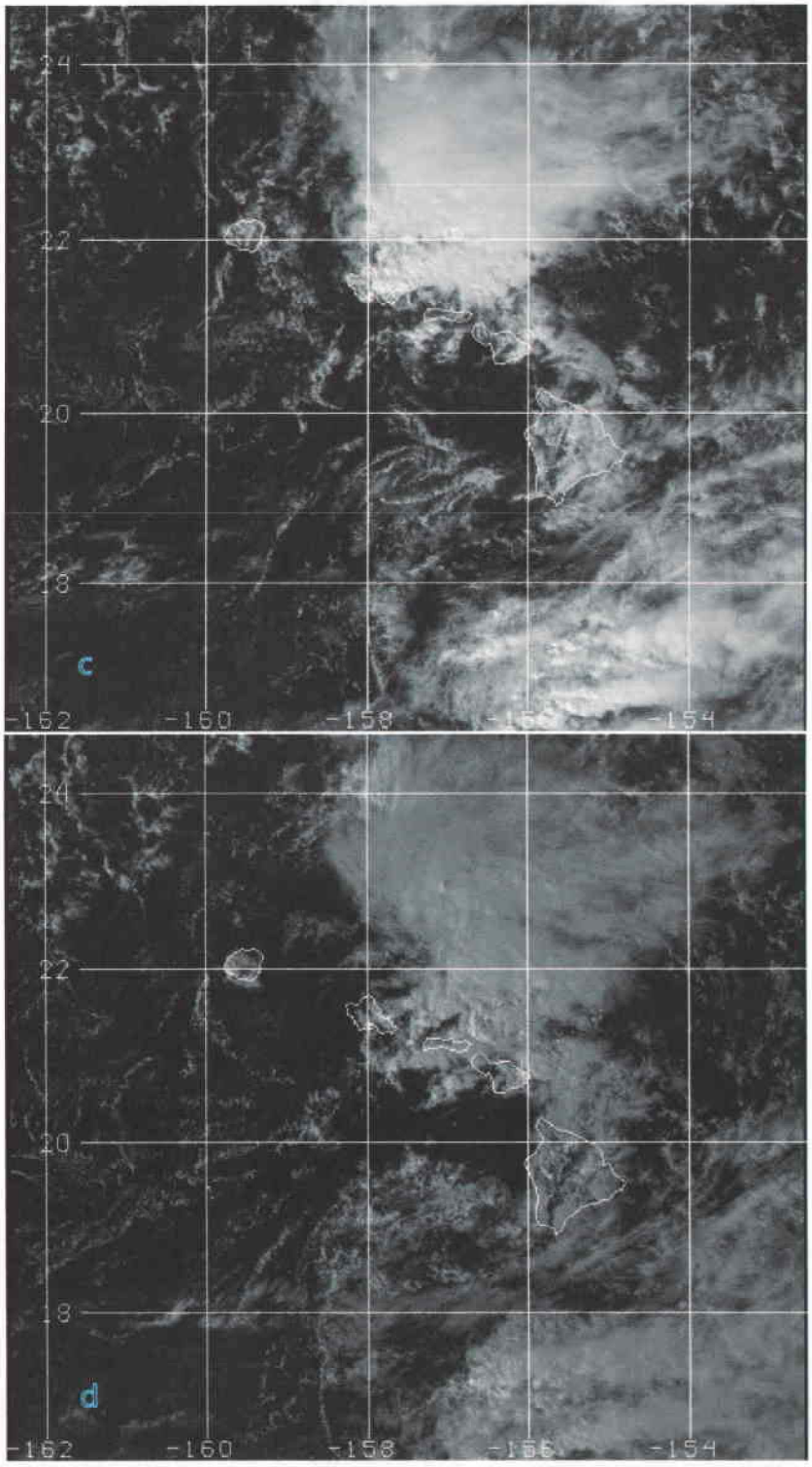

Figure 22 continued.

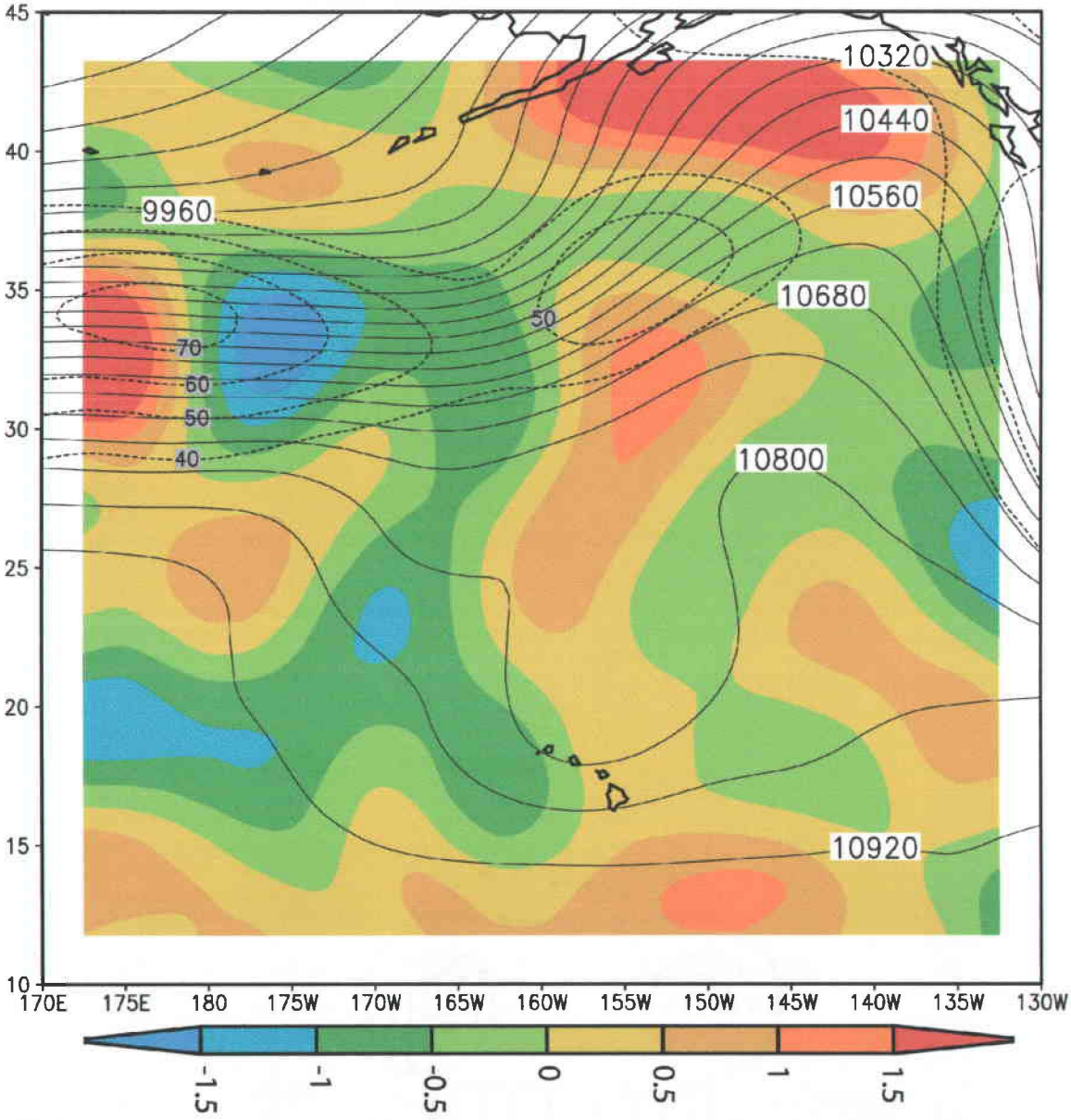

Figure 23. Synoptic Scale 250 hPa Isoheights (m), Winds (m s^{-1}), and Divergence (s^{-1}) Analysis for 1400 HST, 29 October 2000.

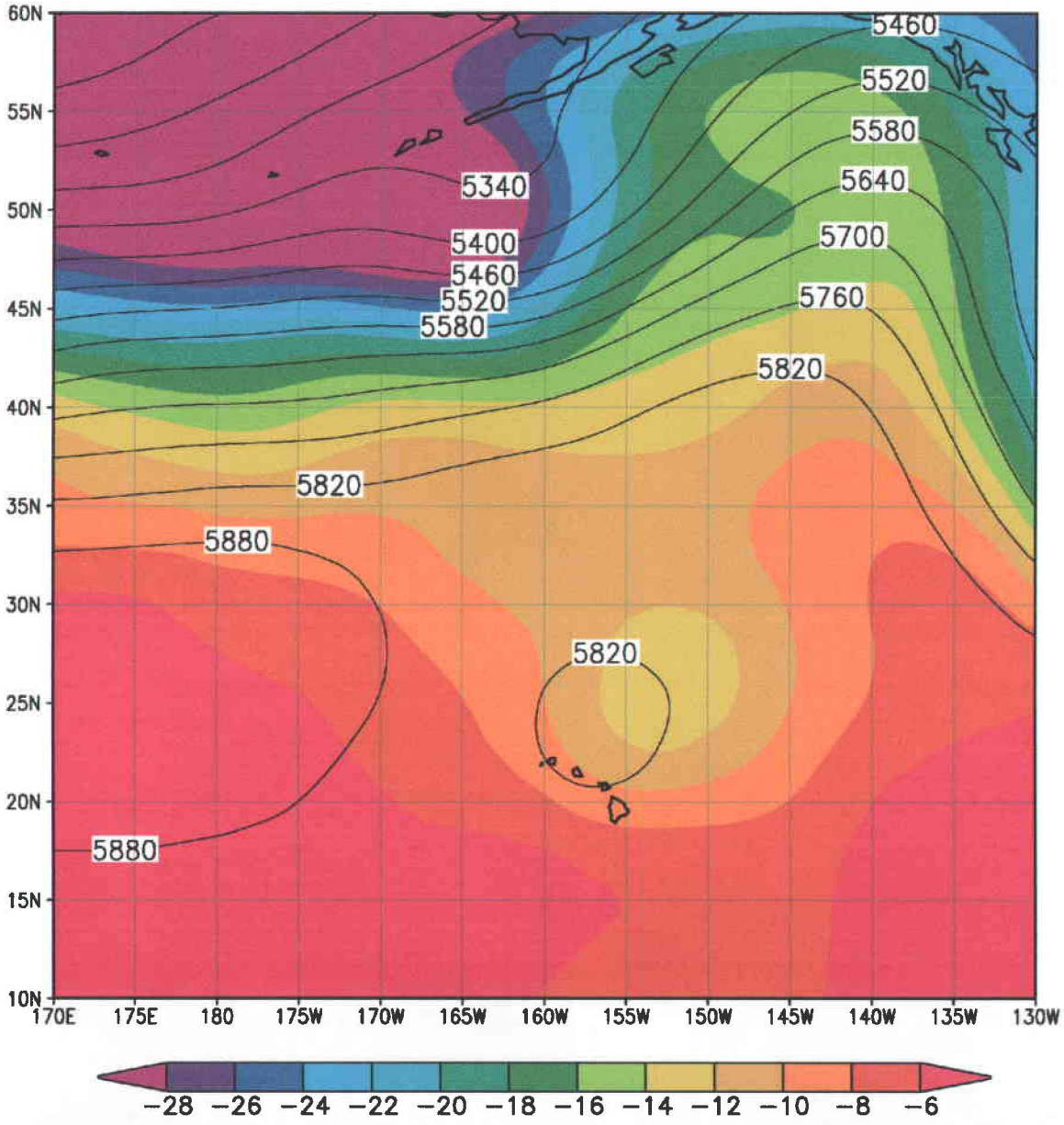

Figure 24. Synoptic scale 500 hPa heights (m) and temperature (°C) analysis for 1400 HST, 29 October 2000.

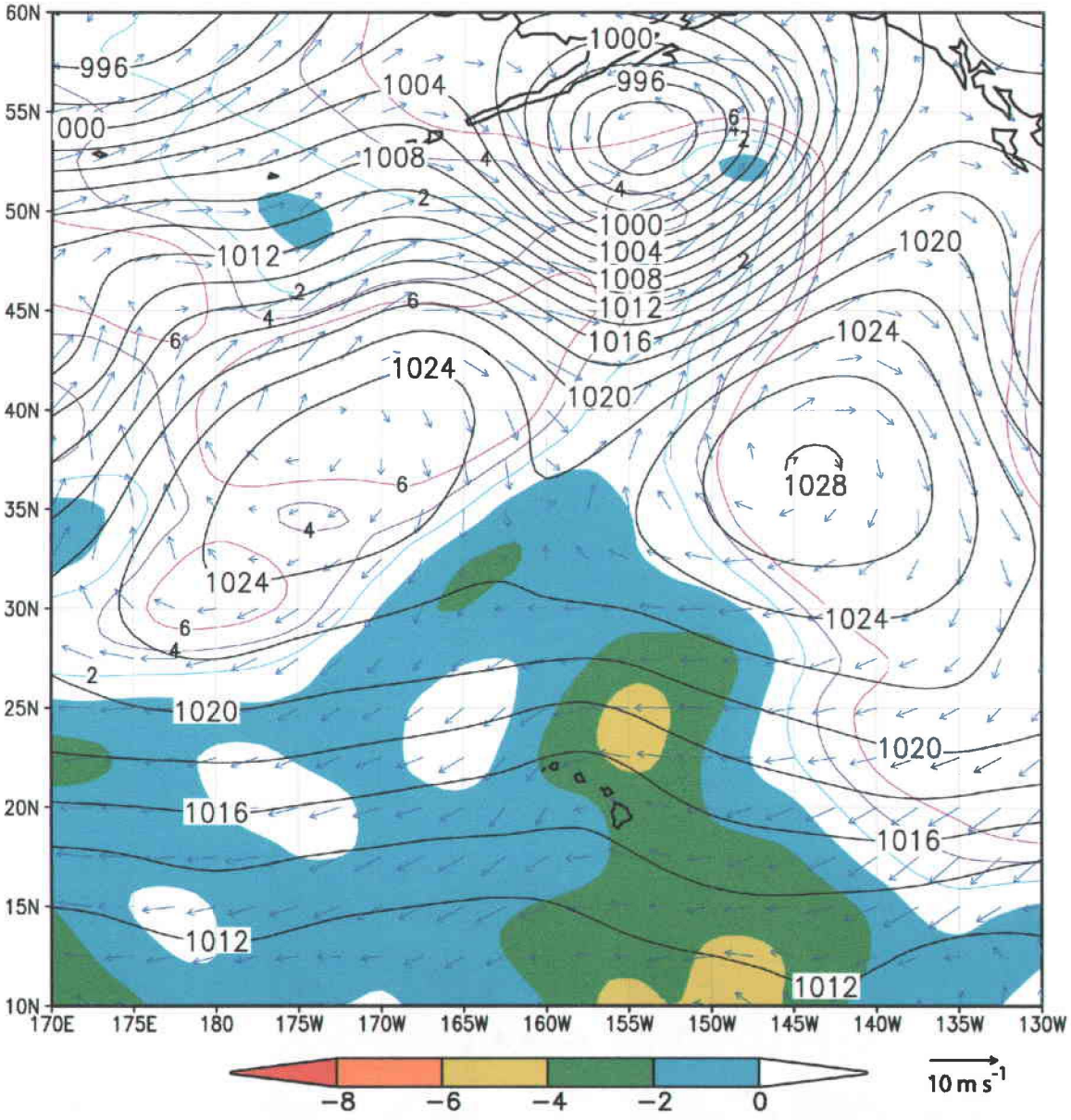

Figure 25. Synoptic scale surface winds (m s^{-1}), pressure (hPa), and lifted index (°C) analysis for 1400 HST, 29 October 2000.

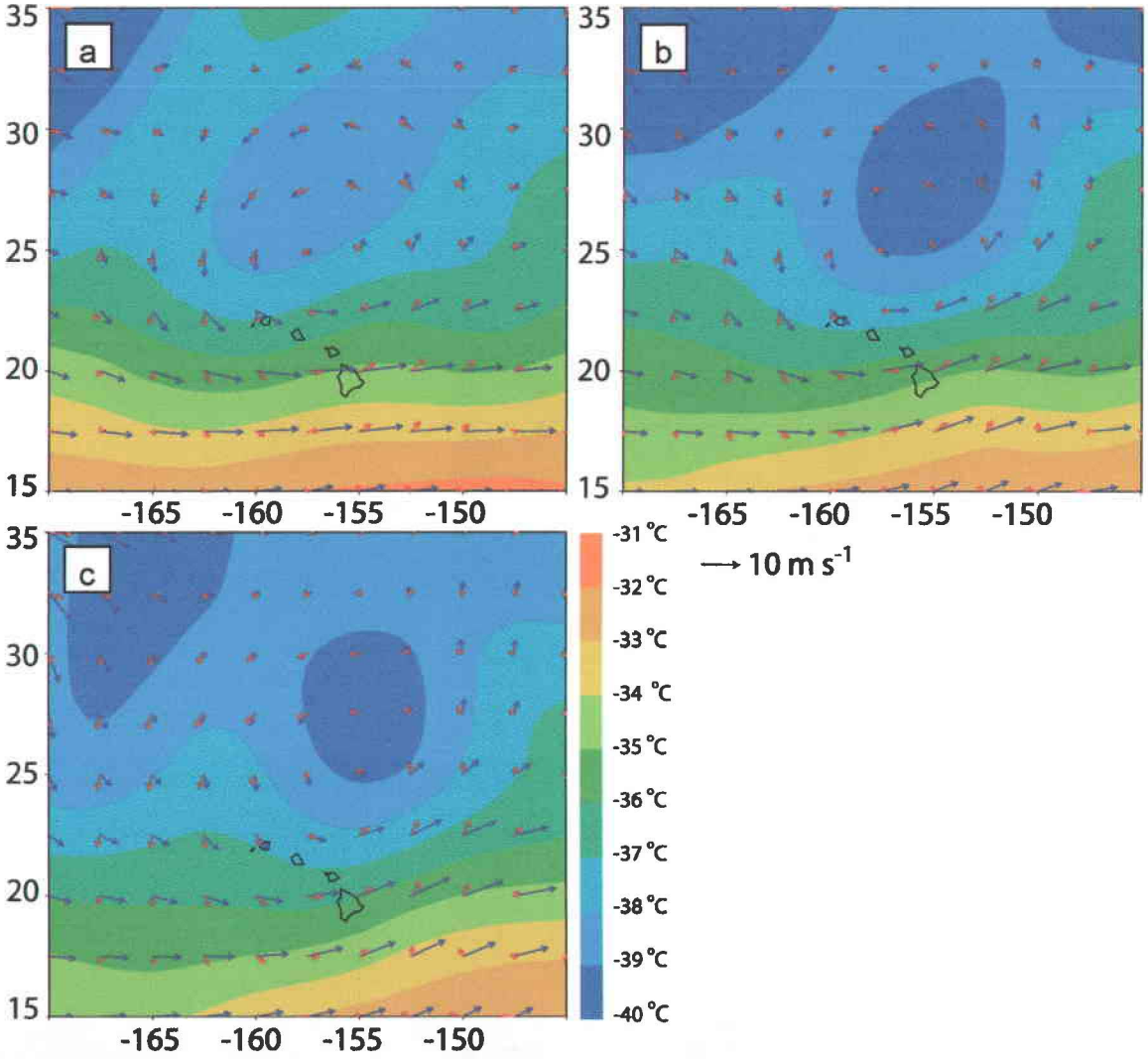

Figure 26. 250 hPa and 500 hPa level winds and 300 hPa temperatures. Red arrows denote 500 hPa winds and the purple arrows represent the 250 hPa winds. a) 0800 HST; b) 1400 HST; c) 2000 HST.

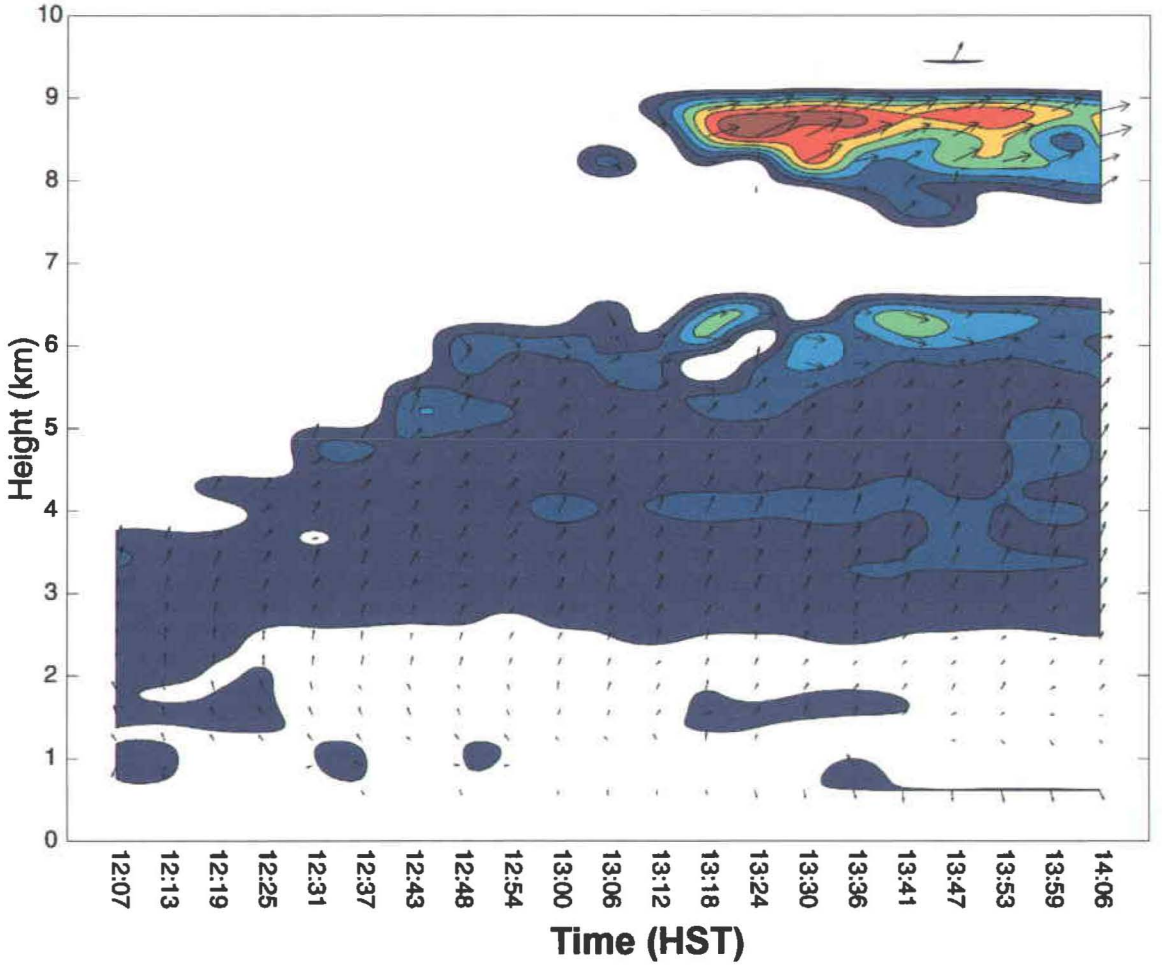

Figure 27. Sequence of PHMO VAD from 1306 to 1735 HST. Color shading represents 2 m s^{-1} intervals in wind speeds starting with 2 m s^{-1}.

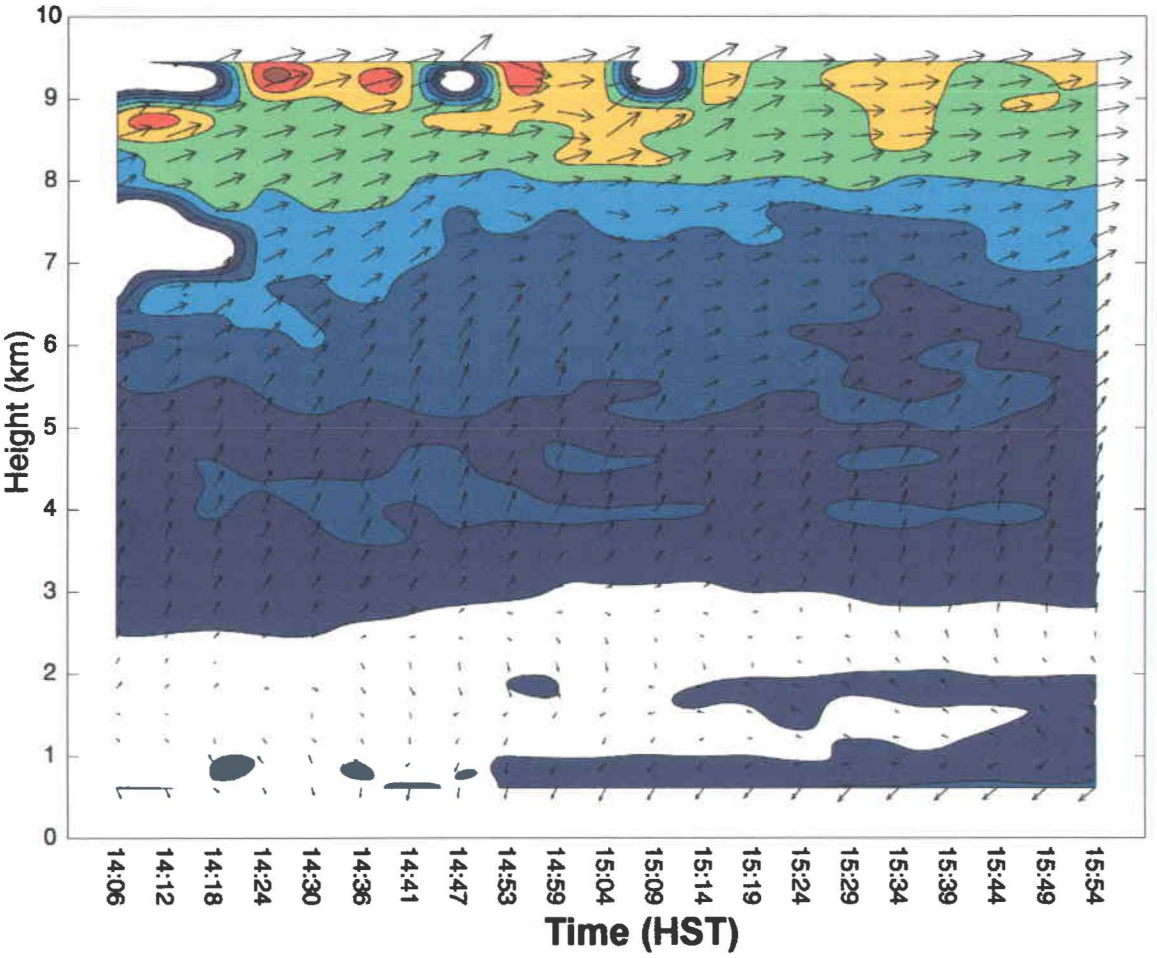

Figure 27 continued. Sequence of PHMO VAD from 1306 to 1735 HST.

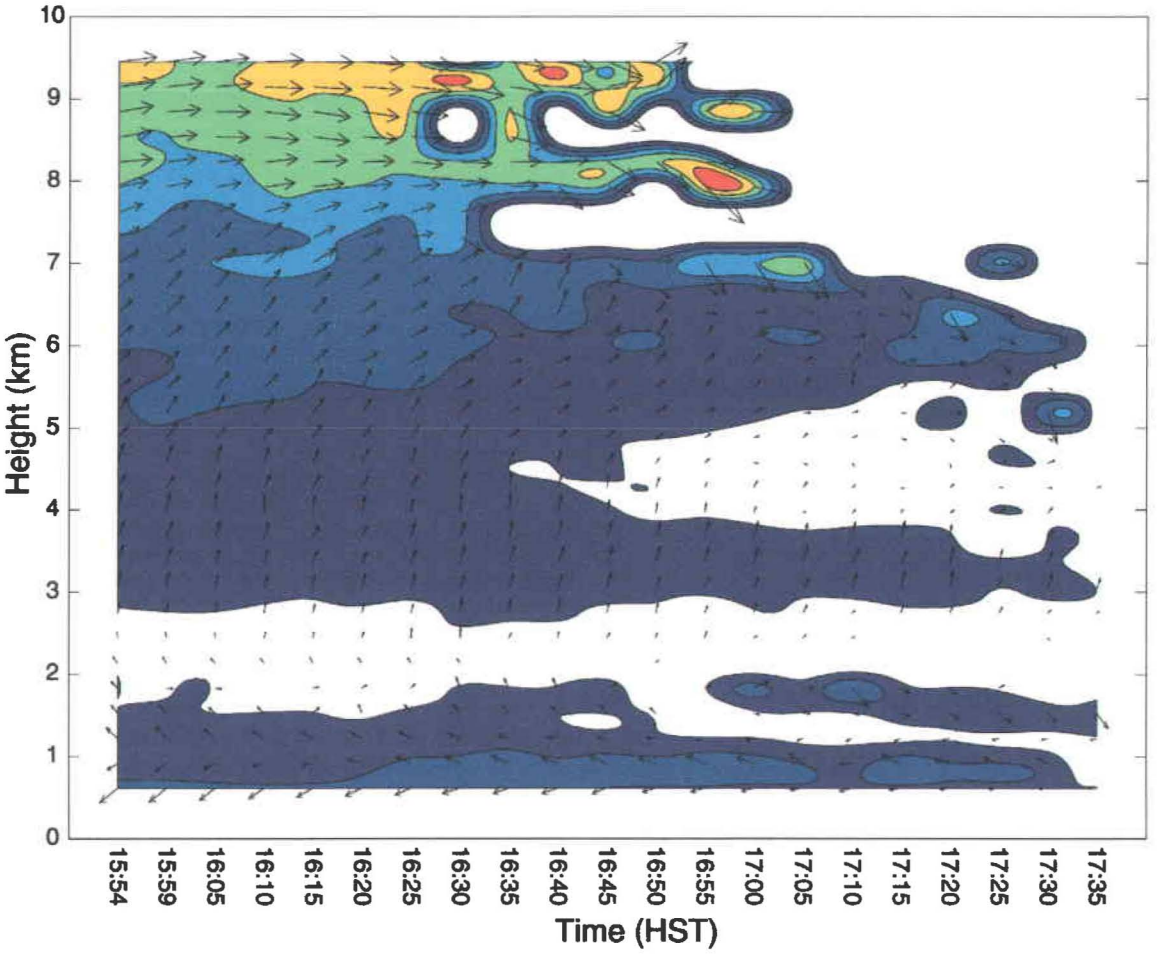

Figure 27 continued. Sequence of PHMO VAD from 1306 to 1735 HST.

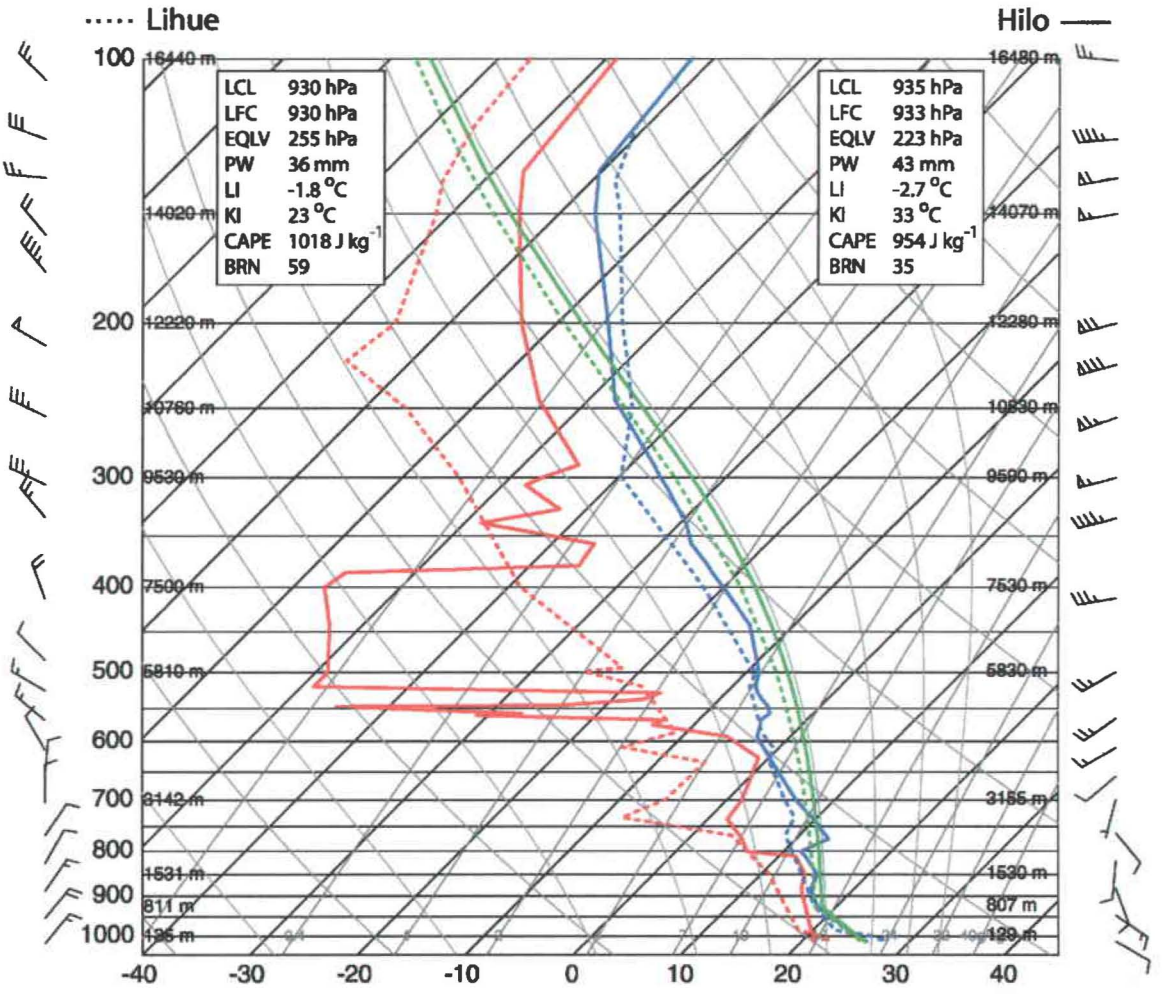

Figure 28. Hilo and Lihue Sounding for 1400 HST 29, October 2000. Dashed lines represent the Lihue sounding, while the solid lines show the Hilo sounding. Wind barbs are plotted in knots; triangle wind barb = 25 m s^{-1}, full wind barb = 5 m s^{-1}, half barb = 2.5 m s^{-1}. LCL - lifted condensation level, LFC - level of free convection, EQLV - equilibrium level, PW - precipitable water through 100 mb, LI - lifted Index, KI - K-index, CAPE - convective available potential temperature, BRN - Bulk Richardson Number.

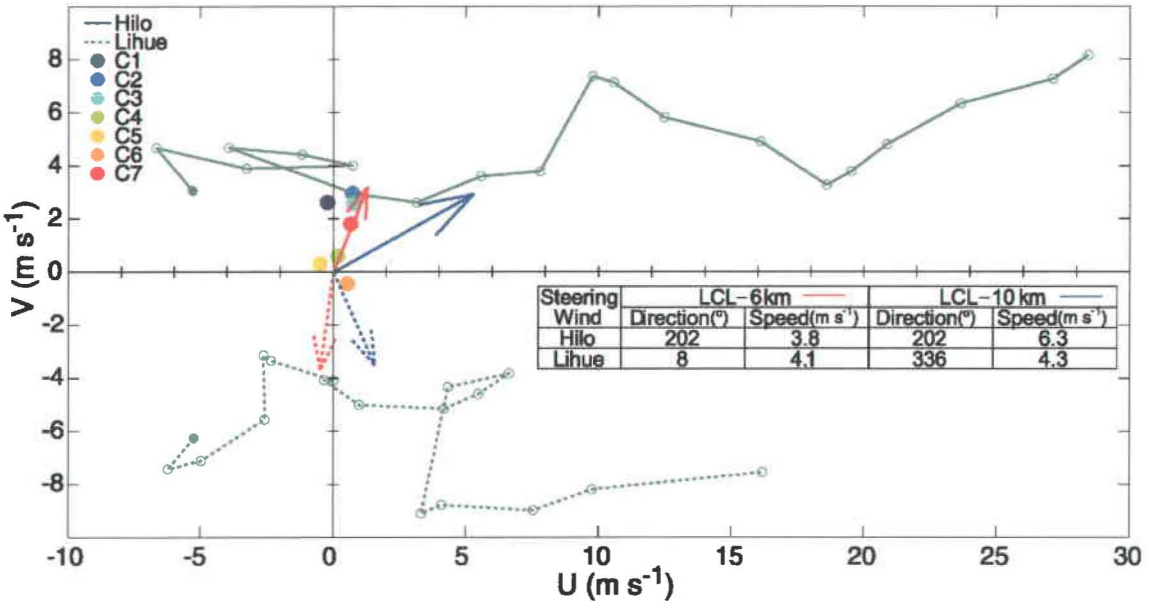

Figure 29. Hilo and Lihue hodograph for 1400 HST 29, October 2000. Surface winds are depicted by the green filled circle, while each circle shows increased intervals of 500 m in height. Colored circles denote the mean motion of the seven cells found in the Hana Storm. Red arrow and blue arrows shows the density weighted steering wind, calculated at 50 hPa interval levels between 950 to 500 hPa and 950 to 250 hPa respectively . The speed and direction for each wind vector is found in the inset table.

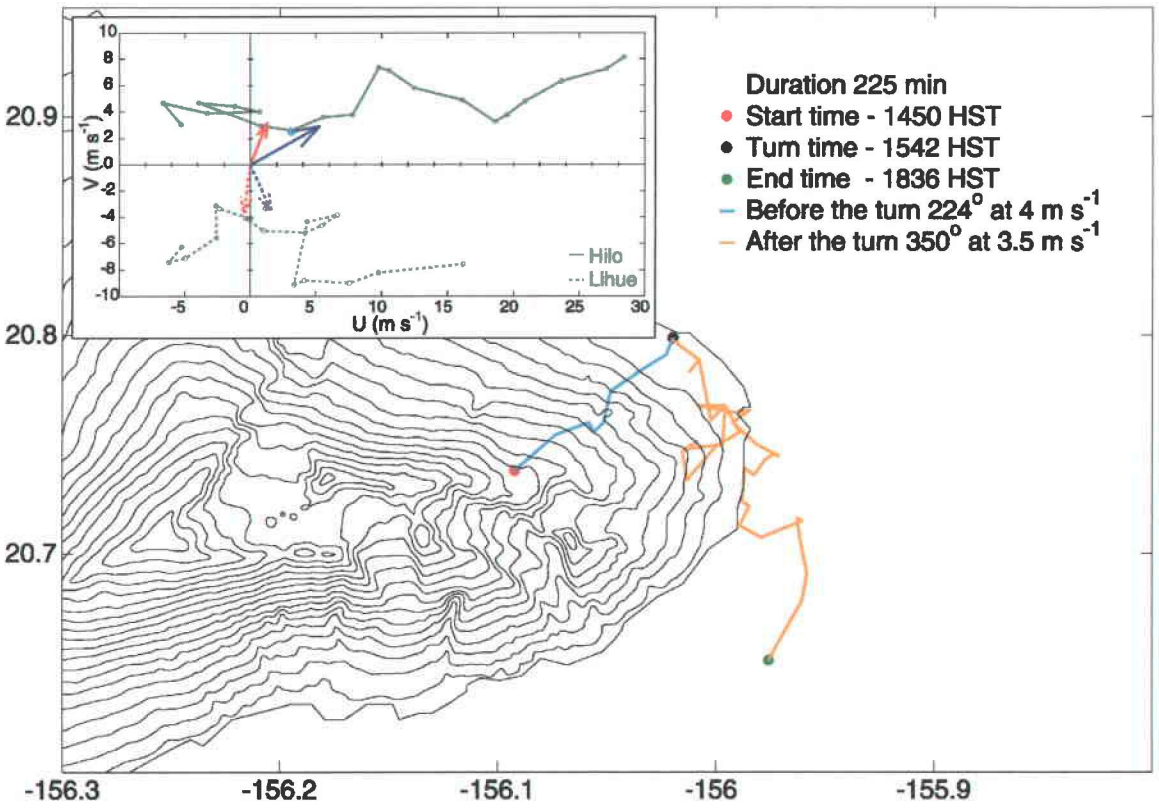

Figure 30. Track description of C6. The inset shows the Hilo and Lihue hodograph as displayed in Figure 29. Blue dot denotes the mean cell motion of C6 prior to the turn, while the orange dot illustrates the mean cell motion after the turn.

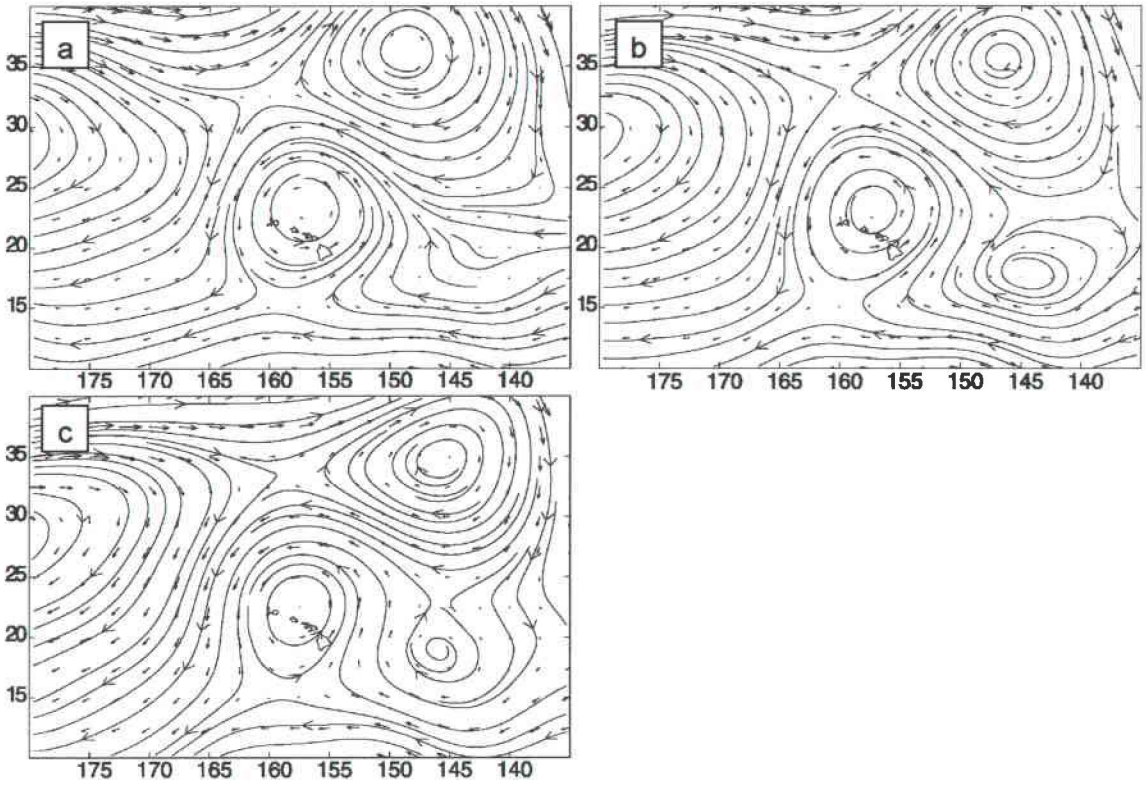

Figure 31. NCEP reanalysis mean density weighted horizontal wind throughout the cloud bearing layer (925-250 hPa). a) 0800 HST; b) 1400 HST; c) 2000 HST.

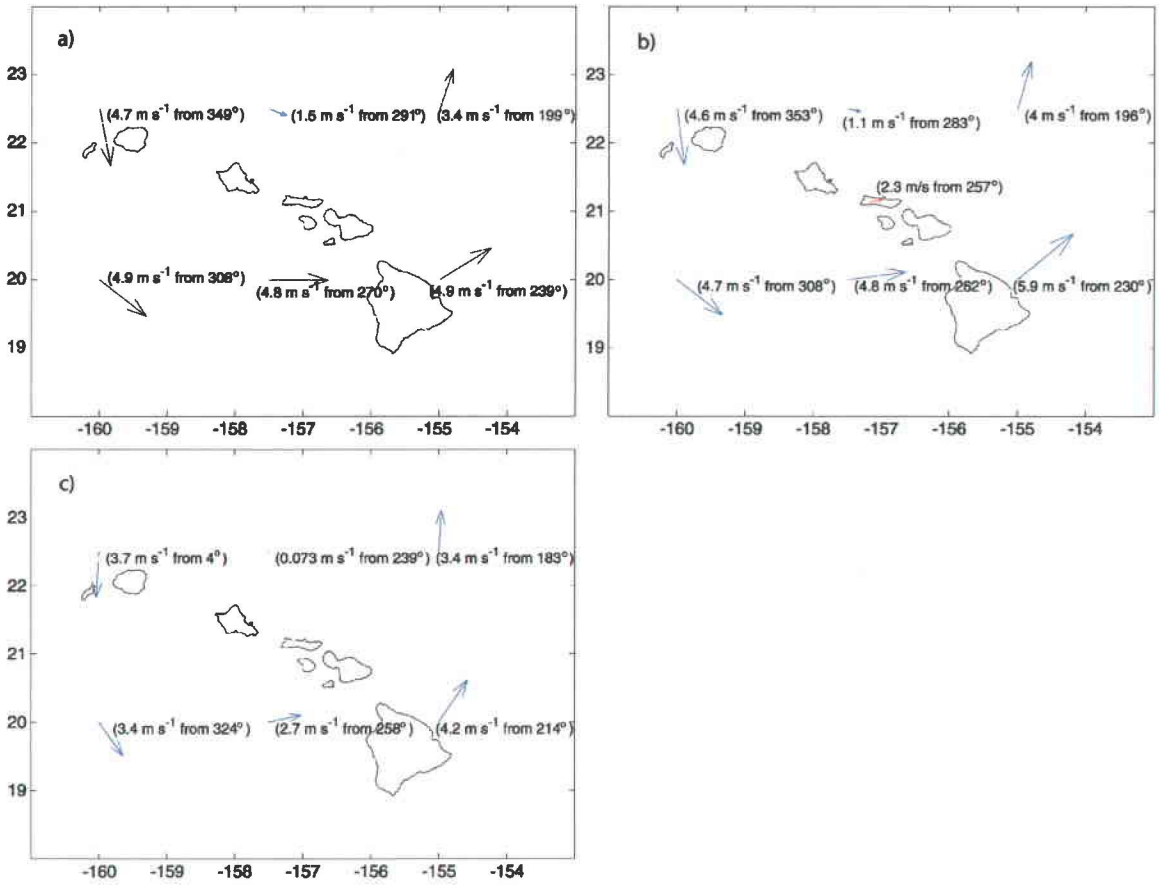

Figure 32. NCEP reanalysis mean density weighted horizontal wind for Hawaii. a) 0800 HST; b) 1400 HST; c) 2000 HST. Red arrow on the b) panel represents the mean density horizontal wind from the PHMO VAD.

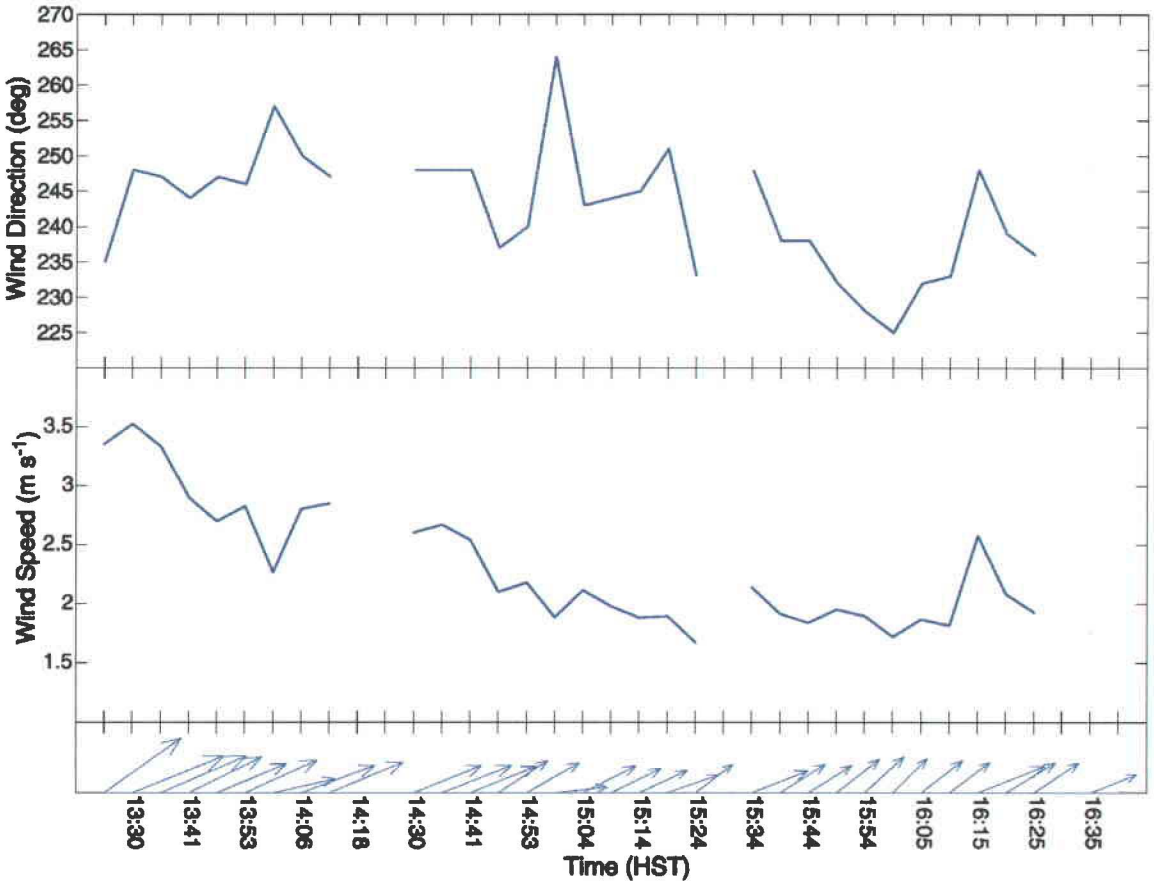

Figure 33. PHMO steering wind for 1334 to 1635 HST. The top panel and middle panel represents the mean wind direction and speed throughout the depth of the troposphere, respectively. The bottom panel depicts the mean wind vector.

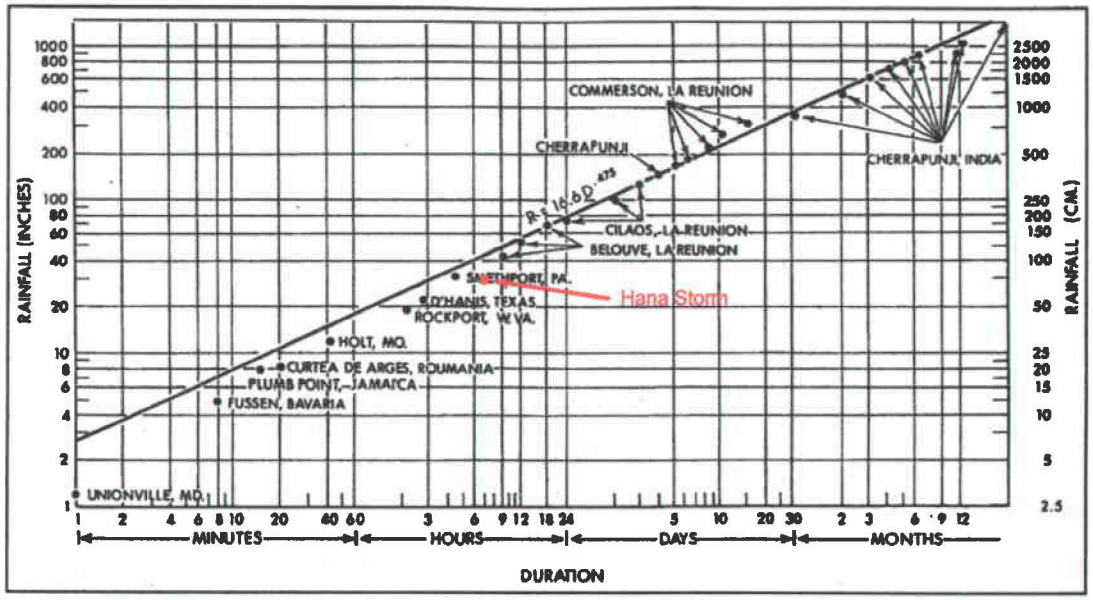

Figure 34. World record observed point rainfalls for various time periods. Taken from Ramage (1995) but including the Hana Storm

Figure 35. Mokulehua Bridge and "another rain gauge." a) Mokulehua bridge is 6 m deep and 30 m wide, b) and c) another rain gauge shows the accumulation of rain over the weekend of the Hana Storm.

REFERENCES

Akaeda, K., J. Reisner, D. Parsons, 1995: The role of mesoscale and topographically induced circulations in initiating a flash flood observed during the TAMEX project. *Mon. Wea. Rev.*, **123**, 1720-1739.

Austin, P. M., 1987: Relation between measured radar reflectivity and surface rainfall. *Mon. Wea. Rev.*, **115**, 1053–1053.

Baeck, M. L. and J. A. Smith, 1998: Rainfall estimation by the WSR-88D for heavy rainfall events. *Wea.* Forecasting, **13**, 416–436.

Battan, L. J., 1973: *Radar Observation of the Atmosphere.* The University of Chicago Press. 324 pp.

Bauer-Messmer, B., J. A. Smith, M. L. Baeck, and W. Zhao, 1997: Heavy rainfall: contrasting two concurrent great plains thunderstorms. *Wea. Forecasting*, **12**, 785–798.

Birchard, T. R., 1999: Investigation of radar reflectivity-rainrate relationship in Hawai`i. M. S. thesis, Dept. of Meteor., Univ. of Hawai`i. 64 pp.

Browning, K. A., 1964: Airflow and precipitation trajectories within severe local storms which travel to the right of the winds. *J. Atmos. Sci.*, **20**, 634-639..

Browning, K. A. and R. Wexler, 1968: The determination of kinematic properties of a wind field using doppler radar. *J. Appl. Meteor.*, **7**, 105–113.

Carbone, R. E., J. D. Tuttle, W. A. Cooper, V. Grubisic, and W. C. Lee, 1998: Trade wind rainfall near the windward coast of Hawaii. *Mon. Wea. Rev.*, **126**, 2847–2863.

Carcena, F., R. A. Maddox, L. R. Hoxit, and C. F. Chappell, 1979: Mesoanalysis of the Big Thompson storm. *Mon. Wea. Rev.,* **107**, 1-17.

Chappell, C. F., 1986: Quasi-stationary convective events. *Mesoscale Meteorology and Forecasting*, P. S. Ray, Ed., Amer. Meteor. Soc., 289-310.

Chen, Y. L., and A. J. Nash, 1994: Diurnal variation of surface airflow and rainfall frequencies on the island of Hawai`i. *Mon. Wea. Rev.*, **122**, 34–56.

Chisholm, A. J., and J., H., Renick, 1972: The kinematics of multicell and supercell Alberta hailstorms. Hail Studies Rep. No. 72-2, Alberta Hail Studies 1972, Research Council of Alberta, Edmonton, Alberta, 24-31.

Cram, R. S. and H. R. Tatum, 1979: Record torrential rainstorms on the island of Hawaii. January-Febuary 1979. *Mon. Wea. Rev.*, **107**, 1653-1662.

Crum, C. D., R. L. Alberty, and D. W. Burgess, 1993: Recording, archiving, and using WSR-88D data, *Bull. Amer. Meteor. Soc.*, **74**, 645-653.

Davis, R. S., 2001: Flash flood forecast and detection methods. Severe Convective Storms, Amer. Meteor. Soc., Meteor. Monogr., **28**, 481-525.

Doswell, C. A., H. E. Brooks, and R. A. Maddox, 1996: Flash flood forecasting: an ingredient-based methodology. *Wea. Forecasting*, **11**, 560-581.

Doswell, C. A., 1996: What is a supercell? 18th AMS Conf. Severe Local Storms (San Francisco, CA), 19-23 February 1996, Amer. Meteor. Soc., 641.

Doswell, C. A., 2002: Severe convective storms – An overview. Severe Convective Storms, Amer. Meteor. Soc., Meteor. Monogr., **28**, 1-26.

Dracup, J. A., E. D. H. Cheng, J.M. Nigg, and T. A. Schroeder, 1991: The New Year's Eve Flood on Oahu, Hawaii, December 31, 1987-January 1, 1988. *Natural Disaster Studies*, Vol. 1, National Academy Press, 72 pp.

Fankhauser, J. C. 1964: On the motion and predictability of convective systems as related to the upper winds in a case of small turning of wind with height. National Severe Storms Proj. Rep. 21.

Fankhauser, J. C. and C. G. Mohr, 1977: Some correlations between various sounding parameters and hailstorm characteristics in northeast Colorado. *Preprints 10th conference on severe local storms*, Omaha, Nebraska, Amer. Meteor. Soc., 218-225.

Foote, G. B. and C. G. Wade, 1982: Case study of a hailstorm in Colorado. Part I: Radar echo structure and evolution. *J. Atmos. Sci.*, **39**, 2828–2846.

Fullerton, C. M., and S. K. Wilson, 1975: An analysis of four showers with rainfall rates >250 mm/hr. Water Resource Research Center, University of Hawaii Tech. Rep. 90, 45 pp.

Galway, J. G., 1956: The lifted index as a predictor latent instability. *Bul. Amer. Meteor. Soc.*, **37**, 528-529.

George, J. J., 1960: *Weather and Forecasting for Aeronautics*. Academic Press, 673 pp.

Giambelluca, T. W., M. A. Nullet, and T. A. Schroeder, 1986: Rainfall Atlas of Hawai'i. Rep. R76, Water Resource Research Center, University of Hawaii, 267 pp.

Haraguchi, P. 1977: Forecasting floods in Hawaii (excluding Hawaii island). NOAA Tech. Memo, NWSTM PR-16, 30 pp.

Houze, R. A. Jr., 1977: Structure and dynamics of a tropical squall-line system. *Mon. Wea. Rev.*, **105**, 1540-1567.

Hudlow, M., and R. Arkell, 1978: Effect of temporal and spatial sampling errors and Z-R variability on accuracy of GATE radar rainfall estimates. Preprints, 18th Conf. Radar Meteor., Amer. Meteor. Soc., Boston, 342-349.

Hudlow, M. D. and V. Patterson, 1979: GATE radar rainfall atlas. NOAA Special Report, Washington D.C., 155 pp.

Jorgensen, D. P.,E. J. Zipser, and M. A. LeMone, 1985: Vertical motions in intense hurricanes. *J. Appl. Meteor.*, **42**, 839–856.

Juang, H. H. 2000: The NCEP Mesoscale Spectral Model: A revised version of the non-hydrostatic Regional Spectral Model. *Mon. Wea. Rev.*, **128**, 2329-2362.

Kelly, W. E. and D. R. Mock, 1982: A diagnostic study of upper tropospheric cold lows over the western North Pacific. *Mon. Wea. Rev.*, **110**, 471-480.

Kodama K. and G. M. Barnes, 1997: Heavy rain events over the south-facing slopes of Hawaii: Attendant Conditions. *Wea. Forecasting,* **12**, 347-367.

Knight C. A., P. Smith, and C. Wade, 1982: Storm types and some radar reflectivity characteristics. Hailstorms of the Central High Plains Vol. I, Colorado Associated University Press, 81-93.

Maddox, R. A., C. F. Chappell, and L. R. Hoxit, 1979: Synoptic and meso-alpha scale aspects of flash flood events. *Bull. Amer. Meteor. Soc.*, **60**, 115-123.

Marwitz, J.D. 1972: The structure and motion of severe hailstorms. Part I: Supercell storms. *J. Appl. Meteorol.*, **11**, 166-179.

Petersen, W. A., L. D. Carey,S. A. Rutledge, J. C. Knievel, R. H. Johnson, N. J. Doesken, T. B. McKee, T. Vonder Haar, and J. F. Weaver, 1999: Mesoscale and radar observations of the Fort Collins flash flood of 28 July 1997. *Bull. Amer. Meteor. Soc.*, **80**, 191–216.

Ramage, C. S. 1971: *Monsoon Meteorology.* Academic Press. 296 pp.

Ramage, C. S. 1995: *Forecasters Guide to Tropical Meteorology.* Air Weather Service, 392 pp.

Reinhart, R. E., 1991: *Radar for Meteorologists.* Available from the Department of Atmospheric Sciences, University of North Dakota, 334 pp.

Rodgers, R. R., 1967: Doppler radar investigation of Hawaiian rain. *Tellus*, **19**, 433-455.

Rosenfeld, D., D. Atlas, D.B. Wolff, and E. Amitai, 1992: Beamwidth effects on the Z-R relations and area-integrated rainfall. *J. Appl. Meteor.*, **31**, 5, 454-464.

Rosenfeld, D., D. B. Wolff, and D. Atlas, 1993: General probability-matched relations between radar reflectivity and rain rate. *J. Appl. Meteor.*, **32**, 50–72.

Schroeder, T. A. 1977: Meteorological analysis of an Oahu flood. *Mon. Wea. Rev.*, 105, 458-468.

Schroeder, T. A. 1978: Mesoscale structure of Hawaiian rainstorms. Water Resource Research Center, University of Hawaii Tech Rep. 119, 69 pp.

Szoke, E. J. and, E. J. Zipser, 1986: A radar study of convective cells in mesoscale systems in GATE. Part II: Life cycles of convective cells. *J. Appl. Meteor.*, **43**, 199–218.

Tokay, A. and D. A. Short, 1996: Evidence from tropical raindrop spectra of the origin of rain from stratiform versus convective clouds. *J. Appl. Meteor.*, **35,** 355–371.

U.S. Department of Commerce, 1962: Rainfall frequency atlas of the Hawaiian Islands. Weather Bureau Tech. Paper No. 43, 60 pp.

Weisman, M.L. and J.B. Klemp, 1982: The dependence of numerically simulated convective storms on vertical wind shear and buoyancy. *Mon. Wea. Rev.*, **110,** 504–520.

Weisman, M.L. and J.B. Klemp, 1986: Characteristics of isolated convective systems. *Mesoscale Meteorology and Forecasting*, P. S. Ray, Ed., Amer. Meteor. Soc., 331-358.